X-RAY INDUCED EFFECT ON CHARGE CARRIER TRAPPING LIFETIME OF a-Se PHOTOCONDUCTORS AND THE RECOVERY PROCESS

A Thesis Submitted

To the College of Graduate and Postdoctoral Studies

In Partial Fulfillment for the Degree of Master of Science

In the Department of Electrical and Computer Engineering

University of Saskatchewan

By

Emmanuel B. Adeagbo (B.Sc.)

Saskatoon, Saskatchewan, Canada

PERMISSION TO USE

In presenting this thesis in partial fulfillment of the requirements for a Postgraduate degree from the University of Saskatchewan, I agree that the Libraries of this University may make it freely available for inspection. I further agree that permission for copying of this thesis in any manner, in whole or in part, scholarly purpose may be granted by the professor or professors who supervised my thesis work or, in their absence, by the Chair of the Department or the Dean of the College in which my thesis work was done. It is understood that due recognition shall be given to me and to the University of Saskatchewan in any scholarly use which may be made of any material in my thesis.

Request for permission to Copy or to make other use of the material in this thesis in whole or part should be addressed to:

Chair of the Division of Electrical and Computer Engineering
57 Campus Drive
University of Saskatchewan
Saskatoon, Canada, S7N 5A9

Or

Dean
College of Graduate and Postdoctoral Studies
University of Saskatchewan
116 Thorvaldson Building, 110 Science Place
Saskatoon, Saskatchewan S7N 5C9
Canada

ABSTRACT

Amorphous selenium (a-Se) alloy x-ray detectors are currently used in commercial mammographic detectors for breast cancer detection and diagnosis. They have been only recently commercialized and there are now at least five companies manufacturing these detectors. This work focuses on the study of the X-ray induce effects on the carrier trapping lifetime in a-Se, and the recovery process of the X-ray induced damage in the bulk of a-Se samples. The x-ray dose effect on the carrier trapping lifetime was studied alongside the temperature effect on the induced x-ray damage and recovery process. The carrier trapping lifetime reduces as the accumulated dose deposited in the a-Se samples increases. Upon the cessation of x-ray exposure, carrier lifetime recovered slowly (over many hours) back to its original state. The damage was not permanent. Several a-Se detectors samples have been exposed to high doses of x-ray and the recovery process has been observed under different temperature, 23.5 ^{o}C and 35.5 ^{o}C. The time of flight (TOF) measurement technique was employed to measure the carrier drift mobility μ and the interrupted filed time of flight (IFTOF) technique was used to measure the carrier trapping lifetime τ. All samples used in this project are pure a-Se for hole transport measurements, a-Se: 0.3%: 2.5ppm Cl and a-Se: 0.5%: 10ppm Cl for electron transport measurements. Sample thickness ranges from 50 μm to 200 μm with a variance of $\pm$5 μm at different positions on the sample. The applied dose rate during the x-ray irradiation ranges from 1.9 Gy/s to 2.5 Gy/s. The difference in dose rate does not affect the change in the hole trapping lifetime but has a non-significant effect on the electron trapping lifetime. The rate of decrease in the hole normalized lifetime is more rapid at 35.5^{o}C than at room temperature (23.5^{o}C). The recovery processes were also observed to be more rapid at the higher temperature.

ACKNOWLEDGMENT

My heartfelt appreciation to my ever-supporting supervisor, Dr. S.O. Kasap first, for the opportunity to carry out this study under his guidance. His support throughout the course of this project is highly appreciated. My sincere appreciation to George Belev for helping in making samples and the setting up of the experiments for this research work. I would like to thank Cyril Koughia for his invaluable support, assistance and all the problem-solving discussions. I would like to appreciate my colleagues; Farley Chicilo, Thomas Meyer, Ozan Gunes for their supports during the course of this work. The financial supports from the University of Saskatchewan and Analogic Canada Corp have been very instrumental during the course of this research work, thank you.

Finally, my deepest gratitude goes to my wife, Adeagbo Shade, for her ever-abiding support throughout this program. Your support and understanding are sincerely appreciated, I love you dearly. Thanks to my daughter, Adeagbo Ayanfeoluwa for being such an awesome child. I appreciate my parents, Pastor Jacob Adeagbo and Victoria Adeagbo, for your prayers and support. Thanks to my siblings, Oluwaseun, Oluwatunmise, Oluwatosin and Adetutu for your understanding throughout the course of this work.

TABLE OF CONTENTS

PERMISSION TO USE i

ABSTRACT ii

ACKNOWLEDGEMENT iii

TABLE OF CONTENTS iv

LIST OF TABLES viii

LIST OF FIGURES ix

LIST OF ABBREVIATIONS xvii

1. INTRODUCTION…… 1

1.1 Introduction…..... 1

1.2 Digital X-ray Imaging…..... 3

1.3 Materials for X-ray Detector…….…… 7

1.3.1 Stabilized a-Se as an X-ray Photoconductor…..…….. 8

1.3.2 X-ray Absorption Coefficient……... 10

1.3.3 Electron-Hole Pair Creation Energy……. 11

1.3.4 Charge Transport and Schubweg……..… 12

1.4 Research Objectives…….. 13

1.5 Thesis Outline and Objectives……..……... 14

2. THEORY…….……..…….. 15

2.1 Amorphous Selenium Structures and Properties……..... 15

2.1.1 Introduction…….…. 15

2.1.2 Structure of Amorphous Solid …….……. 16

2.1.3 Band Theory for Amorphous Semiconductors…..…… 17

2.1.4 The Atomic Structure of Amorphous Selenium…..……. 20

2.1.5 Density of State of a-Se and Carrier Transport in a-Se…… 25

2.1.6 Optical Properties of a-Se……. 28

2.2 X-ray Absorption……...…….. 31

2.3 Time-of-Flight and Interrupted-Field Time-of-Flight transient Photoconductivity……. 35

2.3.1 Introduction…….……. 35

2.3.2 The Time-of-Flight Measurement Technique…..…….36

2.3.3 The Interrupted-Field Time-of-Flight Technique……..44

2.4 Transient Trap Limited Theories……..45

2.4.1 Monoenergetic Trap Level…….……46

2.4.2 Multiple Trap Distribution……51

2.5 Summary…….…… 55

3. EXPERIMENTAL PROCEDURE……..…….. 57

3.1 Introduction…….…….57

3.2 Sample Preparation…….…….57

3.3 X-ray Dose Measurement……..…..… 61

3.3.1 X-ray Tube System……..……. 61

3.3.2 X-ray Dose Measurement System…… 63

3.3.3 X-ray Dose Rate Adjustment……....64

3.4 Charge Transport Measurements……..……...64

3.5 TOF/IFTOF Experimental System……..…… 70

3.5.1 System Overview……. 70

3.5.2 High Voltage Switch and Supply……..……72

3.5.3 Amplifier……...73

3.5.4 Laser and Trigger System …….……... 74

3.5.5 Data Acquisition System…….. 77

3.6 X-ray Induced Carrier-trapping Lifetime Changes……..78

3.6.1 Accumulated Dose Measurement……..……..…. 79

3.6.2 Lifetime Recovery Measurement…….……79

3.7 Temperature Control Systems…….....80

3.8 Summary……...…..……..81

4. RESULT AND DISCUSSION……...……. 83

4.1 Introduction……..…….…….. 83

4.2 X-ray Dose Deposited in the a-Se Samples…….…… 83

4.3 Charge Carrier Mobility and Lifetime……. 88

4.3.1 X-ray Irradiation Effect on Lifetime…….91

4.4 Lifetime Recovery……..……. 102

4.5 Summary……..105

5. SUMMARY AND CONCLUSION……..…….. 106

5.1 X-ray Induced Change in Lifetime of Amorphous Selenium…….106

5.2 Carrier Trapping Lifetime Recovery Process…….. 108

5.3 Future Works……...…… 108

REFERENCES……..…….. 110

LIST OF TABLES

Table 3.1: Working Cycle of the X-ray tube [51] ……..……63

Table 4.1: Absorbed dose rate per second for listed samples at 70 kVp X-ray tube Voltage and 15mA filament current……...87

Table 4.2 Measured carrier mobility……..……91

Table 4.3 Measured carrier trapping lifetime before irradiation …..…….91

Table 4.4 Different dose rate for electrons and holes measurement……92

Table 4.5: Normalized lifetime change rate dependence on dose rate for hole…….……...95

Table 4.6: Normalized lifetime change rate dependence on dose rate for electron……..……96

Table 4.7: Hole and Electron normalized lifetime change rate at different temperature……99

Table 4.8: Structural Relaxation Time for Different Temperature……104

LIST OF FIGURES

Figure 1.1: A typical projection radiography consists of the x-ray tube, collimator, and x-ray detector…….. 2

Figure 1.2: Simplified x-ray imaging system utilizing a phosphorescent screen and a photographic film. After Allen [7] …….…….…….3

Figure 1.3: Block diagram of digital imaging system……..4

Figure 1.4: A typical structure of indirect conversion x-ray detector [59] ……..5

Figure 1.5: A small section of a thin film transistor active matrix array used in a direct conversion detector [60]……...6

Figure 1.6 A Cross-sectional view of a pixel in an a-Se direct conversion x-ray detector. After Kasap [6]……6

Figure 1.7: Two x-ray images captured by a-Se based flat panel x-ray detectors after Kasap and Rowland [5] …… 9

Figure 1.8: The linear attenuation coefficient α and absorption depth ($1/\alpha$) of a-Se and other semiconductors of interest as a function of the incident energy in the X-ray spectrum. After Kasap et al. [5] ……10

Figure 2.1: Two-dimensional representation of the structure of (a) a crystalline solid; (b) an amorphous solid. Spheres mark “O” and “U” represent over-coordinated and under-coordinated atoms respectively. After Fogal [6]…...16

Figure 2.2: Density of states models for crystalline and amorphous semiconductors. (a) Crystalline semiconductor: two bands separated by a forbidden energy region. (b) Initial DOS model for amorphous semiconductors; localized

states encroach into the band gap. (c) The CFO model; the localized states extend all the way into the band gap and overlap. (d) Marshal and Owen model; structural defects create many localized states deep in the band gap [8]…… ….. 19

Figure 2.3: Definition of dihedral angle in selenium random chain model. (a) Dihedral angle formed between two planes of atoms 123 and 234. (b) Looking down on the bond joining atoms 2 and 3. The bond angle θ and the bong length *r* [25]……..22

Figure 2.4: A Random model of a-Se depicting chain-like and ring-like chains. After Lukovsky [25]……..22

Figure 2.5: The structure and energy of simple bonding configurations for selenium atoms. Straight lines represent bonding orbitals, lobes represent lone-pair (nonbonding) orbitals, and circles represent antibonding orbitals. The energy of a lone-pair is taken as the zero energy. This Figure is adapted from [61] ……...……....23

Figure 2.6: The VAP defects with a distribution of a net charge a) two chain VAPs defects. (b) Single IVAP defects while a one-fold coordinated negatively charged Se atom C_1^- and a three-fold coordinated positively charged Se atom C_1^+ are on the same side. c) Two IVAPs belongs to different chains and form a common one. After Kasap et al [34] ……24

Figure 2.7 Density of State model suggested by Abkowitz. After Abkowitz [29]……...25

Figure 2.8. Generalized DOS model. (a) DOS around conduction band. (b) DOS around valence band. The bars in the center depict the concentration of deep carrier traps for both electrons and holes. After Kasap et al [31] ……..26

Figure 2.9: Density of State distribution for shallow traps. One peak is observed 0.27 –0.33 *e*V below the band edge. Another Gaussian peak is observed 0.38 – 0.48 *e*V below the band edge. After Kasap et al [31…….27

Figure 2.10: Absorption coefficient and quantum efficiency as a function of incident photon energy (*hv*) for the various applied field. After Pai et al [62]……...30

Figure 2.11 A typical X-ray Spectrum produced from a tungsten X-ray tube at 70 KVp. Source: X-ray spectrum simulation program by Siemens for dose of 1mGy [41]32

Figure 2.12: Schematic diagram of the TOF measurement technique. After Allen [7]…….36

Figure 2.13: The motion of a charge q, through a distance dx makes a charge dQ flow in the external circuit [7] ……..…….39

Figure 2.14: A simplified small signal AC equivalent circuit for the TOF experiment. C_s is the combination of the sample capacitance and any stray capacitances added by the cables…….40

Figure 2.15: Simulated TOF (a) I-mode and (b) V-mode photocurrent with no traps (solid) and deep trapping (dashed). After Fogal [6] ……..43

Figure 2.16: A typical ideal waveform of TOF measurement……43

Figure 2.17: A typical ideal waveform of IFTOF measurement. The photocurrent is $i(t_1)$ and the photocurrent after the interruption is $i(t_2)$. Interruption time is t_i……..45

Figure 2.18: Carrier flow in a semiconductor involving trapping and releasing within a slice dx. After Fogal [8[…..……..……..46

Figure 2.19: TOF waveform showing shallow trap-controlled drift ignoring deep tapping because of constant steady state current……..……50

Figure 2.20: Photocurrent waveform in the model of the high field [7] ……52

Figure 2.21: Photocurrent and energy band diagram representation of the TOF experiment with a binary trap distribution. The process of thermalization and deep trapping are shown with exponential decay expression. The charge carrier packet drifts with a velocity v_d. Shallow traps are located just below the conduction band energy E_c while deep traps are in lower energy states just above level E_F…….54

Figure 3.1: NRC 3117 Stainless steel vacuum coater system…….....58

Figure 3.2: Schematic diagram of the NRC 3117 vacuum deposition system used in making the samples. [8].…… ……..…….……59

Figure 3.3: Hummer VI sputtering system……..…….60

Figure 3.4: Schematic diagram of the Hummer VI sputtering system for making contact on the a-Se samples [8] ……...…….……..61

Figure 3.5: Gendex GX 1000 X-ray system and lead chamber protection……62

Figure 3.6: Keithley 35050 Dosimeter and Ion Chamber for X-ray exposure

measurement……..64

Figure 3.7: A simplified schematic diagram of TOF and IFTOF measurement system……..65

Figure 3.8: A typical timing transient voltage response for the (a) TOF and (b) IFTOF signal. The TOF signal show hole transit time t_T which is used to determine hole mobility. For the IFTOF signal, the bias voltage is interrupted to determine hole rapping lifetime……..……67

Figure 3.9: A semi-logarithm plot of the ratio of photocurrent drop and interruption time. The slope of the plot gives the carrier trapping time……...69

Figure 3.10: A grounded bridge network to eliminate the displacement current signal from IFTOF transient measurement…….……..70

Figure 3.11: Some component of the experimental setup for the TOF/IFTOF experiment showing A LN103C nitrogen-pumped laser, a 10V supplied triggering system, an EG&G high voltage supply, a Tektronix digital oscilloscope and a GBIB data……...……71

Figure 3.12 The TOF/IFTOF system schematic……71

Figure 3.13: A 1 KV fast switching high voltage HEXFET switch [6] ……72

Figure 3.14: A two-stage wide bandwidth differential amplifier with 16 dB gain Circuit designed by Dr. Robert Johanson. ..……74

Figure 3.15: (a) The protection circuit system. (b) The timing diagram [4]……74

Figure 3.16: Trigger timing for the LN103C laser [6]……75

Figure 3.17: The PCI-CTR05 interface circuit for generating the trigger system for the TOF/IFTOF System……76

Figure 3.18: Timing signal from the PCI-CTR05 counter board and interface circuit……..…..76

Figure 3.19: GUI interface for TOF/IFTOF in LabView……....78

Figure 3.20: Accumulated dose measurement procedure…..…….79

Figure 3.21: Recovery measurement procedure…….80

Figure 3.22 Thermal controlling system chamber…….81

Figure 4.1: X-ray dose in air in Gy/minutes vs the inverse square distance of the sample from the X-ray source ……84

Figure 4.2: X-ray mass attenuation and the mass-energy coefficient for Selenium vs photon energy. Data interpolated from data from NIST [66] …….85

Figure 4.3: X-ray mass attenuation and the mass-energy coefficient for dry air vs photon energy. Data interpolated from data from NIST [66]……..86

Figure 4.4: Simulated X-ray spectrum at 70 kVp X-ray tube voltage from Siemens [41].……87

Figure 4.5: (a) Hole TOF waveform of a 151 μm thick film of a stabilized a-Se with an applied field of 1.99 V/μm gives transit time of 5.54 μs, μ_h = 0.137 cm^2/V.s . (b) Electron TOF of an 88 μm thick film, applied field is 1.14 V/μm and transit time 286.81 μs, μ_e = 0.003 cm^2/V.s……..……89

Figure 4.6: (a) Hole IFTOF waveform for a 105 μm thick film sample with interruption time of 12 μs, τ_h= 13.92 μs. (b) Electron IFTOF waveform captured for an

88 μm thick film with interruption time of 250 μs, τ_e= 574.29 μs …….……..90

Figure 4.7 (a) Hole TOF signal captured before x-ray exposure. (b) Hole TOF signal captured after x-ray exposure……92

Figure 4.8: X-ray Irradiation effect on Normalized hole-trapping lifetime at a different dose rate……..……...93

Figure 4.9: X-ray Irradiation effect on Normalized electron-trapping lifetime at a different dose rate…….93

Figure 4.10: X-ray dose effect on the normalized hole trapping lifetime at a different temperature…….....97

Figure 4.11: X-ray dose effect on the normalized electron trapping lifetime at a Different temperature.....…...97

Figure 4.12: Normalized lifetime change rate dependence on dose rate……98

Figure 4.13: Hole Normalized lifetime (τ) and its reciprocal ($1/\tau$) dependence on dose D at 35.5 ºC……..100

Figure 4.14: Hole Normalized lifetime (τ) and its reciprocal ($1/\tau$) dependence on dose D at 23.5 ºC……..……100

Figure 4.15: Electron Normalized lifetime (τ) and its reciprocal ($1/\tau$) dependence on dose D at 23.5 ºC…….…….101

Figure 4.16: Electron Normalized lifetime (τ) and its reciprocal ($1/\tau$) dependence on dose D at 35.5 ºC……...…...101

Figure 4.17: Normalized Hole lifetime recovery at different temperature……103

Figure 4.18: Normalized hole lifetime recovery at different temperature…….104

LIST OF ABBREVIATIONS

a-Se	amorphous selenium
AMA	active matrix array
EHP	electron-hole-pair
GPIB	general-purpose instrument bus
DOS	density of states
TOF	Time-of-flight
IFTOF	Interrupted-field Time-of-flight
HV	High voltage
ITO	Indium tin oxide
PCB	printed circuit board
PCI	peripheral component interconnect

1. INTRODUCTION

1.1 Introduction

The discovery of X-rays in the late 19th century by William Rontgen has had an enormous influence on medical diagnosis. Medical imaging, which has become a very popular tool for diagnosis in the medical world, has experienced dramatic improvements during the past few decades. Radiography, one of the major techniques in medical imaging, uses ionizing radiation such as X-rays to view the bones and internal organs of patients. It involves the creation of an image by measuring the differential attenuation of X-rays that pass through a body, which was originally recorded on a film (special x-ray film). X-ray imaging started with the discovery of x-ray by Rontgen and he evolved over many decades. Today, x-ray imaging can be done by using computer tomography, from two dimensional to three-dimensional imaging. The old film technology used an emulsion film covered by a phosphor screen; and both encased in an x-ray cassette. The x-ray photos are absorbed by the phosphor screen, which then emits visible light. The visible light incident on the film then produces the image, similar to the old photographic technology of taking photographs. Each film in an x-ray cassette can only be used for one x-ray exposure and must be changed for each new image to be captured. After exposure, the film must be developed to provide a visible image.

Although this technique has worked well over time, the need to transit to a digital imaging system eventually lead to the development of digital x-ray imaging detectors. This is because digital imaging techniques have the potential for efficient image capturing [1] and can be done in real time. Images can be manipulated and stored in digital forms. Other merits of the digital system include a reduction of x-ray exposure of patience, better image quality for better diagnosis. Digital images are also very easy to transfer from one location to another[2], which will aid quick access to test results as well as remote diagnosis.

Digital images can be achieved by directly converting x-ray photons to an electrical signal in direct-conversion digital x-ray image detectors or indirectly by using a phosphor screen

to convert X-ray radiation to visible light. The light photons are then converted to charge carriers by arrays of photodiodes. The major disadvantage of the latter arrangement is the loss of resolution because of the lateral spread of emitted light in the scintillator as a result of light diffusion (scattering).[3] The indirect detector arrangement has the benefit of reduced manufacturing cost, which comes from the use of arrays photodiodes in the device structure [4]. Well-established scintillators can then be used for converting x-rays to light. Direct conversion flat panel detectors have the advantage of high resolution and are now widely used in digital x-ray imaging with applications in medical, security and industrial imaging [5].

Flat panel x-ray image (FPXI) detectors are large area integrated circuits that can capture an x-ray image and convert it to digital form [6]. These FPXI detectors have two layers; an Active Matrix Array (AMA) which is made up of a two-dimensional array of thin film transistors (TFTs) and an x-ray detection layer [4]. In the detection layer, the incident and absorbed X-rays are cnverted to electronic charges and then these charges are collected and stored in charge collection capacitors; each element of the AMA as a charge storage capacitor. The stored charges are read out by activating the TFTs in a proper order. This produces a digitized image, which can be sent to a computer for processing and display [7].

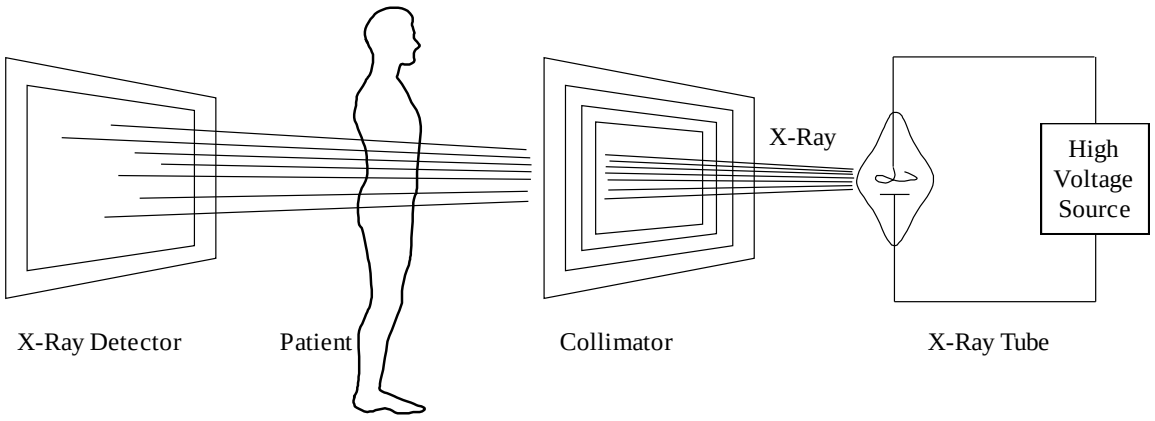

Figure 1.1 A typical projection radiography consists of the x-ray tube, collimator and x-ray detector. (After [8])

1.2 Digital X-ray Imaging

As mentioned earlier, x-ray-based radiography imaging is one of the most prevalent techniques used in medical diagnosis. The process whereby images are created by measuring the quantity of x-ray radiation that passes through an object is known as radiography[8]. The reduction in the x-ray radiation in a given thickness of a material is a function of the x-ray photon energy, the material density, and the thickness through which it must pass[9]. Figure 1.2 shows a typical film-based system in which x-rays are produced by an x-ray source and pass through the object, and then become incident on a phosphor screen. The x-rays passing through the patient are attenuated based on the density and type of the material. The x-rays emerging from the patient therefore correspond the local attenuation experienced by the x-ray beam. The x-ray absorbed in the phosphor screen lead to the emission of visible photons. Some of these photons are then incident on the photographic film and case a reaction and the information is recorded just as in normal film photography.

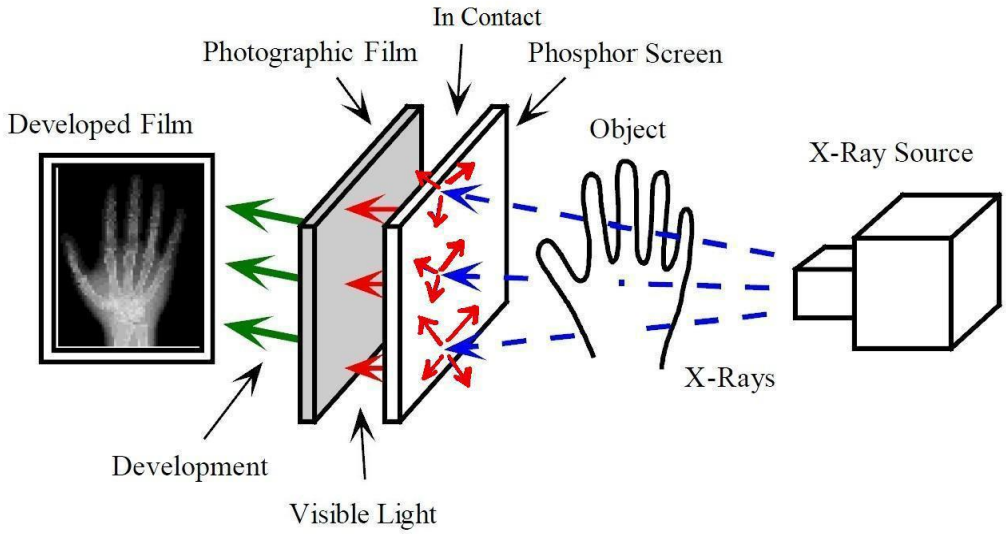

Figure 1.2 Simplified x-ray imaging system utilizing a phosphorescent screen and a photographic film. (After Allen [7])

The medical radiographic imaging system consists of an x-ray source and an x-ray detector. In the case of digital x-ray imaging, the detector is designed and constructed to generate an

electronic imaging from incident x-ray photons. As digital x-ray imaging started gaining grounds in medical radiography, studies of several prospective photoconductive materials for x-ray detectors have been carried out and is still ongoing. Amorphous selenium has shown great potential as an x-ray photoconductor and has been already commercialized in flat panel x-ray image detectors.

Digital x-ray imaging has changed radiography and is bringing new possibilities for improvements in the medical diagnosis. The general form of a digital radiography system is shown in Figure 1.3

X-ray images can be captured in digital x-ray imaging by direct or indirect conversion methods. Figure 1.4 shows the structure of a typical indirect conversion x-ray detector. It uses a reflector as a filter which allows x-ray to reach the scintillator that absorbed the x-ray photons and emits visible light which is absorbed by photodiode array [10]

In the direct conversion method, the x-ray photons are directly converted to electronic carries which are then collected and stored in charge collection capacitors; and are read out by activating the thin film transistor (TFT) switches. There are practically negligible blurring effects in the direct conversion method of x-ray imaging and the output signal has a very high spatial resolution.

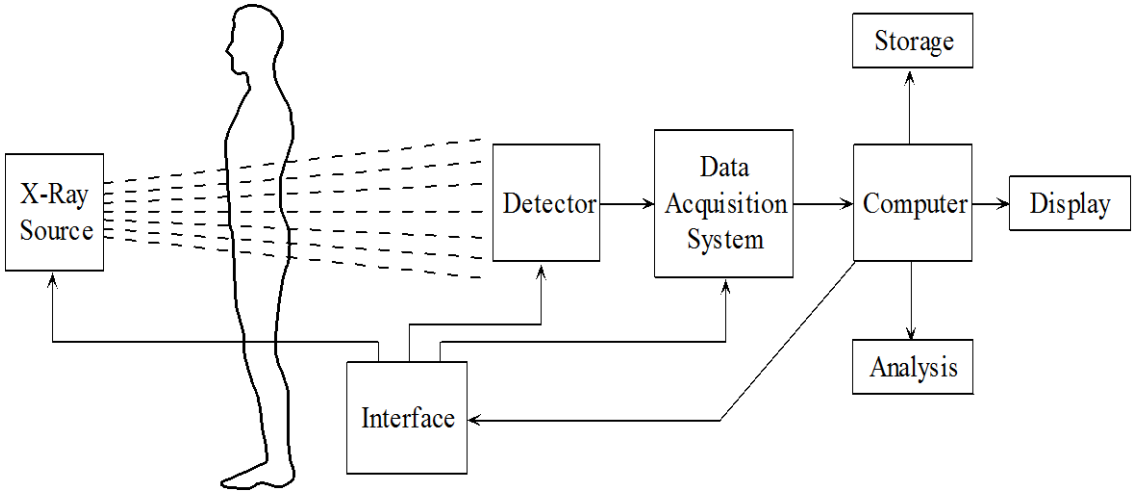

Figure 1.3 Block diagram of a digital imaging system. (After [3])

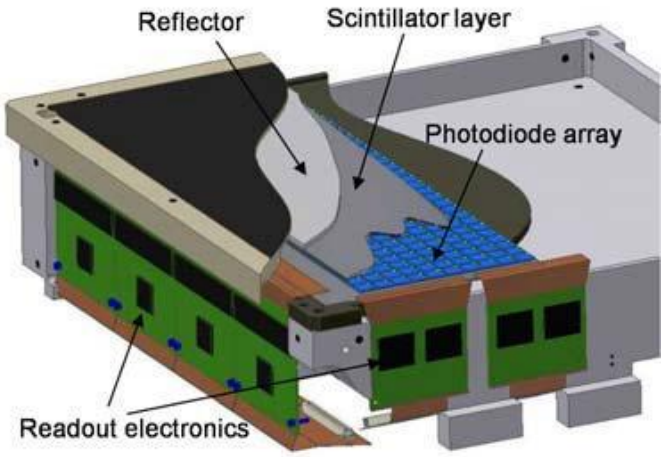

Figure 1.4 A typical structure of indirect conversion x-ray detector. (After [62])

For direct conversion flat panel x-ray image detectors, the principal detecting component that does the conversion of x-rays to collectible charge carriers is the x-ray photoconductor [5]. A typical direct conversion x-ray detector employs a large AMA panel with rows and columns of pixels [11].

Each pixel is a small x-ray detector on its own and contains a small charged capacitor and a thin film transistor. The x-ray photoconductor absorbs x-ray photons which generate electron-hole pairs. The created electron-hole pairs are separated by the applied field across the photoconductor and are drifted by the electric field created by the applied voltage. These carriers are then collected by the electrodes and stored on the storage capacitance, as depicted in Figure 1.6. If an incident radiation of intensity X generates a charge Q in the photoconductor, which is subsequently stored on the capacitance C, the charge Q is read out when the gate of the transistor switch is activated [6].

The gate terminal of each TFT in a row is connected to a control line also known as the gate line and the source terminals in a column is connected to a data line. The reading out process involves the activation of the control line which turns on the TFTs on. When the entire row is on, the stored charge in the capacitor is sent to the data line, processed and sent to the computer [11][7]. The total amount of charge carriers created in the photoconductor is proportional to the intensity and the x-ray photon energy.

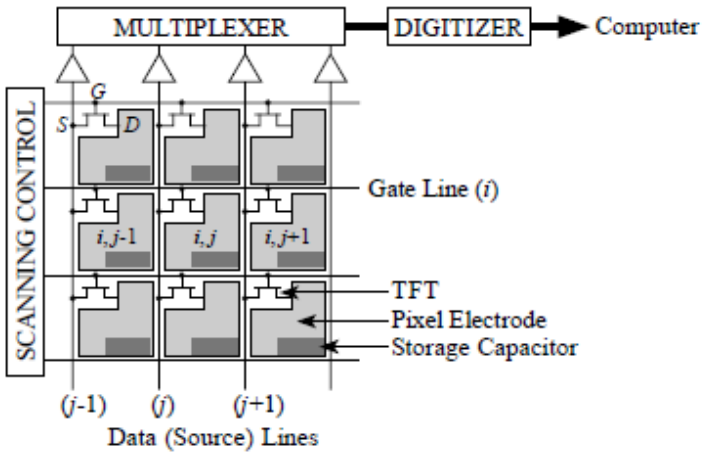

Figure 1.5 A small section of a thin film transistor active matrix array used in a direct conversion detector(After [63])

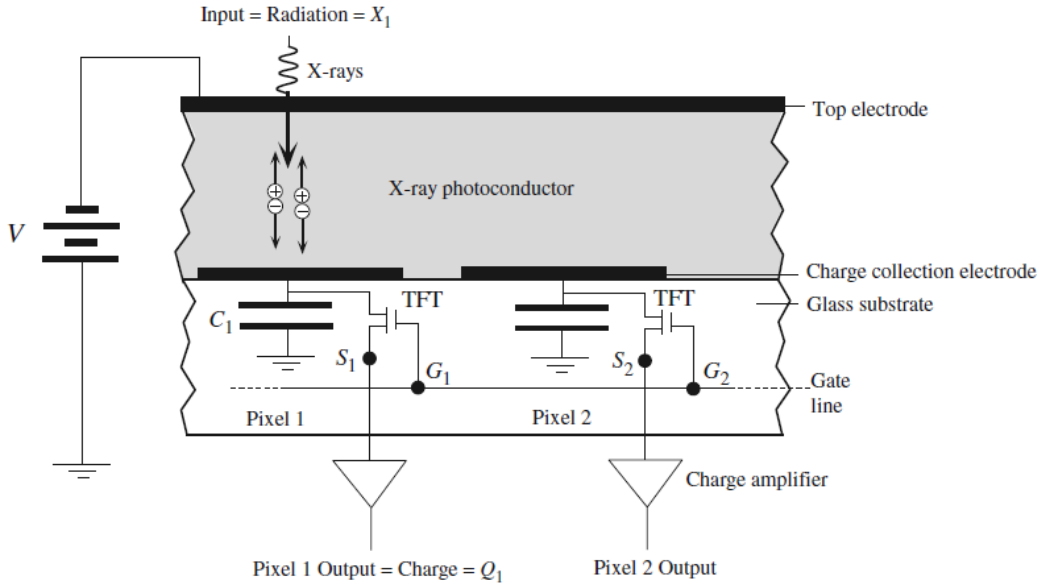

Figure 1.6 A Cross-sectional view of a pixel in an amorphous selenium direct conversion x-ray detector. (After Kasap [6])

The development of direct conversion techniques has brought distinct advances in digital x-ray imaging because of the possibilities of producing higher image quality at lower x-ray doses and being able to do multiple frames one after a another such as in tomosynthesis.

1.3 Materials for X-ray Detector Photoconductor Applications

In this section, certain criteria to look out for in a typical photoconductor material and the factors that affect detector performance are presented. It has been mentioned earlier that the x-ray photoconductor forms the backbone of the direct conversion digital x-ray imaging system. The performance of x-ray photoconductors, therefore, plays a vital role in the overall performance of the system and this solely depends on the quality of the photoconductive material. There are certain properties to look out for in choosing the material that is suitable as an x-ray photoconductor. An ideal photoconductor material should have the following properties.

First, the material must be able to absorb the incident x-rays. A material with a large atomic number tends to have higher x-ray absorption capability. The material of choice should be able to absorb most of the incident X-rays to avoid overexposure to patients. This implies that the absorption depth δ of the x-rays, over the energy range of interest, must be less than the device layer thickness. This also means that the quantum efficiency, which is the fraction of incident photons absorbed, must be high[12][13].

Furthermore, the material should be able to create electron-hole pairs at lower x-ray energy. The latter makes it possible for lower energy x-ray photons to create more electron-hole pairs. This means that the x-ray sensitivity of the material must be high. The radiation energy required to create a single electron-hole pair, denoted by $W_{\pm}$ increases with the bandgap E_g of the photoconductor [14] thus, a low E_g material leads to high x-ray sensitivity. In general, $W_{\pm}$ increases with the bandgap energy [14]. But, in certain semiconductors, it also depends on the applied electric field and the x-ray photon energy.

Another very important criterion is the dark current of the photoconductor. Because photoconductors operate under an applied voltage bias, there is always a dark current flowing in the material[15]. This dark current should be as small as possible to have a very high signal to noise ratio.

The fourth criterion is that the loss of charge carriers by deep trapping during their drift within the photoconductor should be negligible. This implies that the schubweg, which is the product of carrier mobility with the carrier trapping lifetime and the electric field in the

photoconductor ($\mu\tau F$), must be much greater than the thickness of the photoconductor. Also, charge carrier diffusion must be negligible compared to the drift of the carriers. This characteristic will ensure less time for lateral carrier diffusion. The longest carrier transit time, which depends on the smallest drift mobility, must be shorter than the image readout time. Furthermore, the photoconductor properties should not change because of continuous exposure to x-ray over time. In other words, the photoconductor must stable, and x-ray fatigue and x-ray damage should be negligible [16].

X-ray detector performance is a function of the charge transport characteristic of the photoconductor material, thickness of the photoconductor and pixel size and is measured by the sensitivity, quantum efficiency and resolution in terms of the modulation transfer function [17]. The sensitivity depends on the number of absorbed x-ray photons which is characterized by the attenuation coefficient or the attenuation depth, the conversion efficiency of the photoconductor characterized by the EHP creation energy $W_{\pm}$ and the charge collection efficiency which is characterized by the charge carrier range $\mu\tau$ [4].

1.3.1 Stabilized a-Se as an X-ray Photoconductor

Amorphous selenium has found its way to the top of the list of materials used in direct-conversion detectors among many other potential materials. This is because of the properties it possesses. The photoconductivity property of amorphous selenium was first recorded by Willoughby Smith, an electrician for a telegraph company [16]. Recent studies have shown that a-Se photoconductor based flat panel detectors have reached a stage that can be used in different x-ray imaging applications[18] Although selenium has a small atomic number compared to other potential materials with a high atomic number, the range of x-ray energy for optimizing use is low x-ray energy. Amorphous selenium can be easily be coated as a thick film, typically 100 - 1000μm, onto an active matrix array by conventional vacuum deposition method without increasing the temperature to the damage threshold of the AMA [12] [10]. Amorphous selenium has good x-ray attenuation efficiency, good carrier transport and a low dark current is within an acceptable limit.

Figure 1.7 Two x-ray images captured by a-Se based flat panel x-ray detectors. (After Kasap and Rowland [5])

Amorphous selenium in its pure state is not thermally stable and crystallizes over several weeks or months after manufacturing. So, there is a need to stabilize it for any electronic application as an x-ray photoconductor because crystalline Se has much lower dark resistivity which means higher dark current than a-Se. Pure a-Se can be more stable and prevent crystallization by alloying it with As (0.2 – 0.5% As). Although alloying with As prevents crystallization, studies have shown that it introduces deep hole traps which affects hole lifetime.

Doping the alloy with 10 – 20 parts per million (ppm) of halogen, for example, Chlorine, restores the hole lifetime. Therefore, stabilized a-Se is the alloying of a-Se with 0.2 – 0.5% As and doping with 10 -20 ppm Cl [12].

1.3.2 X-ray Absorption Coefficient

The photoconductive layer of an x-ray image detector converts the absorbed x-ray photons to electronic charge carriers. The parameter that determines the number of x-ray photons absorbed by the photoconductor due to photoelectric effect is known as absorption coefficient α. The fraction of incident x-ray photons that are absorbed by the photoconductor is given by:

$$A_Q(E) = [1 - \exp(-\alpha L)] \qquad 1.1$$

Where L is the detector thickness of detector, $\alpha = \alpha(E, Z, d)$ is the absorption coefficient of the photoconductor material which is a function of the incident x-ray energy E, atomic number Z and the density d of the material. The detector thickness is related to the absorption coefficient because sufficient incident x-ray must be absorbed by the photoconductor material for best image quality and at the same time patient exposure must be minimal.

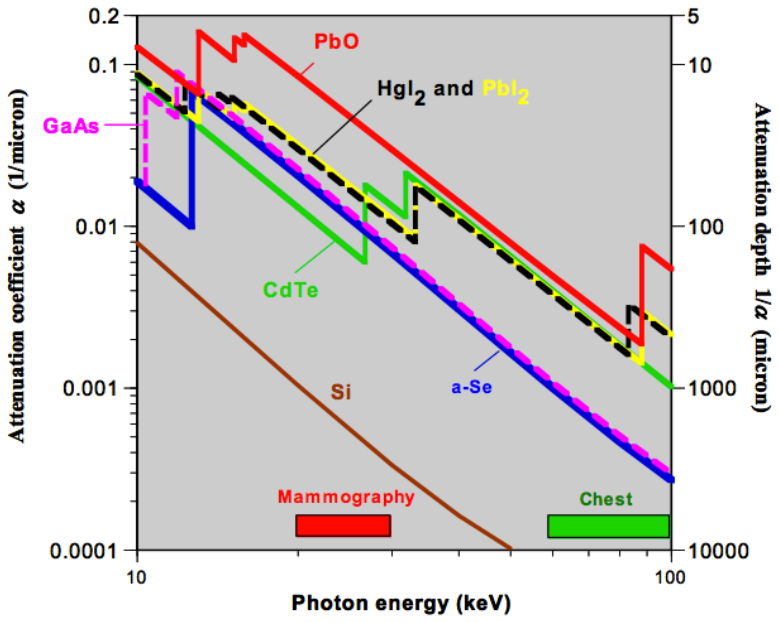

Figure 1.8 The linear attenuation coefficient α and absorption depth ($1/\alpha$) of a-Se and other semiconductors of interest as a function of the incident energy in the X-ray spectrum. (After Kasap et al. [5])

The absorption depth $\delta = 1/\alpha$ is the thickness needed to absorb 63% of the incident x-ray photons. This means to absorb sufficient x-rays, the detector thickness must be greater than the absorption depth, $L > \delta$. For example, in mammography, x-rays used typically have a mean energy of 20 keV. If the minimum detector thickness required is 2δ, the thickness of a-Se needed will be 200 μm. However, in chest radiography, x-ray mean energy is 60 keV, this will require 2000 μm of a-Se.

For the detector layer to absorb sufficient incident x-ray photons, the detector should be as thick as possible. However, there are other factors that limit the maximum thickness of the layer. First, it is expensive and technically difficult to deposit a very thick uniform layer of photoconductor without defect [18].

Also, increase in thickness requires an increase in the bias voltage. If 10V/μm operating bias is required, it implies that a detector of thickness 1000 μm will require 10vkV of bias which will introduce additional technical problems such as protecting the AMA and dielectric breakdown. Lastly, increasing the thickness of the detector increases the probability of losing generated charge carriers due to trapping before they reach the collecting electrodes. This is known as a schubweg limitation given by μτF for electrons and holes and it determines the average distance a charge carrier moved before being trapped.

1.3.3 Electron-Hole Pair Creation Energy

As the photoconductor absorbs an x-ray photon, a highly energetic electron is kick out from an inner energy level. This kicked out electron moves to the conduction band. This electron moves with a high speed through the material collides with other atoms and generates many electron-hole pairs. This implies that the absorption of a single x-ray photon can generate multiple free electrons and holes. The amount of charge ΔQ from the absorption of x-ray radiation energy ΔE is given by:

$$\Delta Q = \frac{e\Delta E}{W_{\pm}} \qquad 1.2$$

where ΔQ is the generated charge, $W_{\pm}$ is the electron-hole pair creation energy which is the amount of radiation energy absorbed by the material to create a single electron-hole pair, e is the elementary charge and ΔE is the photon energy. The value of $W_{\pm}$ must be as low as

possible to maximize the detector sensitivity because EHP creation energy is inversely proportional to detector sensitivity. Low bandgap material creates a large amount of charge upon irradiation but narrow bandgap materials have a higher conductivity which leads to higher electronic noise due to dark current [4].

Que and Rowland have shown that $W_{\pm}$ is related to the energy gap Eg of a-Se by $2.2E_g + E_{phonon}$ where the phonon energy E_{phonon} is expected to be small [14]. $W_{\pm}$ has also been shown to depend on the electric field although the exact relationship is yet to be proven [17]. In case of a-Se, $W_{\pm}$ at a given energy E decreases with increase in the electric field F and can be approximated by

$$W_{\pm} = W_{\pm}^{o} + \frac{B}{F} \qquad 1.3$$

Where $W^{\circ}_{\pm}$ is the saturated EHP creation energy at infinite applied field and B is a constant that depends on the x-ray photon energy.

1.3.4 Charge Transport and Schubweg

After the creation of charge carriers by the incident x-ray photon, the applied field across the photoconductor causes the oppositely charge carriers to separate and drift through the material. These charges become collected at the electrodes. The drift velocity is governed by the drift mobility μ and the field F. The time taken by a charge carrier to move across the sample is known as the transit time. Under ideal conditions, all the generated charge carriers are collected by the electrodes which is known as the maximum collection efficiency. Shallow traps have the effect of reducing the drift mobility. They do not affect the total collected charge. (Traps that capture and emit carriers multiple times during the transit of the carriers are considered as shallow traps.) On the other hand, there may be significant concentrations of localized electron and hole deep traps. Trapped carriers that are captured by these deep trapping centers are removed from the conduction band, become immobile and do not contribute to the collected charge signal. This reduces the x-ray sensitivity of the x-ray detector. Therefore, the carrier trapping time is the average time a carrier can travel in the photoconductor before it is captured by one of these deep traps. The reciprocal of the

charge carrier trapping time gives the probability that a charge carrier is trapped per unit time.

The carrier *Schubweg* is the product of drift mobility μ, lifetime τ and applied field F. It represents the average distance a photogenerated carrier travels before being trapped. So, ideally, a photodetector with good performance should have a thickness L such that the Schubweg is much longer than this thickness i.e. $\mu\tau F >> L$. It has been shown previously that the photoconductive layer should have sufficient thickness to absorb as many x-ray photons as possible. However, for desired performance, the thickness should be carefully chosen to fulfill the condition that

$$1/\alpha < L < \mu\tau F \qquad 1.4$$

where α is the x-ray linear attenuation coefficient at the given energy so that $1/\alpha$ is the attenuation depth at the same energy. This condition is very important because it highlights the importance of charge collection and the attenuation depth. While a thicker layer will maximize x-ray absorption, we would need a large field to achieve the right-hand side in Equation 1.4 i.e. $\mu\tau F > L$. However, increasing the applied field increases the magnitude of the dark current which reduces the signal-to-noise ratio SNR of the detector.

1.4 Research Objectives

The focus of this research work is to study the effect of x-ray irradiation on the electronic properties in the a-Se samples and the recovery process of the damage induced by x-ray irradiation. This involves investigating the effect of x-ray irradiation on the carrier trapping lifetime of holes and electrons, the dependence of x-ray dose on the carrier trapping time under different temperatures. The effect of temperature on the recovery of the carrier trapping time will also be investigated in this work.

The carrier trapping lifetime of a-Se is obtained through the interrupted field time of flight technique. This technique essentially measures the transient current caused by the carrier drift because of the applied bias across the sample. Amorphous selenium samples were sandwiched between two electrodes while an ultra-short laser pulse is used to excite the carriers in the sample. The field is interrupted when during the transient. The interruption

causes an amount of signal loss. This signal lost provides information about the carrier trapping lifetime.

It has been observed that x-ray irradiation induces defects in a-Se samples which reduces the carrier-trapping lifetime because the increase in x-ray dose causes a decrease in carrier-trapping lifetime. Because x-ray irradiation influences the carrier trapping lifetime, the dependency of x-ray dose rate on hole and electron lifetime was investigated. Previous research work has shown the dependency of temperature on the carrier trapping time, more defects were recorded for the same x-ray dose at a higher temperature. However, the induced defect by the X-ray irradiation gradually disappear with time, this is known as the lifetime recovery or relaxation process. The previous experiment has shown that hole and electron lifetime recovery process is faster at a higher temperature, this was verified in this work.

1.5 Thesis Outline and Objectives

This study is divided into five chapters. The first chapter as covered above provides a brief review on the evolution digital medical imaging techniques based on direct conversion flat panel detectors. Direct and indirect conversion x-ray image detectors have been contrasted and the advantages of direct conversion over the indirect conversion detectors have been highlighted. The necessary properties to look out for in an ideal photoconductor suitable for x-ray image detector applications have been also presented. This introductory chapter is followed by the theoretical background on the atomic structure and properties of amorphous semiconductor and their applications, a-Se. The theory behind the time of flight (TOF) and the interrupted field time of flight (IFTOF) techniques for measuring the drift mobility and lifetime (deep trap capture time) for both holes and electrons is introduced. Chapter three describes the experimental procedures, sample preparations and experimental set-up with a brief description of each equipment that makes up the whole experimental set-up. The results of the experiments, techniques used in analyzing these results and discussion of the results are presented in chapter four. Chapter five provides the conclusions and suggestions for future work based on this thesis.

2. THEORY

2.1 Amorphous Selenium Structures and Properties

2.1.1 Introduction

Amorphous selenium was first commercialized in xerography. Xerography, also known as electrophotography, is a dry photocopying process in which black or colored powder sticks to electrically charged surface after its exposure to light from an image of the document to be copied [19]. Its application in xerography led to intensive study of the properties of a-Se and its alloys during the 1960s and 1970s. The pace of research on a-Se as a xerographic material was slowed down by the advent of organic photoconductors. However, the research on a-Se has recently been revived because of interest in the development of digital flat panel X-ray detectors using a-Se for medical imaging applications. The term amorphous selenium in the context of a photoconductor implies "stabilized a-Se", which is a-Se alloyed with 0.2-1% As and doped with 0-10 ppm Cl. The arsenic alloying diminishes the crystallization tendency of pure a-Se and the halogen addition ensures that the hole transport properties are preserved i.e. Cl compensates for As-induced hole deep traps. Amorphous selenium can easily convert incident X-ray photons to electronic charge carriers, which is the fundamental principle of the direct conversion technique employed in flat panel X-ray imagers (FPXIs). Amorphous selenium can be easily deposited over a large surface area. To optimize the performance of a device using a-Se as its photoconductor, a good understanding of the electronic and optical properties of a-Se is necessary.

The theory behind the properties of materials can be explained by the application of quantum mechanics to the bonding arrangement of the atoms in the material; the field of solid state physics. However, the framework of predicting the properties of crystalline solids cannot be applied to a-Se because because the structure is non-periodic. Therefore, electronic band structures of amorphous solids are derived by observing their similarities to crystalline semiconductors and observations from experiments of their electronic and optical properties. Time of flight (TOF) and interrupted field time of flight (IFTOF)

measurement techniques have been used to study the electronic properties of doped and undoped a-Se and its alloys. Electronic charge carrier transportation in the bulk structure of a-Se can be examined by the TOF/IFTOF measurement techniques.

2.1.2 Structure of Amorphous Solid

A solid is made up of a three-dimensional network of atoms interconnected by atomic bonds. The atomic bond is formed in a semiconductor when two or more atoms share their valence electrons to complete the subshell of each atom which results in a more energetically stable structure. Figure 2.1 shows the bonding arrangement for a crystalline and amorphous semiconductor. The equilibrium position of each atom in the crystal is represented by the dots and the lines between the dots represent the bond between an atom and one of its nearest neighbors.

For crystalline semiconductors, the structure has an ordered arrangement of atoms as shown in Figure 2.1 (a). The number of bonds formed by each atom and their angles is well defined throughout the material which gives rise to a periodic structure. The wave function of each electron also overlaps neighboring wave functions and extends throughout the material

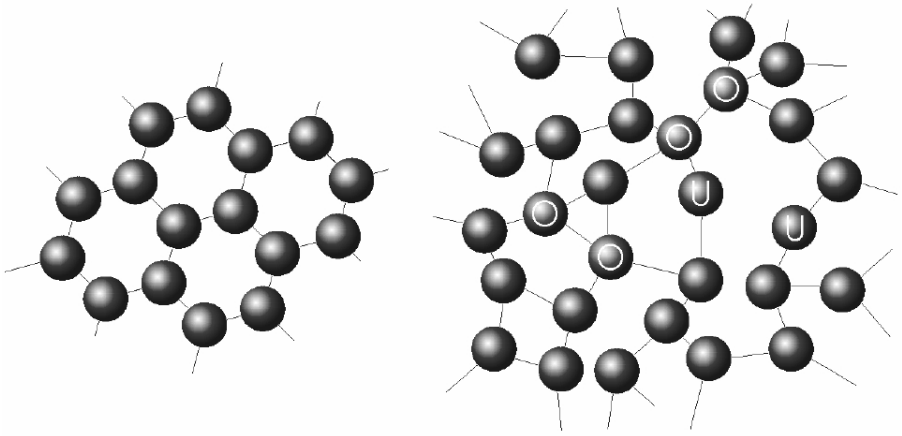

Figure 2.1 Two-dimensional representation of the structure of (a) a crystalline solid; (b) an amorphous solid. Spheres mark “O” and “U” represent over-coordinated and under-coordinated atoms respectively. (After Fogal [6]).

forming covalent bond [8]. The number of nearest neighbors to a given atom is known as the coordination number of that atom. Each atom in a crystalline semiconductor has the same coordination number with identical bond length and bond angles between bonds.

An amorphous semiconductor, on the other hand, has a more complex structure than the crystalline semiconductor has depicted in Figure 2.1 (b). The differences from the crystalline state are due to the slight variation in the bond length and bond angle between the atoms in the network. This eliminates any periodicity after a few atomic radii and the coordination number is not the same for each atom. There is only short-range order in amorphous semiconductors. Each atom still maintains its normal valence requirement making amorphous semiconductors have a similar electronic structure as that of the corresponding crystalline semiconductor. The overall disorder in amorphous solid gives rise to several localized states. The electronic and optical properties of amorphous solids are influenced by the energy level and density of these localized states.

There are defects in both crystalline and amorphous semiconductors. The defect in crystalline solids occurs when an atom is out of its equilibrium position. But in amorphous semiconductors, defects occur when there are abnormal coordinate numbers. A defect in the amorphous semiconductor is an atom with a different number of bonds as shown in Figure 2.1 (b), either too many or too few bonds. The normal coordination number is 3 but one can see atoms with coordination number 2 and 4; under and over coordinated atoms. Some atoms have four bonds each, these are over-coordinated atoms labeled as “O” and some have two bonds which are known as the under-coordinated atoms are labeled as “U”. Bothe over-coordinated and under-coordinated atoms introduce localized electronic states.

2.1.3 Band Theory for Amorphous Semiconductors

A very important concept in solid-state physics used to explain the electronic and optical properties of a semiconductor is the band model. The band model theory has its basis in quantum mechanics based on treating solids as a collection of a large number of atoms with a specific arrangement [8]. Quantum mechanics explains that a single atom has an electron

with energy state that is quantized through the solution of Schrodinger equation for a single atom into discrete energy states or levels. A solid is formed when a large number of atoms are brought together in close proximity and the electron energy levels relate to an individual atom in a way that a continuous band of energy state is formed. The formed band state is described by a function known as the density of state g(E) which is defined as the number of electron states per unit energy per electron at energy E.

Figure 2.2 below shows four different models of the density of state distribution of different phase of solid. One of the most simplified models for the density of state of a crystalline semiconductor is shown in Figure 2.2 (a). The main concept considered in this model is the periodicity of the crystalline structure. The band diagram shows two bands of energy states separated by a region known as the band gap. The lower band is filled up with electrons involved in covalent bonding of the semiconductor known as the valence band.

The upper band is almost completely without electron until an electron gains enough energy to move through the band gap to become mobile and contribute to electrical current. The band gap is the energy difference between conduction band energy E_c and valence band energy E_v. Crystalline semiconductors have long-range order properties, which makes it simpler to develop a density of state model compared to amorphous semiconductors. Developing an electronic structure for amorphous semiconductors are relatively more difficult because of the absence of long-range order. However, amorphous solids have the same basic electronic and optical properties as their crystalline counterparts because only short-range order in the atomic structure was applied in the band theory [20]

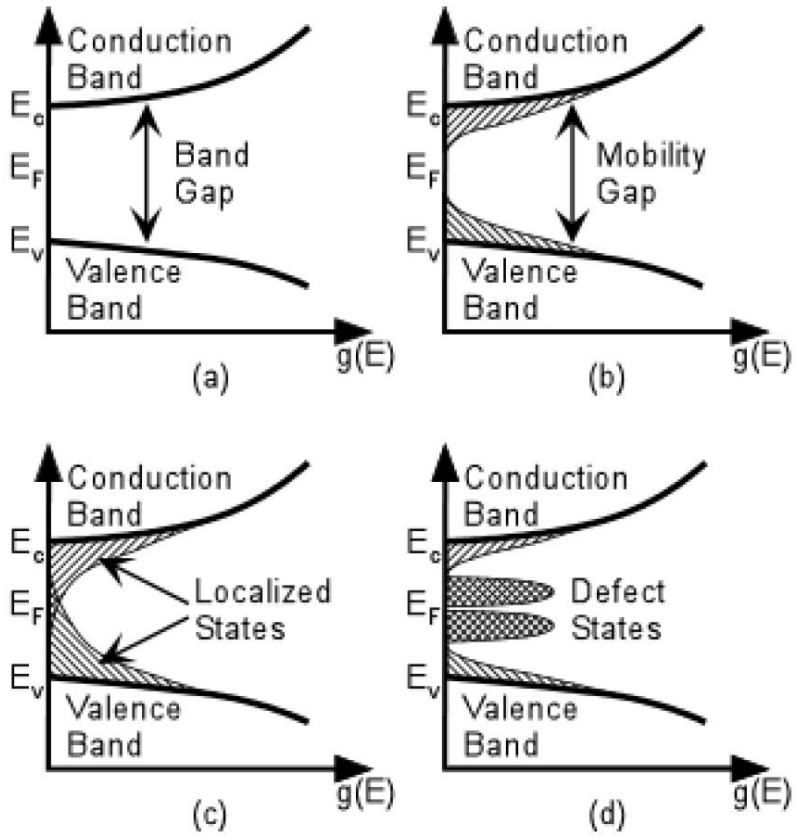

Figure 2.2 Density of states models for crystalline and amorphous semiconductors. (a) Crystalline semiconductor: two bands separated by a forbidden energy region. (b) Initial DOS model for amorphous semiconductors; localized states encroach into the band gap. (c) The CFO model; the localized states extend all the way into the band gap and overlap. (d) Marshal and Owen model; structural defects create many localized states deep in the band gap.

The density of states N(*E*) is a fundamental characteristic of both crystalline and non-crystalline solids. N.F Mott attempted to explain the density of states by modifying that of crystalline semiconductors [21]. Mott argued that electrons in a crystalline solid could be described by extended Bloch wave functions with long-range order both in magnitude and phase. He suggested however that in amorphous semiconductors, the extended Bloch wave function has a long-range order in magnitude but only short-range order in phase, which gives rise to localized electron states into the band gap. This is shown in Figure 2.2 (b), the tails of localized states begin at the edges of band E_c and E_v and extend into the band gap.

Mott's explanation was based on P.W. Anderson's work, in 1958, showed that sufficient disorder could produce characteristic solutions to the Schrodinger equation that are localized in space [22]. Mott further argued that the transition from the localized tail states to the extended band states is well defined [23].

An improvement on the Mott's model was presented by Cohen, Fritzsche and Ovshinsky [24]. They argued that there is more to the effects disorder in an amorphous semiconductor because there could also be compositional disorder, that is, topological and composition disorder can contribute significantly to the disorder. The latter arguments have lead them to suggest that the localized tail states extend much deeper into the band gap and even overlap in the Fermi level region as depicted in Figure 2.2 (c). Metallic properties are not expected though because there is a continuum of electron states throughout the gap. This is because the gap states are highly localized in space. This model is known as the CFO model.

Furthermore, the presence of over-coordinated and under-coordinated atoms in amorphous semiconductors may cause some local defect such as dangling bonds, chain ends, vacancies, substitutional impurities, and interstitials. These defects contribute to additional localized states within the mobility gap. These contributions are taken care of by another model proposed by Marshal and Owen. In this model, the Fermi level is determined by these defect states, the donor-like and acceptor-like in the upper and lower half of the gap respectively. The concentrations of the donor and acceptor states are adjusted by a self-compensation mechanism which keeps the Fermi level near the middle of the band gap.

2.1.4 The Atomic Structure of Amorphous Selenium

Selenium has an atomic number of 34, with an electronic configuration $1s^2 2s^2 2p^6 3s^2 3p^6 3d^{10} 4s^2 4p^4$ and belongs to a group of elements known as chalcogens which are in group six of the periodic table. Selenium has six electrons in its outermost shell which can occupy eight states, two in the s-state and up to six in the p-state. The two electrons in the s-states form a lone pair and do not contribute to bonding. There is another lone pair in the p-state which is also a non-binding state which leaves only two electrons in the p-state

available for covalent bonding. Therefore, the lowest energy configuration for Se atoms has a two-fold coordinated bonding structure with an optimum bond angle of 105^{o} and dihedral angle of 102^{o} [25]. The solid phase of selenium has several forms. The crystalline form exists in one of two possible phases because of the two fold coordinated bonding. The phases of existence include the α-monoclinic Se (α-Se) and trigonal Se (ϒ-Se). In α-Se, the atoms bond in a way where eight atoms form a ring (Se_8) while in ϒ-Se, the atoms are arranged in a "parallel fashion" and spiral Se_n molecular chains. The amorphous state, on the other hand, was initially assumed to be made up of a mixture of chain-like and ring-like formations distributed randomly within the solid. Some observation of a-Se structural properties later suggested a more accurate model based on a meandering chain model in which atoms are linked together in a two-fold coordinated chain structure but the changes in the dihedral angle lead to regions within a chain that are ring-like i.e. fragments of Se_8. In this structure, the magnitude of the dihedral angle ϕ is constant although it changes sign randomly. The dihedral angle, as shown in Figure 2.3, is the angle that exists between two adjacent planes of bonding. The angle involves four atoms and two planes as shown in Figure 2.3 [25][26]

In the crystalline phase of selenium, the atomic positions are fixed because of the symmetry, bond length, and bond angle. The magnitude of the dihedral angle is a function of the bond length and bond angle, and its sign depends on the type of crystalline Se under consideration. For α-Se, the sign of the dihedral angle changes (alternates) to form a ring structure. In ϒ-Se, on the other hand, the sign remains the same to form a spiral structure. In a-Se, it changes randomly to form either ring-like or chain-like structures. If + and – are used to represent the relative phase of φ, a ring-like structure is expressed as +-+- and a chain-like structure is represented as ++++ or ----. Figure 2.4 shows a structure of a-Se which is characterized by + + + - + - + - - - with the assumption of only local molecular order within the Se chain.

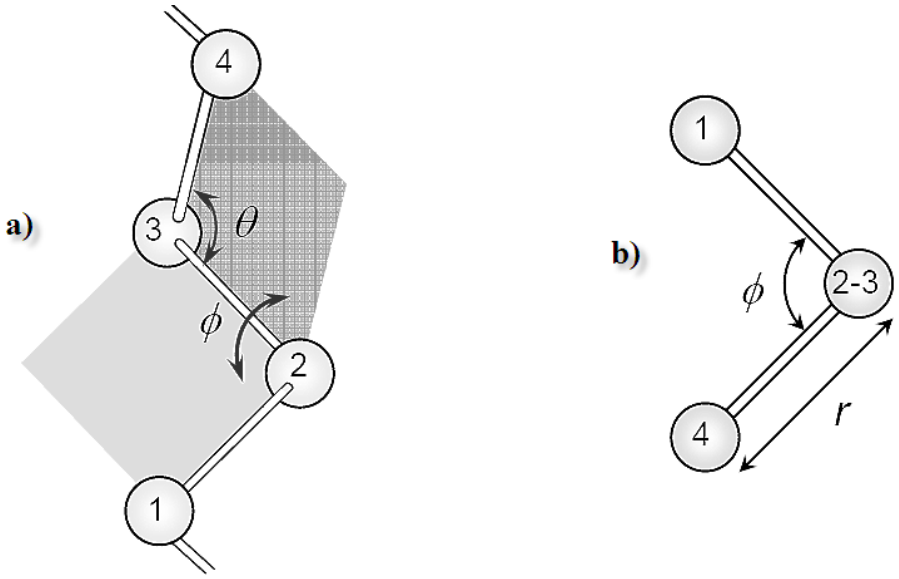

Figure 2.3 Definition of dihedral angle in selenium random chain model. (a) Dihedral angle formed between two planes of atoms 123 and 234. (b) Looking down on the bond joining atoms 2 and 3. The bond angle θ and the bong length *r* [25]

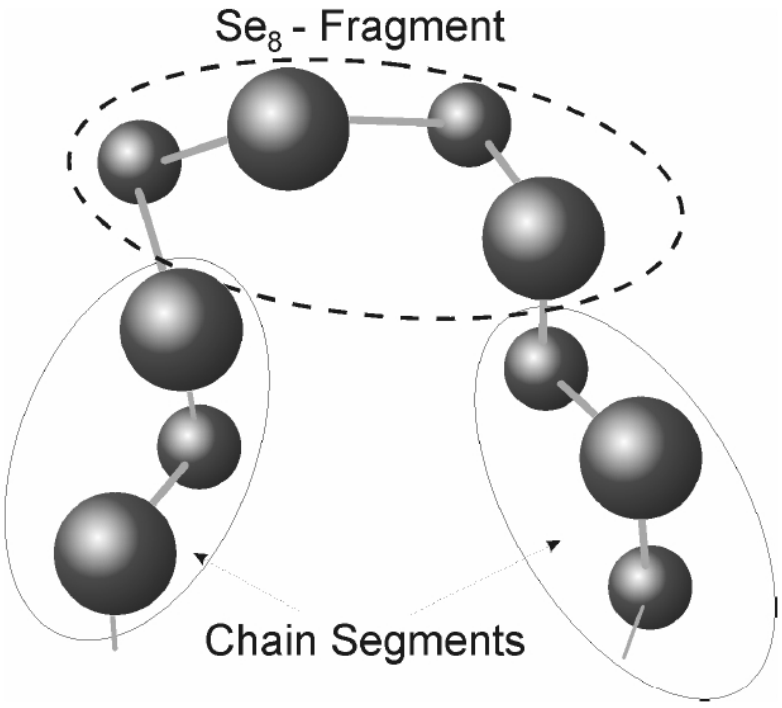

Figure 2.4 A Random model of a-Se depicting chain-like and ring-like regions in a meandering chains model. After Lukovsky [25]

As presented in the previous section, some atomic configuration in a-Se are over-coordinated and under-coordinated which contribute to structural defects in a-Se. Some of these defects are electrically charged while some others are not although Electron Spin.

Resonance studies show that for a-Se, the chance of having a neutral defect is small [8][10]. However, most of the defects are from thermodynamically derived charged structural defects known as valence alternation pairs (VAPs) which are common in most chalcogenide glasses. VAPs are either positively charged three-fold Se atom Se_2^+ or negatively charged one-fold Se atom Se_0^-. VAPs can also form intimate valence alternative pairs (IVAPs) close proximity. Figure 2.5 shows the structure and energy of several simple bonding arrangements of selenium and the possible defect formed by selenium atoms are depicted in Figure 2.6 below. [27][28][4].

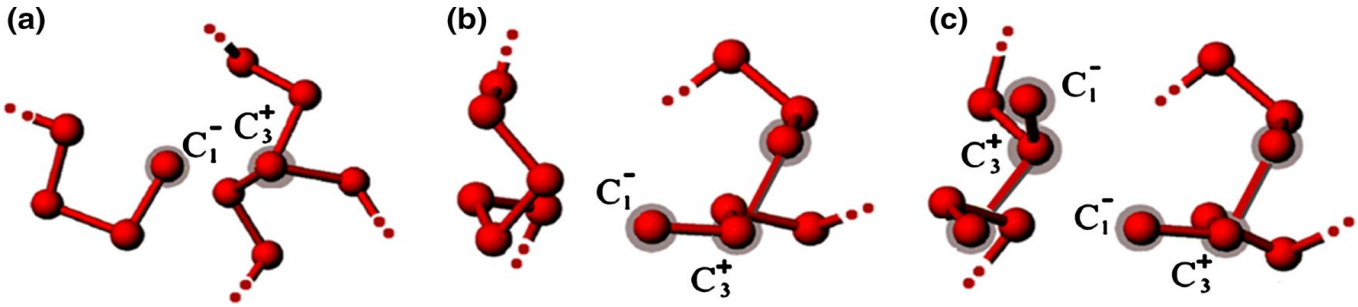

Figure 2.5 The structure and energy of simple bonding configurations for selenium atoms. Straight lines represent bonding orbitals, lobes represent lone-pair (nonbonding) orbitals, and circles represent antibonding orbitals. The energy of a lone-pair is taken as the zero energy. This Figure is adapted from [64]

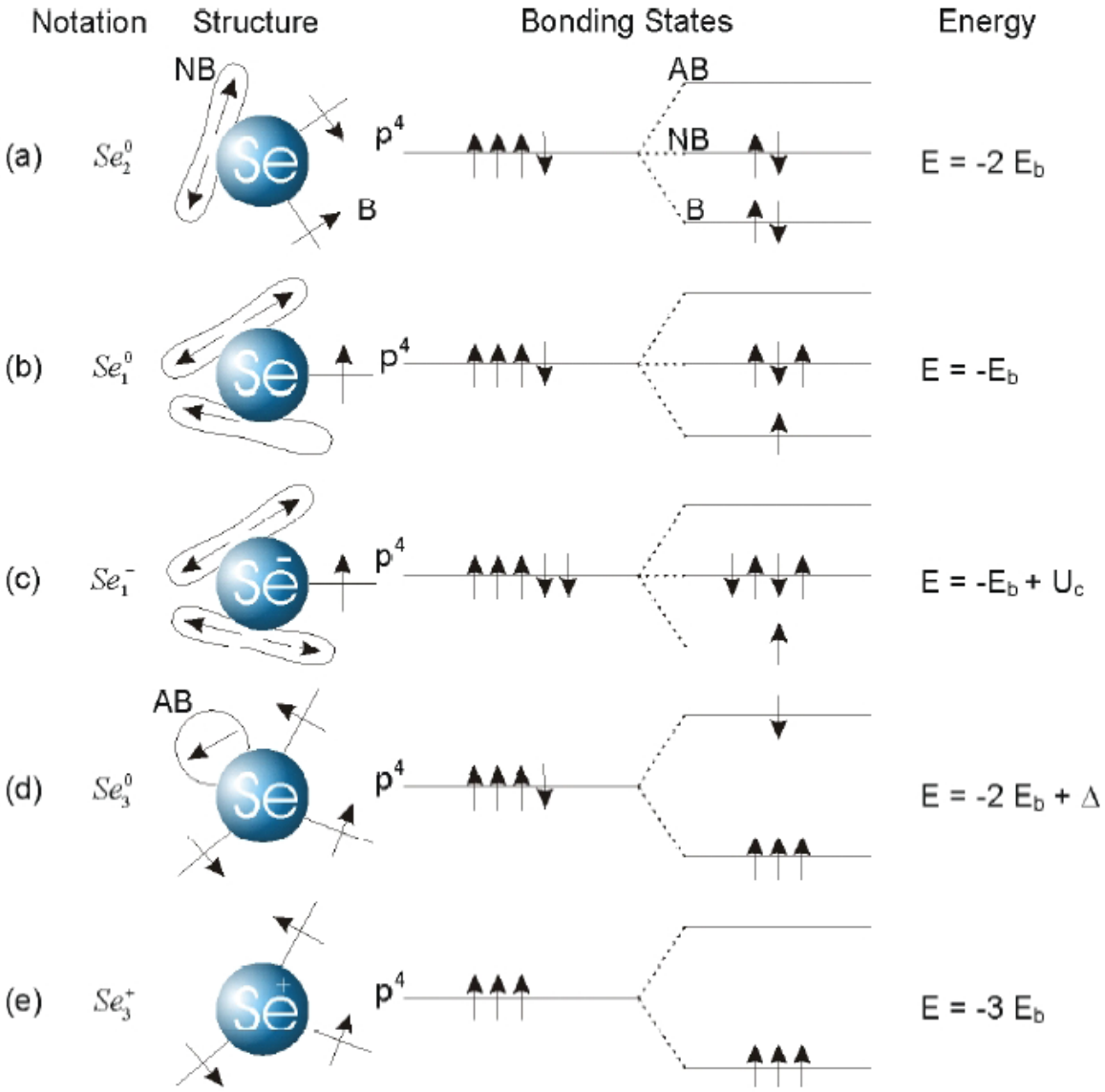

Figure 2.6 The VAP defects with a distribution of a net charge a) two chain VAPs defects. b) Single IVAP defects while a one-fold coordinated negatively charged Se atom C_1^- and a three-fold coordinated positively charged Se atom C_1^+ are on the same side. c) Two IVAPs belongs to different chains and form a common one. Adapted from Kastner et al [34]

2.15 Density of State of a-Se and Carrier Transport in a-Se

There are quite a number of density of state models for a-Se and the Abkowitz model proposed in 1988 has been commonly used [29]. This particular model is shown in figure 2.7. The Abkowitz model is more likely an improved version of Owen-Marshal model with two peaks, which represent localized states, close to the valence and conduction band known as the shallow traps.

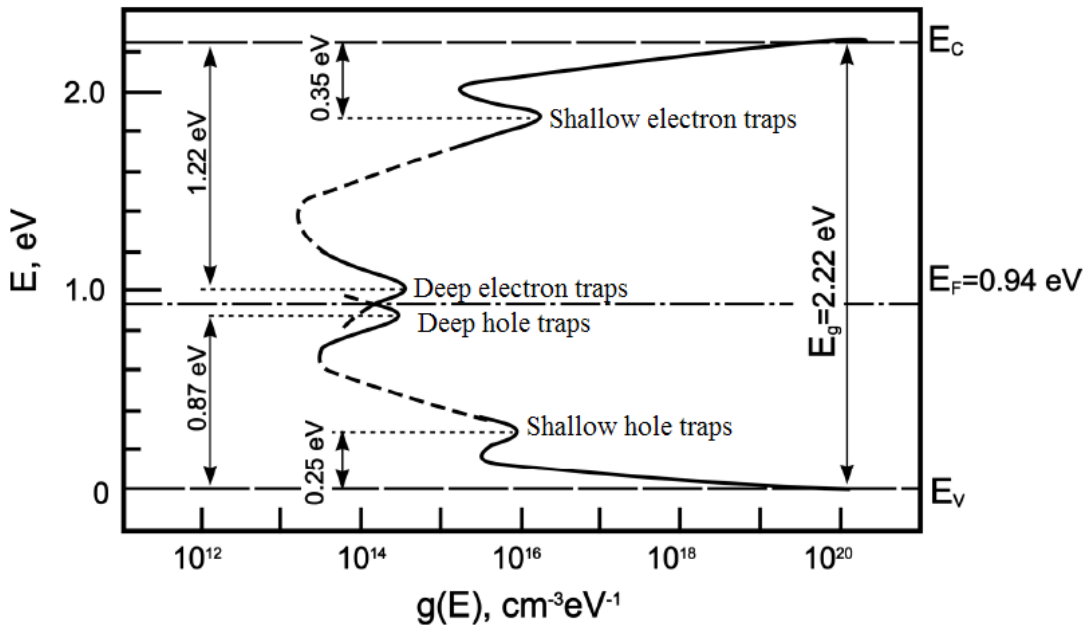

Figure 2.7 Density of State model suggested by Abkowitz. (After Abkowitz [29])

The shallow traps are those localized states that are close to the conduction band for electrons and close to the valence band for holes. The model depicts another set of two peaks near the Fermi level corresponding to deep traps. The mobility gap for a-Se based on the Abkowitz model is 2.22 *e*V [32]. The horizontal peak near but above the Fermi level is the deep electron traps and the horizontal peak below the Fermi level is the deep hole traps This model has been proposed from several experiments such as the Time-of-Flight (TOF)

transient photoconductivity, xerographic cycled-up residual voltage decay and xerographic dark discharge [8]. Experimental observations suggest that the electron mobility and hole mobility in a-Se is controlled by shallow traps through capture and release processes [30]. Equation 2.1 expresses the carrier mobility of a-Se with a discrete set of monoenergetic shallow traps at an energy level E_t from the transport band edge e.g. E_v [16].

$$\mu = \mu_o \left[1 + \frac{N_t}{N_v} \exp\left(-\frac{E_t}{kT}\right)\right]^{-1} \tag{2.1}$$

where $N_t$is the shallow trap concentration, N_v is the density of state at the valence band mobility edge and E is the energy depth of the shallow traps from the E_v.

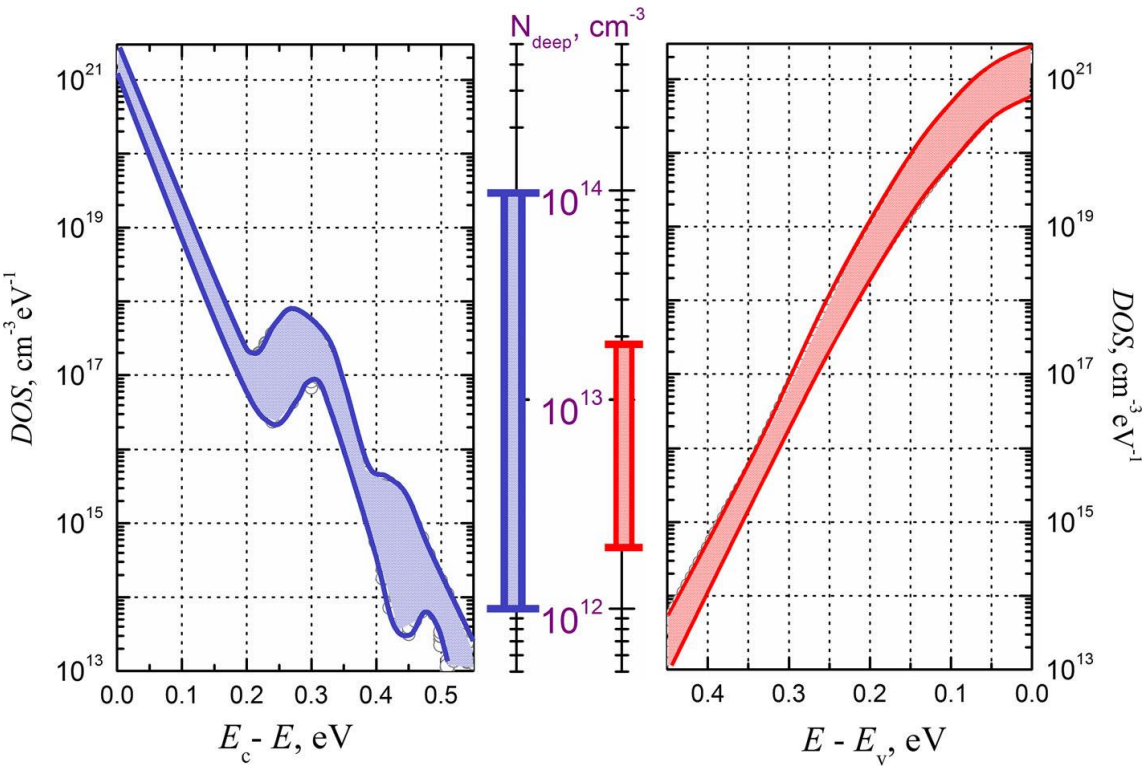

(a) (b)

Figure 2.8 Generalized DOS model. (a) DOS around conduction band. (b) DOS around valence band. The bars in the center depict the concentration of deep carrier traps for both electrons and holes. (After Kasap et al [31])

The density of state for shallow traps and their energy levels are major factors that determine the carrier mobility in a-Se. Experimental measurements based on Abkowitz's model has shown that the peak of shallow hole traps is roughly 0.29 *e*V above the valence band and the peak of shallow electron traps is 0.35 *e*V below the conduction band [31][32]. Photoinduced discharge measurement and cycled-up xerographic residual voltage measurements techniques have been employed to measure peaks of deep traps [33]. The deep hole traps were found to be roughly 0.87 *e*V above valence band and the peak of the deep electron traps is 1.22 *e*V below the conduction band [31]. Recently, Kasap et al [34] presented a more detailed study of shallow carrier distribution which gave slightly different results from the previous studies. Previous and recent studies suggest that the energy of the deep carrier trap is at least 0.55 *e*V away from the band edge. The recent study revealed that there are two Gaussian peaks near the conduction band and no Gaussian peaks near the valence band.

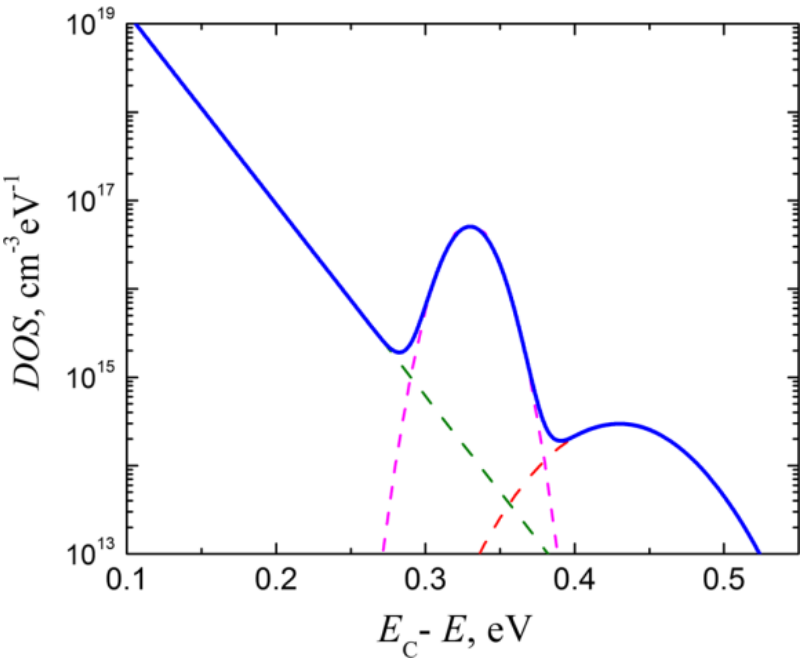

Figure 2.9 Density of State distribution for shallow traps. One peak is observed 0.27 – 0.33 *e*V below the band edge. Another Gaussian peak is observed 0.38 – 0.48 *e*V below the band edge. (After Kasap et al [31]).

The recent model suggests a distribution in the near band edge region and a number of deep traps in the mobility gap as shown in Figure 2.8 [31]. Both shallow and deep carrier traps have been proven to be generated by structural defects and are thermodynamically stable at room temperature [32][35]. Deep traps in the mobility gap control the carrier lifetime which can affect the carrier schubweg $\mu\tau F$, significantly which will eventually affect the photoconductor x-ray sensitivity as discussed in Chapter 1. Improving the performance of photoconductors involves an improvement in the carriers' transportation and structural stability of the semiconductor material. In the case of a-Se, alloying and addition of impurities have proven to improve stability and carrier transport properties. Arsenic has been considered as good alloys in improving the thermal stability. When a-Se is alloyed with As, the hole transport becomes worse but can be restored by the addition of a halogen dopant such as Cl in the part per million (ppm) amounts. Thus, combination alloying with As and doping with Cl allow a good control over the charge transport parameters of a-Se [36].

2.1.6 Optical Properties of a-Se

Amorphous selenium conducts a photocurrent when exposed to light due to the creation of free charge carriers; this makes it a photoconductor. Charge carriers are created when incident photons with sufficient energy excite electrons from the valence band into the conduction band. The optical absorption coefficient α describes the rate at which photons are absorbed as light propagates through the medium. This coefficient is a function of the wavelength of the incident light and the magnitude of the density of state at the band edge [10]. In the case of a-Se, it has been observed experimentally that the optical absorption coefficient exhibits an Urbach edge of the form [37]

$$\alpha(\mathrm{E}) = 7.35 \times 10^{-12} \exp\left(\frac{E}{\Delta E}\right) \mathrm{cm}^{-1} \qquad (2.2)$$

where

$$E = h\nu \qquad (2.3)$$

and ΔE is the so-called Urbach width which is typically about 58 m*e*V in a-Se.

The Urbach edge behavior in Equation 2.2 is common nearly to all amorphous semiconductors. The main parameter that varies from one to another amorphous semiconductor is the Urbach width. At higher photon energies, the absorption coefficient represents transition from tail or extended states in the valence band to tail or extended state in the conduction band and has a distinctly different form than in Equation 2.2. Davis suggested that at higher photon energies, the absorption coefficient follows a different pattern.

$$\alpha(E) = B(E - E_0) \tag{2.4}$$

where E_0 is the optical band gap at room temperature typically in the range of 1.99 – 2.05 eV [37].

This behavior has been linked to the sudden rise in the density of state at the band edge. According to Tauc's law written in the form

$$\alpha(E) = B(E - E_0)^r \tag{2.5}$$

where $E_0 \approx 2.0$ eV and r is the curve fitting parameter which depends on the data range and close to unity [38].

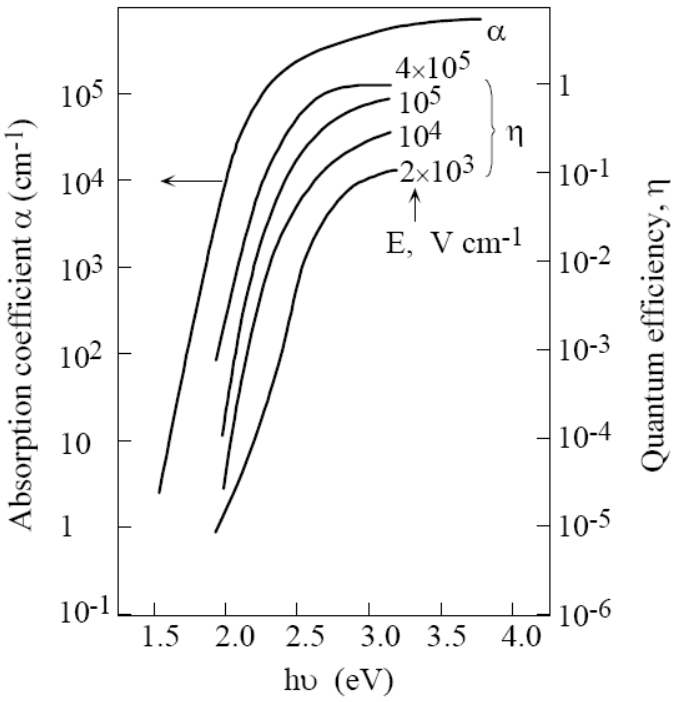

Figure 2.10 Absorption coefficient and quantum efficiency as a function of incident photon energy (hv) for the various applied fields. (After [39]).

When photons are absorbed, electron-hole pairs (EHP) are generated. An electron is excited from the valence band into the conduction band which leaves a void in the valence band – a hole. In the presence of an external field, the generated charge carriers may contribute to electric current conduction. The probability that a generated EHP is separated by the external electric field is determined by the quantum efficiency. Some electron-hole pairs generated recombines and do not contribute to conduction. Studies have shown that the quantum efficiency in a-Se has a strong dependence on the field. This is depicted in Figure 2.10. Onsage theory for the dissociation of photogenerated EHPs explains the mechanism behind the field dependence of quantum efficiency in a-Se. Onsage explains that the quantum efficiency through [39]

$$\eta = \eta_0 f(E, T, r_0) \tag{2.6}$$

where $\eta_0$is the quantum efficiency for the intrinsic photon generation process and $f(E,T,r_0)$is the probability that an EHP will separate and r_0 is the initial separation of the photo-induced pair.

2.2 X-ray Absorption

X-rays are ionizing radiation in the electromagnetic spectrum with photon energy ranging from 100 eV to 100 keV. The electromagnetic spectrum is the range of frequencies of electromagnetic radiations and their respective wavelengths and photon energies. The x-ray source used for this work is a tungsten x-ray tube which means Bremsstrahlung radiation is the major mechanism for x-ray production. As explained by the classical theory, an accelerated charged particle radiates electromagnetic energy. Bremsstrahlung radiation is produced when energetic electrons are incident on a metal target [9]. A typical X-ray energy spectrum of a medical X-ray tube is shown in Figure 2.11. The interaction of X-ray with matter exists in different ways. These are photoelectric absorption, coherent scattering, Compton scattering and pair production. Photoelectric absorption and Compton scattering are the major interactions employed for medical applications [40].

In the photoelectric absorption, the incident X-ray photon interacts with an electron in the inner shell of an atom and the energy of the photon is transferred to the electron. If the energy of the incident X-ray is greater than the electron binding energy, the electron is excited and removed from the inner shell. The absorbed photon energy is then converted to kinetic energy of the electron. In Compton scattering, X-ray photon is deflected instead of being absorbed. It involves incoherent scattering of an x-ray photon by an electron in the outer shell. Compton scattering typically occurs at higher x-ray energies. X-ray photon collides with an outer shell electron and the electron gets excited and recoils. The energy

loss in the X-ray photon is converted to electron kinetic energy and energy dissipated for overcoming the binding energy.

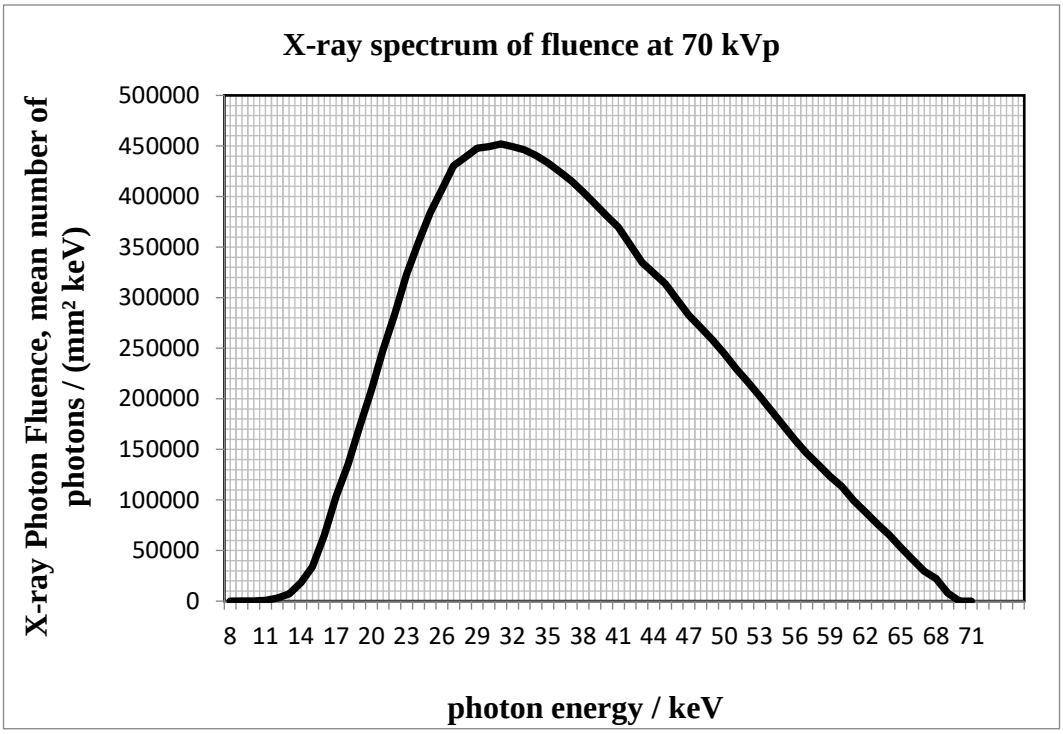

Figure 2.11 A typical X-ray Spectrum produced from a tungsten X-ray tube at 70 kVp
Source: X-ray spectrum simulation program by Siemens for dose of 1 mGy. [41]

X-ray dose is the energy per unit mass absorbed by the sample object. It is the measure of the x-ray energy density absorbed by the sample. The dose is a very useful parameter to study the effect of X-ray in a-Se X-ray photoconductors. Computing the absorbed X-ray dose in a sample involves calculating the energy deposited into the sample which involves both mass attenuation coefficient μ/ρ, energy absorption coefficient μ_{en}/ρ, quantum efficiency $1 - \exp(-\mu L)$ and the incident photon fluence Φ (E). The unit of the dose is Gray which is defined as the absorbed energy (J) per unit mass (kg) of the sample object (1 Gy = 1J/kg). The absorbed dose D is given by;

$$D = E_{\text{absorbed}}/M \tag{2.7}$$

where E_{absorbed} is the mean energy absorbed from the radiation and M is the mass of the body in which the radiation is incident on.

When an ionizing radiation, X-ray as a typical example, is expose in the air, it impart sufficient energy to ionize charge. The amount of radiation that needed to impart enough energy to 1 cm^3 of air to ionize 0.33 nC of charge at standard temperature and pressure (STP) is known as a unit Roentgen, R. Dose in air and exposure both refer to a given amount of air, and can be converted from one to the other. One Roentgen of exposure at STP is equivalent to depositing 8.77×10^{-3} J into 1 kg of air. Therefore, 1 R = 8.77 mGy; or 1 mGy = 114 mR.

The actual energy E_{absorbed} deposited into a medium by each photon of a high energy radiation of photon energy E is defined by [9]

$$E_{\text{absorbed}} = E\,\frac{(\mu_{\text{en}}/\rho)}{(\mu/\rho)} \tag{2.8}$$

where μ_{en}/ρ is the mass energy absorption coefficient of the medium and μ/ρ is the mass attenuation coefficient. The energy absorption coefficient μ_{en} is a fraction of coefficient μ transferred from the incident photons to the kinetic energy of the electron, through photoelectric and Compton interaction, and lost by radiation as electrons decelerate. The linear attenuation coefficient μ which is defined by the fraction of radiation lost by absorbing and scattering per unit thickness of an object and it depends on the energy E, density ρ, and the atomic number Z, that is $\mu = \mu(E, \rho, Z)$. It has been found that for high energy radiation, μ depends linearly on the density ρ. The linear attenuation coefficient $\mu(E)$ at photon energy E is given by [42]

$$\mu(E) = -\frac{1}{N(E)}.\frac{dN(E)}{dz} \tag{2.9}$$

where $N(E)$ is the number of photons each with energy E travelling in the direction along z in a medium. Integrating Equation (2.9) gives the number of photons at z as

$$N = N_0 \exp[-\mu(E)z] \tag{2.10}$$

where N_0 is the number of photon at $z = 0$.

The attenuation fraction also known as the quantum efficiency η_Q describes the fraction of the incident photons that are attenuated by a photoconductor. The quantum efficiency η_Q depends on the linear attenuation coefficient μ of the photoconductor and its thickness L and is given by

$$\eta_Q = 1 - \exp(-\mu L) \tag{2.11}$$

Combining Equations2.8 to 2.11, the energy absorbed up to a maximum energy E_{max} is given by

$$E_{\text{absorbed}} = \int_0^{E_{\max}} \Phi(E) E \frac{\mu_{\text{en}}/\rho}{\mu/\rho} [1 - \exp(-\mu L)] dE \tag{2.12}$$

where $\Phi(E)$ is the photon concentration per unit area per unit energy. An ideal X-ray photon fluence $\Phi(E)$ was obtained from the Siemens website as shown in Figure 2.11 [41].

The fluence obtained from the Siemens website is calibrated by measuring the exposure rates in air at 70 kVp, $D_{\text{air exp}}$ from the Keythley ion chamber and divide it by the ideal dose in air at 70 kVp, $D_{\text{air ideal}}$. The factor $D_{\text{air exp}}/ D_{\text{air ideal}}$ is used as the calibration factor to normalize the ideal X-ray fluence simulated from the Siemens website to the equivalent experimental value.

$$\Phi(E)_{\text{exp}} = \frac{D_{\text{air exp}}}{D_{\text{air ideal}}} \times \Phi(E)_{\text{ ideal}} \tag{2.13}$$

where $\Phi(E)_{\text{ideal}}$ is the simulated X-ray fluence, $\Phi(E)_{\text{exp}}$ is the calibrated experimental X-ray fluence. The ideal X-ray dose in the air is given by the following expressions:

$$D_{\text{air ideal}} = \frac{E_{\text{absorbed,air}}}{M_{\text{air}}} \tag{2.14a}$$

From Equation 2.12, $E_{\text{absorbed,air}}$ is expressed as

$$E_{\text{absorbed,air}} = \int_0^{E_{\max}} \Phi(E) E \frac{\mu_{\text{en,air}}/\rho_{\text{air}}}{\mu_{\text{air}}/\rho_{\text{air}}} [1 - \exp(-\mu_{\text{air}} L_{\text{air}})] dE \quad (2.14b)$$

The experimental dose in the air $D_{\text{air exp}}$ is the readout from the dosimeter in units of Roentgen. The absorbed dose in selenium is calculated by

$$D_{\text{Se exp}} = \frac{D_{\text{air exp}}}{D_{\text{air ideal}}} \times D_{\text{Se,ideal}} \quad (2.15a)$$

where

$$D_{\text{Se,ideal}} = \int_0^{E_{\max}} \Phi(E)_{\text{ideal}} E \frac{\mu_{\text{en,Se}}/\rho_{\text{Se}}}{\mu_{\text{Se}}/\rho_{\text{Se}}} [1 - \exp(-\mu_{\text{Se}} L_{\text{Se}})] dE / M_{\text{Se}} \quad (2.15b)$$

2.3 Time-of-Flight and Interrupted-Field Time-of-Flight Transient Photoconductivity

2.3.1 Introduction

In the previous sections, the reasons for a-Se being one of the most suitable semiconductors for flat panel X-ray detector have been presented. Charge transport properties of semiconductors determine the electronic device performance. For this reason, we need to measure the charge transport parameter of a semiconductor used in an electronic device to understand its performance. For this research work, time of flight (TOF) and interrupted field time of flight (IFTOF) transient photoconductivity measurement techniques have been employed in studying the charge transport properties of a-Se. Time of flight measurement technique is used to measure the drift mobility of charge carriers while the interrupted field time of flight technique measures the carrier lifetime (deep trap capture time) in high resistivity semiconductors. Both the TOF and IFTOF involve monitoring the photocurrent transient produced by the drift of photoinjected carriers in the sample introduced by a very

short photoexcitation. The principles of the TOF and IFTOF measurement techniques are presented in this section.

2.3.2 The Time-of-Flight Measurement Technique

The time of flight method measures the transient current (photocurrent) produced by the drift of photo-injected carriers moving through a highly resistive medium. Figure 2.12 shows the schematic of the TOF method.

The photo-conducting material with thickness *L* is placed between two electrode plates A and B with plate A connected to a voltage source and B connected to a grounded sampling resistor *R*. Resistor *R* is chosen such that majority of the voltage drops across the highly resistive sample. In some cases, a non-injecting blocking layer is placed between the top electrode and the photo-conducting material to prevent charge injection from the contact. Charge carriers are excited by a short pulse of excitation radiation which upon absorption, generates electron-hole pairs under the top electrode. If the top electrode is transparent or semi-transparent, an optical excitation may be used [8].

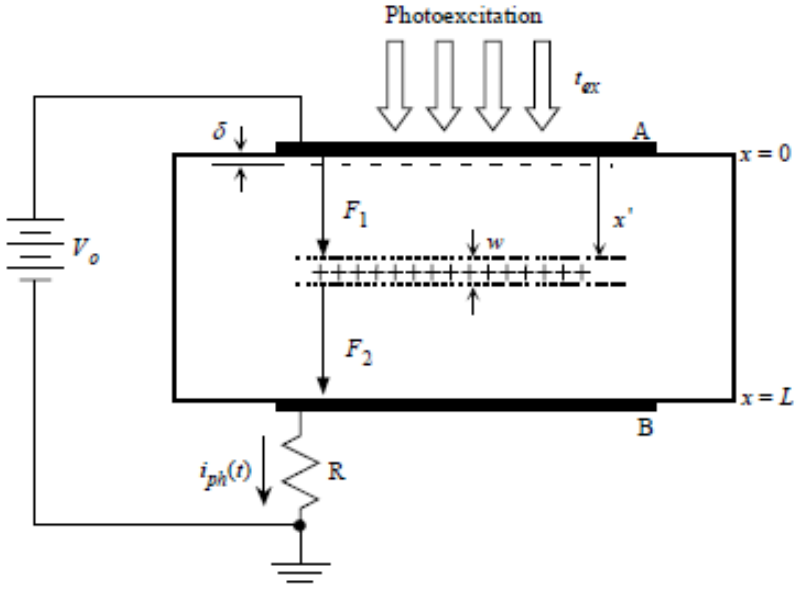

Figure 2.12 Schematic diagram of the TOF measurement technique.

The wavelength of the excitation source is chosen such that the absorption depth δ of the radiation is negligible compared with the sample thickness L. This ensures an immediate collection of electrons at the top electrode A while holes are drifted across the sample and collected by electrode B. A photocurrent $i_{ph}(t)$ is generated through the external resistor R by the drifting of holes across the sample. This photocurrent can easily be measured. The electron photocurrent can similarly be measured by reversing the polarity of the applied voltage to the sample.

For a valid TOF measurement, certain criteria must be met in the choice of the light excitation source. Firstly, the duration of the excitation pulse must be much shorter than the transit time of the carrier across the sample. This ensures that the carrier packet traveling through the sample has a very small width w which is much less than the sample thickness L. Also, the wavelength of the photoexcitation must be carefully chosen so that the absorption depth δ of the light is less the sample thickness L. The purpose of this is to make sure that only one type of carrier drifts across the sample. If the absorption depth δ is too small, carriers that are supposed to be drifted could be trapped by surface defects. The light intensity of the photoexcitation source must be adjusted to prevent the injected charge perturbing the internal field. If the light intensity is too high, the photoinjected charges will perturb the internal electric field in the sample, which will affect the drift of the photoinjected carriers across the sample. A condition known as the small signal condition is required to simplify the mathematical calculations involved in the analysis of TOF photocurrents. In principle, if the field remains constant (injected charge is negligible compared with the charge on the electrodes), then the photocarriers drift with the same velocity and cause a constant photocurrent, in the absence of any deep trapping. The photocurrent lasts until the carriers reach B.

As mentioned above, the small signal condition holds under the assumption that the internal field is uniform through the entire sample and the charge packet moves at a uniform velocity. If the duration of the excitation pulse is shorter than the carrier transit time, the injected holes form a packet of positive charge of width $w \ll L$ which drifts towards the

bottom electrode with drift velocity v_d. As show in Figure 2.12, a charge sheet at a position x' in the solid, in the absence of any pre-existing space charge, has electric fields F_1 and F_2 behind and in front of the charge sheet are constant and are functions of the position of the charge sheet in the solid [43]. The electric fields are expressed as

$$F_1 = F_0 + \frac{ep_o w}{\varepsilon}\left(\frac{x'}{L} - 1\right) \tag{2.16}$$

and

$$F_2 = F_0 + \frac{ep_o w}{\varepsilon}\frac{x'}{L} \tag{2.17}$$

where p_0 is the concentration of holes in the charge sheet, ε is the dielectric permittivity of the solid i.e. $\varepsilon_o\varepsilon_r$ where ε_o is the absolute permittivity and ε_r is relative permittivity. Equations 2.16 and 2.17 show that the charge sheet slightly alters the applied electric field $F_0 = V_0 / L$; the electric field F_1 behind the charge sheet is reduced and the electric field F_2 in the front of the charge sheet is increased. From the Maxwell equations, the rate of change of the electric field at the electrode gives rise to the external current that is measured.

The following expression must be fulfilled to reduce the effect of field enhancement than the unperturbed field F_0

$$\frac{ep_0 w}{\varepsilon} \ll \frac{V_0}{L} \tag{2.18}$$

Equation 2.18 represents small signal condition and implies that the charge on the capacitor plates to be much larger than the injected charge. The charge on the capacitor plate is given by $C_s V_0$ where C_s is the sample capacitor and V_0 is the applied voltage on the sample.

The production of the photocurrent in the external circuit by the drifting of the charge sheet through the sample can be explained by Ramo's theorem [44]. A carrier with charge q is generated within the sample and travels under the influence of applied electric field F_o, drifts

at a constant velocity $v_{\mathrm{d}} = \mu F_0$, where μ is the mobility of the carrier in the material. The knowledge of the drift velocity helps to define the transit time as the time taken by the generated carrier to drift across the sample from the point of production to the point of collection at the electrode. Transit time for carriers generated at A and collected at B is

$$t_{\mathrm{T}} = \frac{L}{v_{\mathrm{d}}} \tag{2.19}$$

but $v_{\mathrm{d}} = \mu F_o$, therefore

$$t_{\mathrm{T}} = \frac{L}{\mu F_{\mathrm{o}}} = \frac{L^2}{\mu V_0} \tag{2.20}$$

The work done by moving a charge q a distance dx is given by $dW = qF_0 dx$. In the external circuit, the work done by the battery moving the charge in a time dt is $dW = V_0 i_{\mathrm{ph}}(\mathrm{t})dt = qF_0 dx$. It can be shown that the external photocurrent is

$$i_{\mathrm{ph}}(t) = \begin{cases} \frac{qv_{\mathrm{d}}(t)}{L}, & 0 < t < t_{\mathrm{T}} \\ 0, & t \geq t_{\mathrm{T}} \end{cases} \tag{2.21}$$

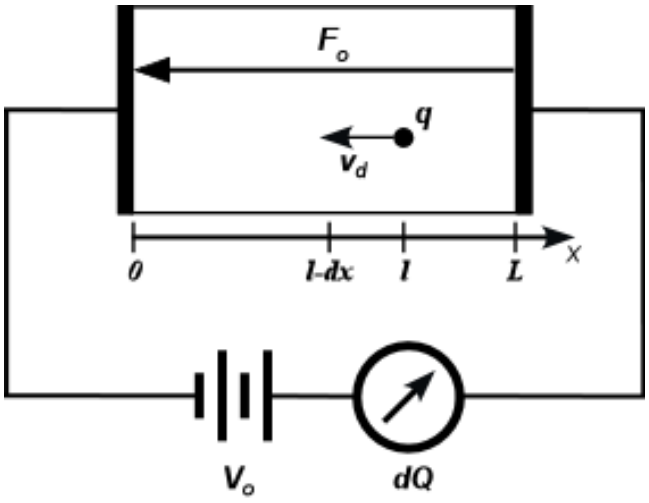

Figure 2.13 The motion of a charge q, through a distance dx makes a charge dQ flow in the external circuit. (After [7])

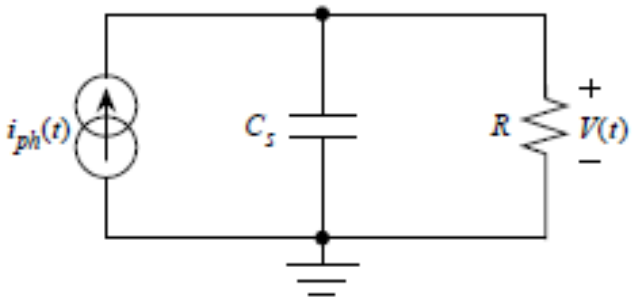

Figure 2.14 A simplified small signal AC equivalent circuit for the TOF experiment. C_s is the combination of the sample capacitance and any stray capacitances added by the cables.

Equation 2.21 is applicable to the TOF experiment as shown in figure 2.12 and given that the small signal condition is met, the total number of holes injected into the sample is given by

$$Q_0 = ep_0wA \tag{2.22}$$

The photocurrent in the external sampling resistor is therefore expressed a

$$i_{\text{ph}}(t) = \begin{cases} \frac{ep_0wAv_{\text{d}}}{\text{L}} = \frac{ep_0wA}{t_{\text{T}}}, & 0 < t < t_{\text{T}} \\ 0, & t \geq t_{\text{T}} \end{cases} \tag{2.23}$$

Figure 2.14 shows the AC equivalent circuit of figure 2.13. C_s is a combination of the sample capacitance and any stray capacitances present in the external circuitry. If $I_{ph}(s)$ and V(s) are the Laplace transform of the current and the voltage signals respectively, equation 2.24 gives the relationship between them.

$$V(s) = \frac{R}{sRC_{\text{s}}+1} I_{\text{ph}}(s) \tag{2.24}$$

Taking the inverse Laplace transform gives the expression which can be used to study the photocurrent and voltage. There are two possible solutions depending on *R* and C_s. The first

solution is when $RC_s \ll t_T$ which is known as the I-mode signal because the magnitude of the signal is proportional to the photocurrent [8]

$$v(t) \approx \begin{cases} Ri(t) & 0 < t < t_T \\ 0 & t \geq t_T \end{cases} \tag{2.25}$$

If $RC_s \gg t_T$ the resulting signal is known as the V-mode signal or charge transient signal as shown in equation 2.27 which is the integral of I-mode signal. The V-mode signal increases linearly as the charge sheet moves through the sample and can be used to measure total injection charge when $t \geq t_T$. The voltage signal remains constant with a magnitude that is proportional to the total injected charge after the carriers reached the collecting electrodes. From Equation (2.24) for $RC_s \gg t_T$, we have

$$V(s) = \frac{1}{sC_s} I_{ph}(s) \tag{2.26}$$

which corresponds to

$$v(t) = \frac{1}{C_s} \int_0^t i_{ph}(t')dt' \tag{2.27}$$

If there is no trapping, under small signals, the above gives

$$v(t) \approx \begin{cases} \frac{1}{C_s} \frac{ep_o wA}{t_T} & 0 < t < t_T \\ \frac{1}{C_s} ep_o wA & t \geq t_T \end{cases} \tag{2.28}$$

In amorphous selenium, there are many localized states in its mobility gap due to the disordered nature of the material. This implies that the time dependence of the number of mobile charge carriers has to be considered in the analysis of TOF signal. The presence of localized states reduces the number of free charge carriers (those in the transport band i.e. holes in the valence band) in the charge sheet because they become trapped in the localized states and do not contribute to conduction. This causes a decay in the magnitude of the photocurrent with time. A more accurate solution for amorphous semiconductors is achieved by taking the localized states into consideration. The first assumption is that a set

of traps at a discrete energy level in the band gap has a mean trapping time τ. This represents the lifetime of the carriers, and it is assumed that there is no release from trap, that is, the trap is "deep". When a carrier is trapped in a localized state, it takes longer time than the transit time to release the carrier from the trap. The solution of the continuity equation for this case shows that the presence of deep traps in the mobility gap causes the number of carriers in the charge sheet to decay exponentially as the carriers drift along the sample The solution of the Continuity Equation for this case results in an exponential decay term in Equation 2.23.

$$i_{\mathrm{ph}} = \frac{ep_0wA}{t_{\mathrm{T}}}\exp\left(-\frac{t}{\tau}\right) \tag{2.29}$$

The I-mode signal is then modified to

$$v(t) \approx \begin{cases} Ri(t)\exp\left(-\frac{t}{\tau}\right) & 0 < t < t_{\mathrm{T}} \\ 0 & t \geq t_{\mathrm{T}} \end{cases} \tag{2.30}$$

Integrating equation 2.29 gives the V-mode signal given as

$$v(t) \approx \begin{cases} \frac{ep_owA\tau}{C_{\mathrm{s}}t_{\mathrm{T}}}\left(1-\exp\left(-\frac{t}{\tau}\right)\right) & 0 < t < t_{\mathrm{T}} \\ \frac{ep_owA\tau}{C_{\mathrm{s}}t_{\mathrm{T}}}\left(1-\exp\left(-\frac{t_{\mathrm{T}}}{\tau}\right)\right) & t \geq t_{\mathrm{T}} \end{cases} \tag{2.31}$$

Figure 2.15 shows the comparison of I-mode and V-mode signals with trapping ($\tau = 100t_{\mathrm{T}}$) and without trapping ($\tau = t_{\mathrm{T}}$). Equation 2.30 is known as the Hecht relationship and can be used to calculate the deep trapping lifetime of charge carrier from a TOF photocurrent signal. Figure 2.16 below show a typical ideal waveform of TOF measurement

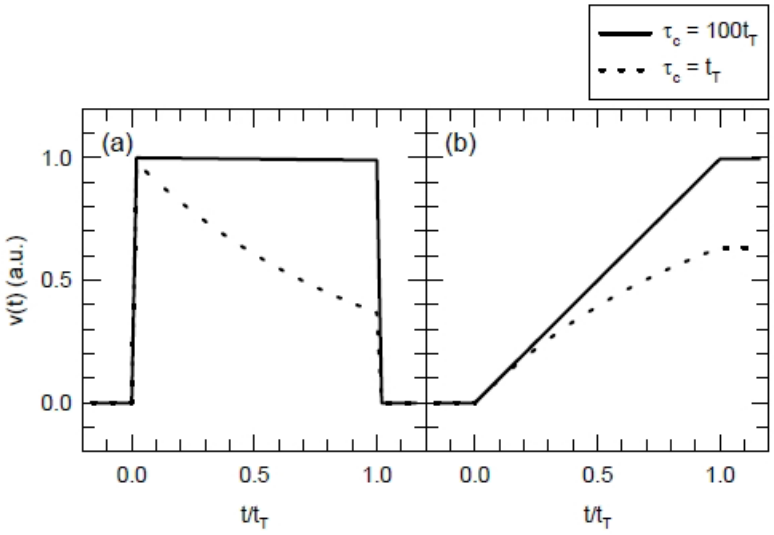

Figure 2.15 Simulated TOF (a) I-mode and (b) V-mode photocurrent with no traps (solid) and deep trapping (dashed).

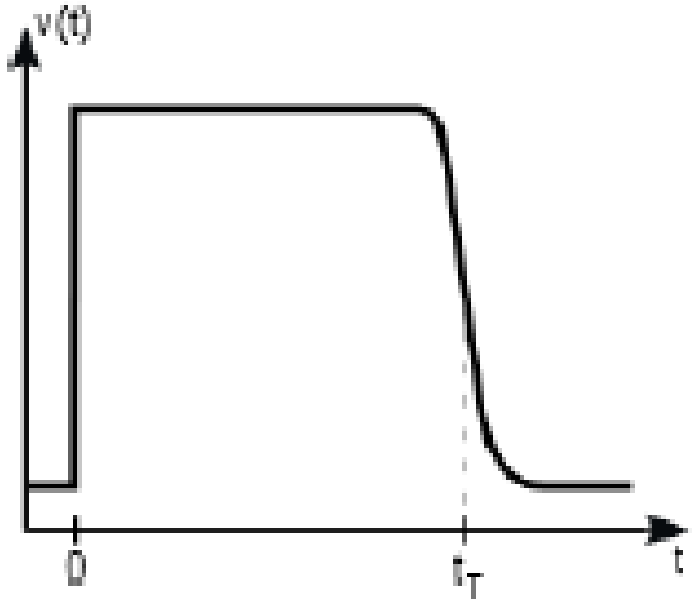

Figure 2.16 Figure 2.16: A typical ideal waveform of TOF measurement

2.3.3 The Interrupted-Field Time-of-Flight Technique

The interrupted field time of flight (IFTOF) method is based on the TOF technique presented in the previous section. It is used to estimate the carrier trapping lifetime in a high resistive material by interrupting the drift of carriers. IFTOF has a similar explanation as for the TOF technique. The only difference is that the applied field is switched off after a time t_1, causing the photocurrent to drop to zero, and switched back on after time t_2. Some of the carriers in the drifting carrier packet get trapped in the localized states in the mobility gap after the applied field is switched off. This causes a reduction in the magnitude of the photocurrent signal after the field is switched on for the remaining carriers to drift to the collecting electrode. The reduction in the magnitude of the photocurrent gives information on the carrier trapping lifetime.

At the point of interruption, the drift of carriers is stopped, and the carriers can interact with the deep traps in the mobility gap. Once the field is switched back, the carriers begin drifting again. The magnitude of the decrease of photocurrent during the interruption is proportional to the number of lost charge carriers because the charge carriers move at constant speed in the material. The interruption time $t_i = t_2 - t_1$.

If the traps in the mobility gap are characterized by a carrier trapping lifetime τ_c, then the carrier concentration after the interruption $p(t_2)$ can be related to the concentration of carriers before the interruption $p(t_1)$ by

$$\frac{p(t_2)}{p(t_1)} = \exp\left(-\frac{t_i}{\tau_c}\right) \tag{2.32}$$

Since the number carriers are proportional to the photocurrent, the current before and after the interruption is related by

$$\frac{i(t_2)}{i(t_1)} = \exp\left(-\frac{t_i}{\tau_c}\right) \tag{2.33}$$

From equation 2.32, the carrier trapping is then given as

$$\tau_c = \frac{t_i}{\ln\left(i(t_1)/i(t_2)\right)} \tag{2.34}$$

Carrier trapping time can be obtained from the IFTOF experiment in two ways. The first method is choosing an interrupted time and use Equation 2.33 to compute the trapping lifetime. The other method is to set different interruption time and perform multiple IFTOF measurements. A graph of $i(t_1)$/i(t_2) is then plotted against it on a semi-logarithmic scale and use the slope of the plot to compute the carrier trapping time. The latter method has an advantage of eliminating the time delay introduced by the electronic circuit in the experimental set-up. Figure 2.17 shows a typical ideal waveform of IFTOF.

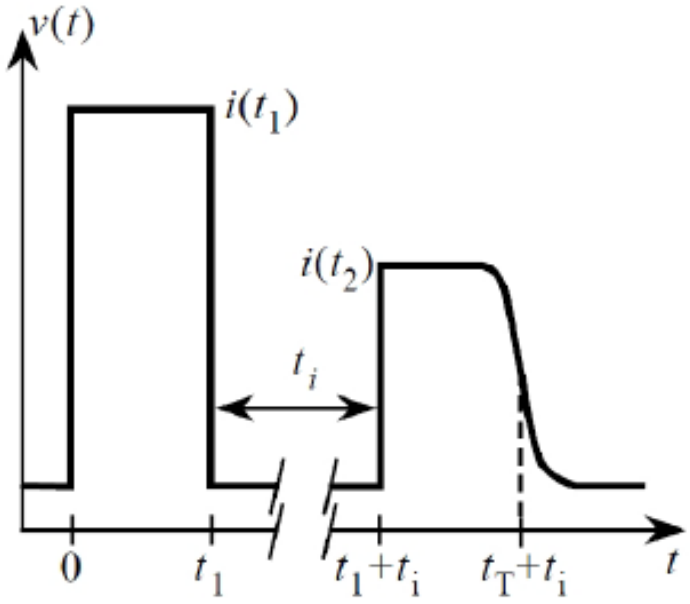

Figure 2.17 A typical ideal waveform of IFTOF measurement. The photocurrent is $i(t_1)$ and the photocurrent after the interruption is $i(t_2)$. Interruption time is t_i.

2.4 Transient Trap Limited Theories

Detailed theoretical explanations of the time of flight and the interrupted field time of flight techniques were presented in the previous section. Amorphous selenium, being the X-ray photodetector material considered in this study, has a complex internal structure. I-mode

and V-mode transient responses due to the drift of photoinjected carriers in the previous sections did not include the effects of the large concentration of localized states in the mobility gap. The localized states behave like trap centers for free carriers in the mobility gap and influence the carrier kinetics in the material significantly. So, to have a thorough understanding of the transport properties of amorphous solids, understanding the influence of the localized states on drifting charge carriers is very important. Three different distribution theories are presented in this section to explain the transient trap theory in an amorphous semiconductor.

2.4.1 Monoenergetic Trap Level

As mentioned in the previous sections, the localized states in the mobility gap serve as trap centers for mobile carriers. Monoenergetic trap model assumes a single energy localized state in the mobility gap. In this analysis, an infinitesimally small portion (slice) dx, of the

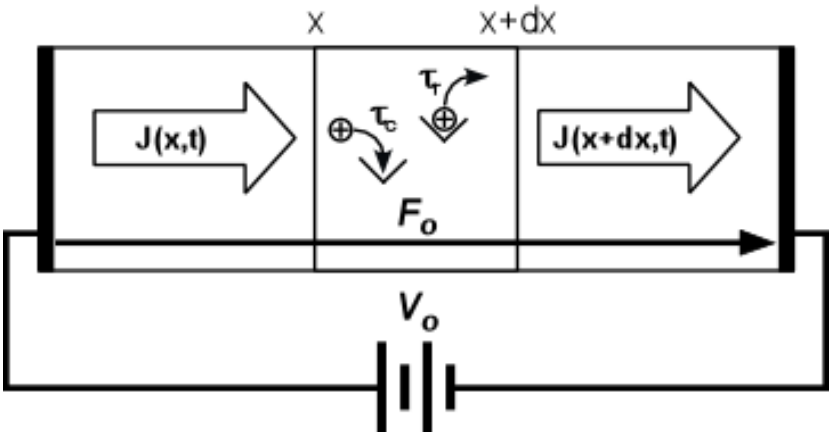

Figure 2.18 Carrier flow in a semiconductor involving trapping and releasing within a slice dx. (After Fogal [8])

semiconductor is considered as depicted in Figure 2.18. The rate of change of the number of free carriers in the slice is due to the net current flowing into the slice minus the net rate of increase in the trapped concentration.

The rate of change in the number of carriers in the slice is therefore[8]:

$$\frac{\partial p(x.t)}{\partial t} = \frac{1}{q}\frac{\partial J(x,t)}{\partial x} - \frac{\partial p_{\mathrm{t}}(x,t)}{\partial t} \tag{2.35}$$

where $p(x,t)$ is the concentration of the carrier of free carriers, $J(x.t)$ is the current density flowing due to holes, q is the elementary charge and $p_{\mathrm{t}}(x,t)$ is the concentration of trapped carrier in the slice. Equation 2.34 is also known as the Continuity Equation.

The net current density $\mathrm{J(x.t)}$, is made up of both conduction current induced as a result of drifting under the applied field, and diffusion current. The conduction current density is given as

$$J_{\mathrm{c}}(x,t) = qp(x,t)v(x,t) = qp(x,t)\mu E(x,t) \tag{2.36}$$

where μ is the carrier mobility.

The diffusion current as a result of the spatial variation in the concentration of charge carriers is given by

$$J_{\mathrm{D}}(x,t) = qD\frac{\partial p(x,\mathrm{t})}{\partial x} \tag{2.37}$$

where *D* is the diffusion coefficient. However, the total current density is derived from Equations 2.35 and 2.36 and is expressed as

$$\mathrm{J(x,t)} = J_{\mathrm{c}}(x,t) + J_{\mathrm{D}}(x,t) = \ qp(x,t)\mu E(x,t) + \ qD\frac{\partial p(x,\mathrm{t})}{\partial x} \tag{2.38}$$

The one-dimension continuity equation for the carrier transportation can be expressed as

$$\frac{\partial p(x.t)}{\partial t} = D\frac{\partial^2 p(x,t)}{\partial x^2} - \frac{\partial p_{\mathrm{t}}(x,t)}{\partial t} + \mu E(x,t)\frac{\partial p(x,t)}{\partial x} + \mu p(x,t)\frac{\partial E(x,t)}{\partial x} \tag{2.39}$$

In this expression, $p_{\mathrm{t}}(x,t)$ represents the trapped carrier density, $\frac{\partial p_{\mathrm{t}}(x,t)}{\partial t}$ is the change rate of trapped carriers which is determined by the carrier-trapping rate and carrier release rate [6].

$$\frac{\partial p_t(x,t)}{\partial t} = \frac{p(x,t)}{\tau_c} - \frac{p_t(x,t)}{\tau_r} \tag{2.40}$$

where τ_c is the trapping time (or captured time) and τ_r is the release time.

The simultaneous solution of the rate and continuity equations gives the expression for the carrier density in the charge packet as a function of *x* and *t*. In order to simplify the solution of the continuity equation, some assumptions were introduced. One of the assumptions is the small signal condition for the time of flight and interrupted field time of flight. Small signal condition assumes that the internal field is independent of time and position which means the applied electric field $E(x,t)$ is constant in the material. Also, it is assumed that the diffusion component of the current density is negligible compared to the drift component. The boundary conditions and initial states help to solve Equations 2.38 and 2.39 are extracted from the TOF experimental details from the previous section. There are no charge carriers at $t < 0$, at time $t = 0$, the photoexcitation pulse generates charge carriers at $x = 0$. Because the duration of the light pulse is very short, a delta function can be used to describe the carrier density at $t = 0$.

$$p(x,0) = P\delta(x,0) \tag{2.41}$$

where *P* is the total number of generated carriers. The number of trapped carriers at $t = 0$ should be zero because no carriers have traveled through the sample;

$$p_t(x,0) = 0 \qquad \text{for } x > 0 \tag{2.42}$$

The carriers are collected at the electrode after the carrier packet drifted across the sample and because traps cannot exist outside the sample. Then,

$$p(x,t) = p_t(x,t) = 0 \qquad \text{for } x > L \tag{2.43}$$

Using these boundary and initial conditions and Laplace transform method, the solution is given as [45][46]

$$p(x,t) = \frac{P}{\mu E}\exp\left(-\frac{z}{\tau_c}\right)\delta(t-z) + \frac{P}{\mu E}\exp\left(-\frac{z}{\tau_c}-\frac{t-z}{\tau_r}\right)\frac{\xi}{2}\frac{I(\xi)}{(t-z)}U(t-z) \qquad (2.44)$$

where E is the applied field, z is the time it takes for the carrier to reach distance x, $z = x/\mu E$, $I(\xi)$ is the first order hyperbolic Bessel function and $U(x)$ is a unit step function.

$$\xi = \frac{2\sqrt{\frac{\tau_c(t-z)}{\tau_r}}}{\tau_c} \qquad (2.45)$$

The first component of Equation (2.44) represents the charge carriers that have not undergone trapping and has a time-dependent exponential decay of the form exp (-t/τ_c) from the time of photo injection. The second term represents charge carriers that have gone through trapping and release process at least once. These carriers are released at a later time and have a minimum transit time of $t_T = L/\mu_o E$. Integrating Equation (2.44) over the sample length produces the time-dependent expression for the external current. It may be though that the complexity of the carrier density equation does not make it easy to apply this equation to studying the transient TOF response. However, two simplifying assumptions leads to two limiting cases; the low field case and high field case. These two cases correspond to short and long-time domains as explained below.

Under low field conditions, it is assumed that the transient time t_T of the carriers is much longer than the trapping time.

$$\tau_c \ll \frac{L}{\mu E} \approx \tau_c \qquad (2.46)$$

This implies that carriers are quickly trapped and those that are trapped to not experience release during the transient process, which means they do not contribute to transient current. Consequently, the second part of the carrier density equation is neglected. By applying the principle of conservation of charge, the relationship between the numbers of free carriers in the sample to the total injected charge is given by [47]

$$P = P_0\frac{\tau_c}{\tau_c+\tau_r} \qquad (2.47)$$

where P_0 is the total number of injected charge given by

$$P_0 = p_0 A w \tag{2.48}$$

where p_0 is carrier concentration, A is charge sheet area, and w is charge sheet width.

The photocurrent is obtained by substituting equation 2.47 into equation 2.23

$$i_{\mathrm{ph}} = \frac{eP_0\mu_0 E}{L}\frac{\tau_{\mathrm{c}}}{\tau_{\mathrm{c}}+\tau_{\mathrm{r}}} = \frac{eP_0\mu F}{L} \tag{2.49}$$

where

$$\mu = \frac{\tau_{\mathrm{c}}}{\tau_{\mathrm{c}}+\tau_{\mathrm{r}}}\mu_0 = \theta\mu_0 \tag{2.50}$$

where μ_0 is the carrier mobility in the corresponding trap-free solid. Due to trapping and release events, the effective carrier drift mobility is reduced. The transport mechanism under low field is known as shallow trap-controlled transport. The scalar numerical factor θ is known as the shallow trap-controlled transport factor [4].

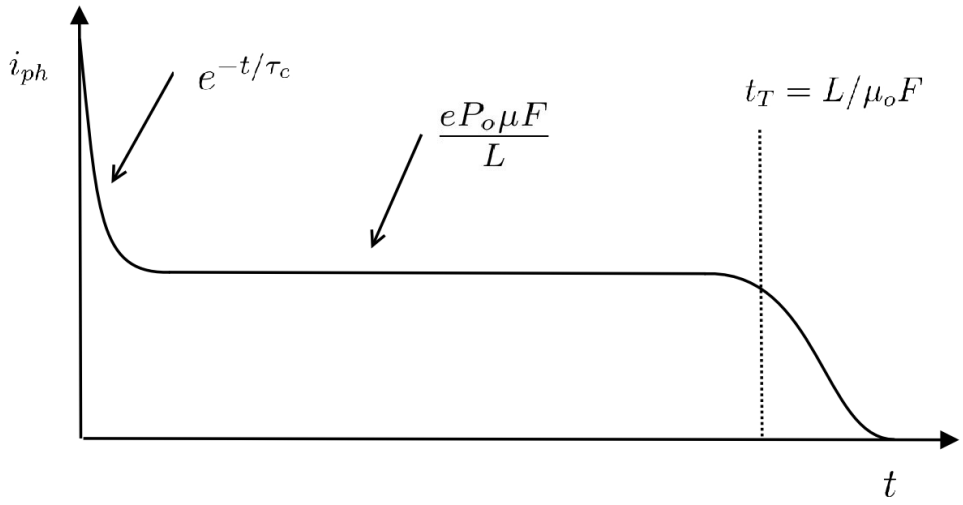

Figure 2.19 TOF waveform showing shallow trap-controlled drift ignoring deep tapping because of constant steady state current.

On the other hand, when a large field is applied to the sample, the transit time is much shorter than the trapping time, which implies that few carriers are captured in the trap centers during the drift process.

The TOF photocurrent is divided into two different time ranges; $0 < t < t_{\mathrm{T}}$ and $t > t_{\mathrm{T}}$ [47]. The transient response for; $0 < t < t_{\mathrm{T}}$ is given by

$$i_{\mathrm{ph}}(t) = \frac{eP_0}{t_{\mathrm{T}}}\left[\frac{\tau_{\mathrm{c}}}{\tau_{\mathrm{c}}+\tau_{\mathrm{r}}} + \frac{\tau_{\mathrm{r}}}{\tau_{\mathrm{c}}+\tau_{\mathrm{r}}}\exp\left(\frac{\tau_{\mathrm{c}}+\tau_{\mathrm{r}}}{\tau_{\mathrm{c}}\tau_{\mathrm{r}}}\mathrm{t}\right)\right] \qquad \text{for } 0 < t < t_{\mathrm{T}} \tag{2.51}$$

If trapping is neglected such that $\tau_{\mathrm{r}} \to \infty$, Equation (2.51) is changed to the case of deep trapping only as expressed by Equation 2.29.

Some part of the charge carriers gets trapped during the transient process and later released to take part in the photocurrent after transit time. For $t > t_{\mathrm{T}}$, the transient response is given as

$$i_{\mathrm{ph}}(t) = \frac{eP_0}{2}\frac{t_{\mathrm{T}}}{\tau_{\mathrm{c}}\tau_{\mathrm{r}}}\exp\left(-\frac{t}{\tau_{\mathrm{r}}}\right) \tag{2.52}$$

It is evident from the above equations that the transient photocurrent will decay initially decay exponentially until the carriers reach the collecting electrode where the magnitude reduces and then decays exponentially to zero as the trapped carriers are released and collected.

2.4.2 Multiple Trap Distribution

This section presents a more realistic model for describing many types of semiconductors, including some a-Se. The model includes both shallow traps and deep traps. In general, however, we can expect a distribution of localized states. As long as we can divide the localized states into two groups, one shallow and one deep, the following binary trap distribution can be used to model the observed TOF signal. Consider a binary trap distribution which involves two different traps with different trapping times and release time.

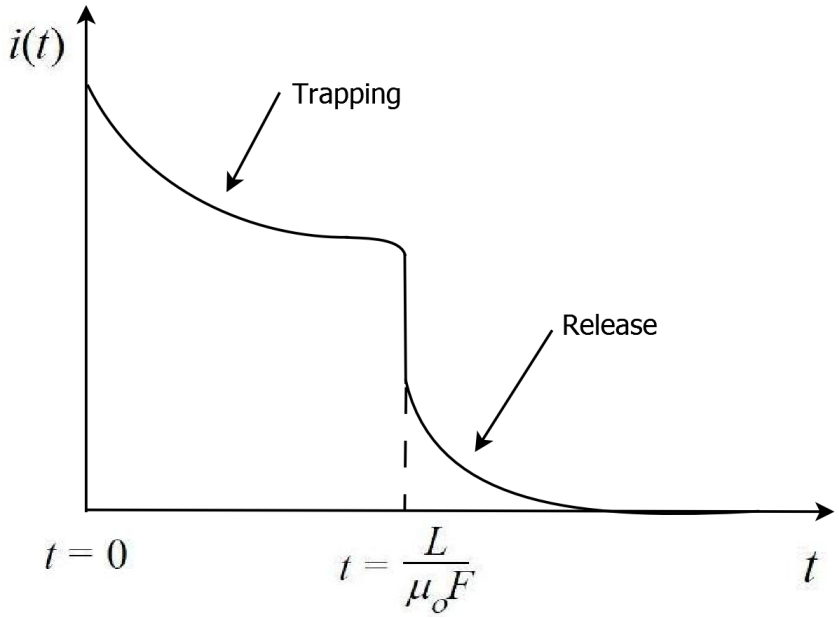

Figure 2.20 Photocurrent waveform in the model of the high field [7]

A major assumption in simplifying the analysis of this model is that the concentration of injected charge is much less than the concentration of traps at each energy state. This assumption suggests that there only a limited number of free carriers to fill all the traps and that only trapping free carriers contribute to the number of carriers trapped at a level. Two trapping times τ_{c1} and τ_{c2} and two release times τ_{r1} and τ_{r2} are considered in this model. Blakney and Grunwald give the transient current for a binary traps distribution [48].

$$j(t) = A\exp(-\alpha t) + B\exp(-\beta t) + j_{\infty} \tag{2.53}$$

where

$$\alpha + \beta = \frac{1+\theta_1}{\tau_{c1}} + \frac{1+\theta_2}{\tau_{c2}} \tag{2.54}$$

$$\alpha\beta = \frac{|\theta_1+\theta_2(1+\theta_1)|}{\tau_{c1}\tau_{c2}} \tag{2.55}$$

$$\alpha A + \beta B = \frac{j_0}{\tau_{c1}} + \frac{j_0}{\tau_{c2}} \tag{2.56}$$

$$A + B + j_\infty = j_0 \tag{2.57}$$

and

$$j_\infty = \frac{j_0\theta_1\theta_2}{|\theta_1+\theta_2(1+\theta_1)|} \tag{2.58}$$

where $\theta_1 = \tau_{c1}/\tau_{r1}$ and $\theta_2 = \tau_{c2}/\tau_{r2}$. The term j_∞ represents the steady state current that flows when the drifting free carriers are in equilibrium with the traps. When one of the two trap levels is deep in the mobility gap in a way that $\tau_{r2} \to \infty$, this makes $\theta_2 = 0$ and Equations (2.53) becomes

$$j(t) = A\exp\left(-\frac{t}{\tau_{c1}}\right) + B\exp\left(-\frac{\theta_1 t}{\tau_{c2}}\right) \tag{2.59}$$

Equation (2.59) shows the transport mechanism known as shallow-trap controlled with deep trapping. The first part depicts a sharp fall which decays exponentially until the carriers reach equilibrium with the shallow traps followed by a slower exponential decaying curve with a characteristic decay rate of τ_{c2}/θ_1

It is important to recognize the observed deep trapping time on the TOF signal (the exponential decays after the initial sharp fall) does not directly represent the trapping time τ_{c2}/θ_1 into deep traps. The observed trapping time τ_{c2}/θ_1 is prolonged by the factor θ_1. In other words, the existence of shallow traps (τ_{c1}andτ_{r1}) prolongs the observed deep trapping time by a factor 1/ θ_1.

Furthermore, if we take the product of observed drift mobility and the observed deep time, we find that

$$\mu\tau = \theta_1\mu_o\left(\frac{\tau_{c2}}{\theta_1}\right) = \mu_o\tau_{c2} = \mu_o\left(\frac{1}{v_{th}S_tN_t}\right) \tag{2.60}$$

where v_{th} is the thermal velocity of the free carriers (their mean speed), S_t is the capture cross section and N_t is the concentration of deep traps. Notice the $\mu\tau$ product does not

depend on θ_1. The most important parameter that controls the $\mu\tau$ product is the deep trap concentration N_t

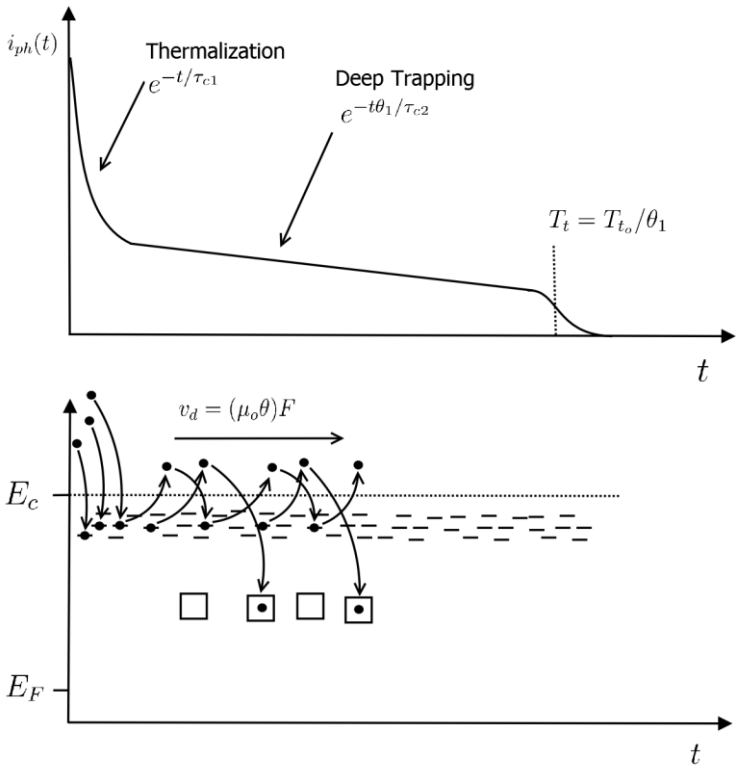

Figure 2.21 Photocurrent and energy band diagram representation of the TOF experiment with a binary trap distribution. The process of thermalization and deep trapping are shown with exponential decay expression. The charge carrier packet drifts with a velocity v_d. Shallow traps are located just below the conduction band energy E_c while deep traps are located in lower energy states just above the fermi level E_F.

2.5 Summary

The absence of long-range periodicity makes conventional solid state mathematical tools difficult to apply to this class of solids. Experimental results of the electronic and optical properties of amorphous solids show we can carry some concepts such as the density of states over to the non-crystalline domain. The electronic and optical properties of amorphous selenium follow the models for other amorphous solids. The density of states (DOS) model can be used to explain the electronic and optical properties of a-Se. The structural models for a-Se show that random variations in the dihedral angle is the most important feature and results in a structure that has chains with ring fragments. The structure of a-Se also has thermodynamically stable valence alternation pair (VAP) type defects, which have localized energy levels in the mobility gap. These defects are charged over and under-coordinated Se atoms, that is, Se_3^+ and Se_1^-. The density of localized states and their energy positions in the mobility gap affect the optical and electronic properties of amorphous semiconductors.

The density of states DOS models were reviewed in this chapter. These models help to understand carrier transport in amorphous solids as well as their optical properties. The DOS models essentially provide information about the distribution of defects in the mobility gap.

Since one of the main focuses of the research is to investigate the effect of X-ray irradiation on the electronic properties of a-Se, X-ray generation, and absorption is also presented in this Chapter. The theoretical analysis of the X-ray energy absorbed in a-Se is introduced, which is eventually used to calculate the x–ray dose deposited in the samples in the course of this research work.

Also presented in this chapter is the theory behind the measurement techniques employed in this research work. The measurement techniques are the time of flight and the interrupted field time of flight. The time of flight enables the measurement of the drift mobility of charge carriers in a-Se. The interrupted field time of flight technique enables the measurement of the carrier trapping lifetime of a-Se. The knowledge of both the carrier drift

mobility and trapping lifetime is essential to understanding the performance of a-Se x-ray detectors.

The expressions for the transient response for different trap distributions in amorphous semiconductors are developed in this chapter. In one simple approach, one assumes that there are shallow trap centers and deep trap centers located in the mobility gap of a semiconductor. Free moving carriers are trapped for a short time in the shallow trap centers and then released which therefore reduce the carrier mobility by a factor θ, called the shallow trap mobility reduction factor; this θ depends on the ratio of the capture and release times associated with the shallow traps An exponential decay of the photocurrent with a decay rate proportional to apparent trapping time τ'_{d} is caused by the deep traps. This apparent lifetime is given by $\tau'_{\mathrm{d}}/\theta$ where τ'_{d} is the deep time in the absence of shallow traps. The TOF and IFTOF techniques introduced in this chapter can be employed in the study of the distribution of gap states in amorphous semiconductors.

3. EXPERIMENTAL PROCEDURE

3.1 Introduction

This chapter presents the experimental procedure employed in the study of the electronic transport properties of alloys of amorphous selenium. The procedure for the preparation of samples used in this research is also described in this chapter. Section 3.3 describes the X-ray system used to produce X-rays, the X-ray dose measurement system and dose rate adjustment. In Section 3.4, a detailed description of charge transport measurement is presented which includes both the charge mobility measurement by the time of flight technique and the charge trapping lifetime by the interrupted field time of flight method. A detailed depiction of the TOF/IFTOF measurement system built for this study is presented in Section 3.5 followed by the accumulated dose measurement, lifetime recovery and the temperature control system.

3.2 Sample Preparation

Pure amorphous selenium is not thermally stable and crystallizes over few weeks or months after its formation. It can be easily stabilized by alloying it with a trivalent element such as arsenic. In addition, it is doped with a few parts per million of halogen, chlorine being the most commonly used halogen. Typically, the arsenic alloying level in stabilized a-Se ranges from 0 to 1% and chlorine doping level varies from 5 to 10 ppm. Stabilized a-Se films were used as samples for this research work. The thickness of samples ranged from 50 μm to 200 μm. Amorphous selenium samples were prepared by conventional vacuum deposition methods. Vitreous selenium pallets were heated in a stainless-steel boat to evaporate and then allowed to condense on a glass substrate coated with a layer of aluminum. The aluminum layer on the substrate serves as the bottom electrode for the experiment. In some cases, a thin layer of indium tin oxide (ITO) is used as the bottom electrode although most of the samples used in this study use aluminum layer.

The aluminum coated substrates were placed in the NRC 3117 stainless steel vacuum coater system as shown in Figure 3.1. The process of vacuum deposition started with adding the source material, which is selenium pallets, into a molybdenum boat and heated to approximately 250^{o}C by a large 100 - 150A ac current until it begins to evaporate. The vacuum chamber was evacuated to a base pressure of $\sim 10^{-6}$ Torr. Selenium vapors are allowed to condense on the substrate held just above the glass transition temperature of the particular a-Se alloy. [49]

Figure 3.1 NRC 3117 Stainless steel vacuum coater system.

The schematic diagram of the NRC 3117 is shown in Figure 3.1. During the process of deposition, two separate thermocouples were connected to control and monitor the temperature of the molybdenum both and the substrate. A digital quartz crystal rate monitor was used to monitor the evaporation rate of selenium. Once the desired thickness was reached, the shutter was closed, and the current is kept on until the evaporation rate of

selenium is very low. The samples are kept in a dark chamber for 24 – 48 hours to allow the samples' physical properties to stabilize.

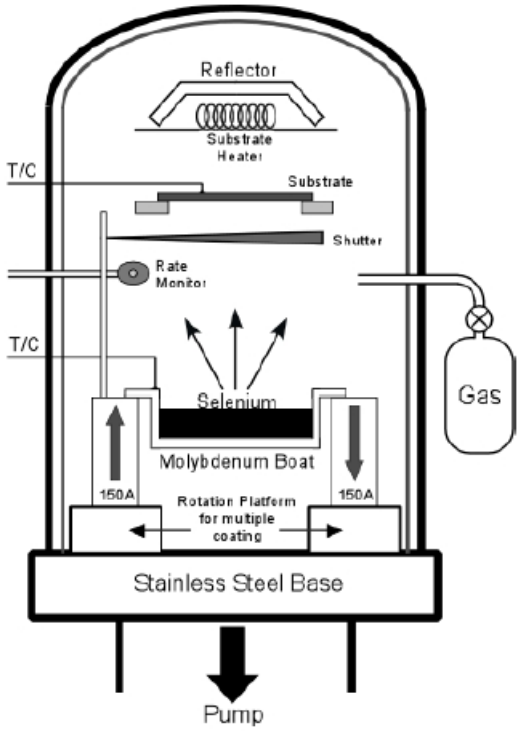

Figure 3.2 Schematic diagram of the NRC 3117 vacuum deposition system used in making the samples. (After [8])

A semitransparent circular gold contacts of area 0.2 cm^2 were sputtered on the sample to act as a top electrode for connection in the TOF/IFTOF experiment. A Hummer VI sputtering system is used to make the top contact on the samples. Figure 3.3 show the picture of the Hummer VI system used to sputter contact on the samples and Figure 3.4 shows the schematic diagram of the Hummer VI sputtering system describing how contacts are made on the a-se sample. A gold mask with a circular opening of 0.5 cm was used to cover the sample while the chamber of the system was filled with argon and kept at a pressure of 100 mTorr. A high voltage was applied to ionize the argon gas molecules. The positively charged ions as a result of ionization of argon gas moecules collide with the negatively

charge gold target, and cause gold atoms to be removed from the target; hence the name sputtering. The gold atoms then impinge and cover the exposed part of the sample uniformly.

Figure 3.3 Hummer VI sputtering system

The sputtered gold films were very thin, of the order of a few hundred angstroms to allow light to pass through into the sample. The semitransparent thickness was obtained by trial and error. The exact thickness is not critical as long as light can pass through the contact to photogenerate carriers in a-Se

During the TOF/IFTOF experiment measurement, electrical connections are established with the substrate electrode and the gold top electrode, using stainless steel connectors and a small portion of indium to protect the sample.

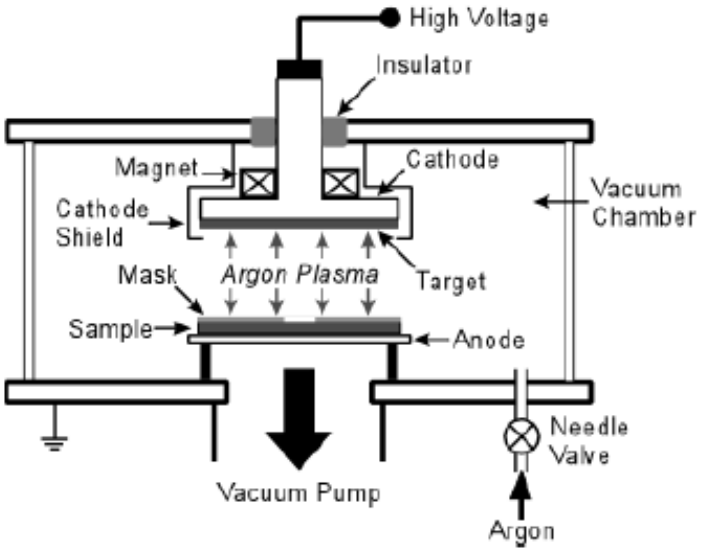

Figure 3.4 Schematic diagram of the Hummer VI sputtering system for making contact on the a-Se samples. (After [8])

3.3 X-ray Dose Measurement

3.3.1 X-ray Tube System

In the TOF/IFTOF experiment set-up, Gendex GX 1000 X-ray tube system is employed as the X-ray source. It has an adjustable peak voltage from 50 kVp to 100 kVp with two selectable filament currents of 10 mA and 15 mA. It has an aluminum window thickness of 2.5mm and uses tungsten as the anode material which produces a wide range of spectrum. The X-ray beam pulses at 1/60 of a second because of the half-wave rectifier

used by the system with a power supply frequency of 60 Hz. The X-ray system can generate a succession of x-ray pulses for a duration from 1/12th to 5s with the help of a time selection dial on the equipment.

The system has a limited irradiation time because the X-ray tube overheats if operated longer than a specific time. Table 3.1 shows the working cycle of the tube within 5 minutes. Figure 3.5 shows the outward appearance of the Gendex GX-1000 X-ray system with the

stainless-steel protection chamber. The stainless-steel chamber protects users from X-ray irradiation.

Figure 3.5 Gendex GX 1000 X-ray system and lead chamber protection

Table 3.1 Working Cycle of the X-ray tube [50]

	Exposure-Second in 5 minutes	
kVp	**10 mA**	**15 mA**
50-70	30	20
80	26	17.5
90	23	15.5
100	21	-

3.3.2 X-ray Dose Measurement System

In this research work, the amount of X-ray dose deposited into samples was determined by first measuring the dose in air and then through calculation. The process of dose determination has two parts. The first part is the use of a dosimeter system to measure the X-ray exposure to the samples. The second part is the theoretical calculation of the deposited X-ray dose. Keithley 35050 Ion Chamber with the Keithley 35050 Dosimeter were used to measure the X-ray exposure in Roentgen. The ion chamber is 1.25 cm thick and the total volume is 15 cm^3. A multimeter was connected to the dosimeter to record the voltage read out during X-ray exposure and the readout from the multimeter is converted to dose in Roentgen by using a converting factor from the calibration of the Keythley Dosimeter system in Equation 3.1

$$\mathrm{V(volt)} \times 0.734 \left(\frac{\mathrm{Volts}}{\mathrm{Roentgen}}\right) = \mathrm{Dose(Roentgen)} \qquad (3.1)$$

Once the dose deposited into the ion chamber is estimated with the thickness of each sample, the dose deposited in each sample is calculated.

3.3.3 X-ray Dose Rate Adjustment

X-ray dose rate can be adjusted either by controlling the X-ray energy output from the X-ray tube or the absorbed dose rate for the sample. The x-ray intensity from the X-ray tube can be adjusted by changing the filament current of the X-ray tube; however, there are only two choices (10 and 15 mA). The output dose rate is proportional to the filament current and since the X-ray system has two filament current options, the output dose rate can be adjusted by switching between the filaments current. The dose rate at 15 mA is 1.5 times more than the dose rate at 10 mA. However, changing the distance between the X-ray source and the sample is a way of adjusting the absorbed dose rate in the sample. The reason being that X-ray energy fluence (energy per unit area) decreases with respect to distance, so changing sample position varies the absorbed X-ray dose in the sample.

Figure 3.6 Keithley 35050 Dosimeter and Ion Chamber for X-ray exposure measurement

3.4 Charge Transport Measurements

The conventional Time-of-Flight (TOF) and Interrupted–Field-Tome-of-Flight (IFTOF) techniques were the major tools used to study the charge transport properties of the a-Se in this work. As discussed in the previous chapter, these experiments capture the transient

response of the drift of charge carriers through a semiconductor under the application of a high electric field. Figure 3.7 shows a simplified schematic of the set-up of the TOF/IFTOF experiment. A switchable high voltage power supply is triggered by the signal HVON to apply a high voltage bias V_A to the sample followed by photoexcitation by a short light pulse which is strongly absorbed by the sample. This creates electron-hole pairs under the semi-transparent gold top electrode near the surface of the sample.

Once electron-hole pairs are generated, the applied voltage separates the electron and the holes depending on the polarity of the applied voltage. If the top electrode is connected to the positive terminal of the applied voltage, the electrons are collected immediately photogeneration and the holes drift across the sample. The drift generates a current *i*(t) in the external circuit which is measured as a voltage through a sampling resistor *R*. The voltage is amplified and recorded by an oscilloscope which is triggered by and synchronized with the laser trigger to capture the entire transient response.

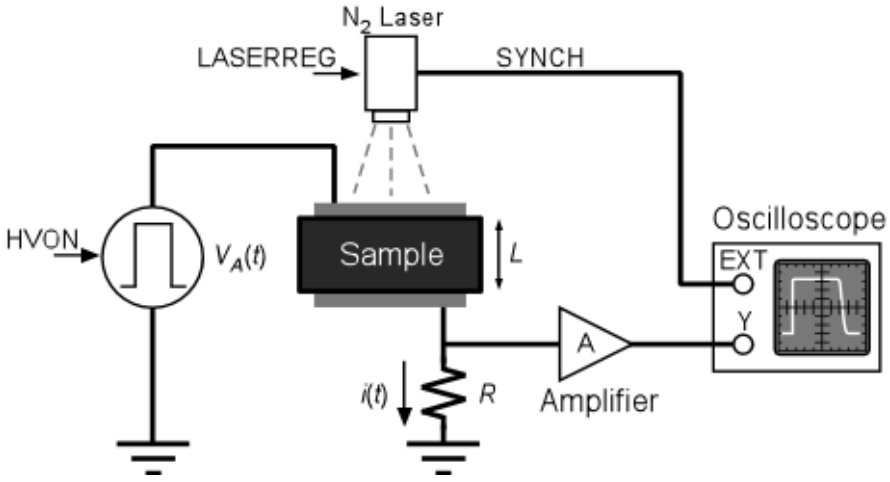

Figure 3.7 A simplified schematic diagram of TOF and IFTOF measurement system

The value of the sampling resistor affects the magnitude of the captured signal. The magnitude of the captured signal can be maximized by increasing *R* which is at the expense of an increase in the *RC* time constant of the circuit. *C* is the combined capacitance of the sample and stray capacitances from the cables and the attached electronics to *R*. So, the value *R* is selected such that $RC \ll t_T$ where t_T is the transit time of the TOF pulse. As long

as $RC \ll t_T$, I-mode of operation will be maintained, and the signal will represent the transient photocurrent

The drift mobility of both carriers, electrons, and holes, is determined by the time-of-flight technique in high resistive semiconductors. This measurement technique was first introduced by Spear [30], Kepler [51], Leblanc [52], and Brown [53] with several modifications evolved over the years such as different photoexcitation sources, different high voltage bias schemes and advanced photoexcitation techniques [54]. Because the spectral output of the photoexcitation source must be closely matched to the bandgap of the material under investigation, a careful selection of the photoexcitation source is very important to the experimental set-up. Some excitation sources that have been used previously include xenon flash lamp and Kerr cell, nitrogen-pumped a dye laser, and condenser powered air spark gap, nitrogen flash lamp and Q-switched ruby laser [47][55][56][57][58][59]

Figure 3.8 (a) shows a typical timing sequence and resulting I-mode photocurrent (converted to voltage by *R*) transient waveform for a TOF experiment under positive applied voltage, that is, for transiting holes. Electron measurement is captured by reversing the polarity of the bias voltage. At time $t = 0$, a pulse of light is injected into the sample by the laser and electron-hole pairs are generated near the surface of the sample. The top electrode immediately collects the electrons near the surface of the sample and holes drift across the sample by the applied field. The drift of photoinjected holes induces a transient photocurrent in the external circuit. The transit time, which is the time taken by the charge sheet to move from the point of generation to the point of collection by the bottom electrode, corresponds to the half magnitude point on the photocurrent tail of the transient pulse is used to determine hole mobility μ_h. The average drift velocity is given by

$$v_{dh} = \frac{L}{t_T} \tag{3.2}$$

Electric field (F = V/L) is assumed to be uniform, it implies that drift velocity will be constant and related to the electric field by $v_{dh} = \mu_h F$, where μ_h is the hole mobility. Therefore

$$\mu_h = \frac{L^2}{V t_T} \tag{3.3}$$

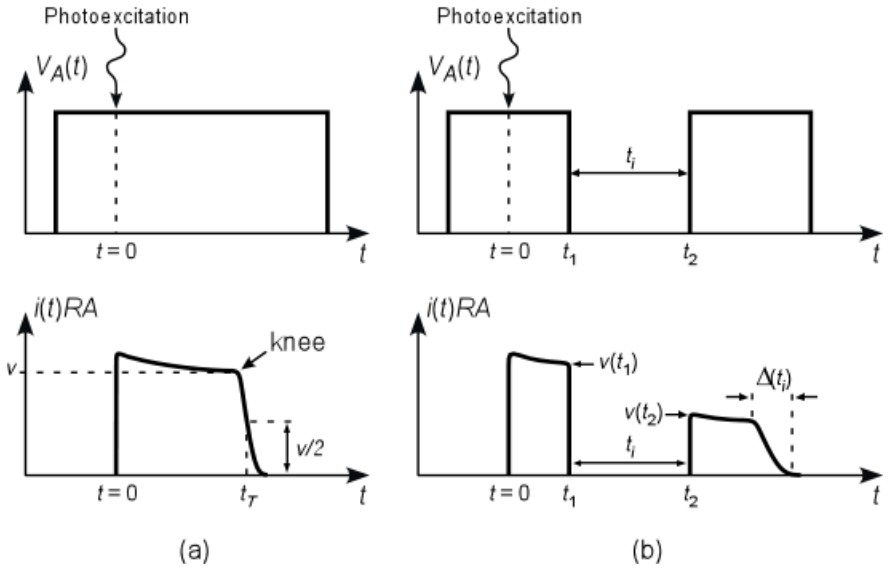

Figure 3.8 A typical timing transient voltage response for the (a) TOF and (b) IFTOF signal. The TOF signal shows hole transit time t_T which is used to determine hole mobility. For the IFTOF signal, the bias voltage is interrupted to determine hole trapping time or lifetime. (After Fogal [8])

The IFTOF experimental timing and resulting waveforms for hole drift measurements are shown in Figure 3.8 (b). The process involved in IFTOF is similar to the TOF experiment. At time t = 0, electron-hole pairs are photogenerated near the surface of the sample by the injection of a short pulse light. Electrons are immediately collected by the top electrode while holes drift across the sample. At time $t = t_1$, the bias voltage is switched off which stops the drifting of holes and the transient photocurrent drops to zero. The bias voltage is switched on at time $t = t_2$ which causes the drift of holes to resume. During the interruption time $t_i = t_2 - t_1$, some of the charge carriers, holes in this, case, interact with localized

state located in the mobility gap of the material. Those holes that are captured by deep traps (those from which there is no release during the experiment) are removed from the charge sheet during the experiment. The loss in charge carries during the interruption time is reflected in the drop in the magnitude of the photocurrent after the interruption time. If the average trapping time is defined by τ_h, the fractional recovered photocurrent signal relates with the interruption time t_i by

$$\frac{i(t_2)}{i(t_1)} = \exp\left(-\frac{t_i}{\tau_h}\right) \tag{3.4}$$

where $i(t_1)$ and $i(t_2)$ are the photocurrent magnitude before and after interruption respectively. Rearranging Equation 3.4 gives the hole trapping time and expressed as

$$\tau_h = \frac{t_i}{-\ln(i(t_2)/i(t_1))} \tag{3.5}$$

Repeating the IFTOF experiment at the same interrupted position point t_1 to measure $i(t_2)/i(t_1)$ at different interruption time t_i can be used to estimate the carrier lifetime by plotting $i(t_2)/i(t_1)$against t_i on a semi-logarithm scale. The slope of the plot gives the carrier trapping time. An example is shown in Figure 3.9

The experimental implementation of the IFTOF method is quite difficult because of large transients produced by switching of high voltages on and off. Quite a number of techniques have been used in the past to eliminate this displacement current. Complementary pulse bias technique was used by Kasap [60]. Plischuk and Kasap later used a floating Schering bridge network to use a single high voltage supply [61]. This technique generates stray capacitances that made balancing the bridge difficult.

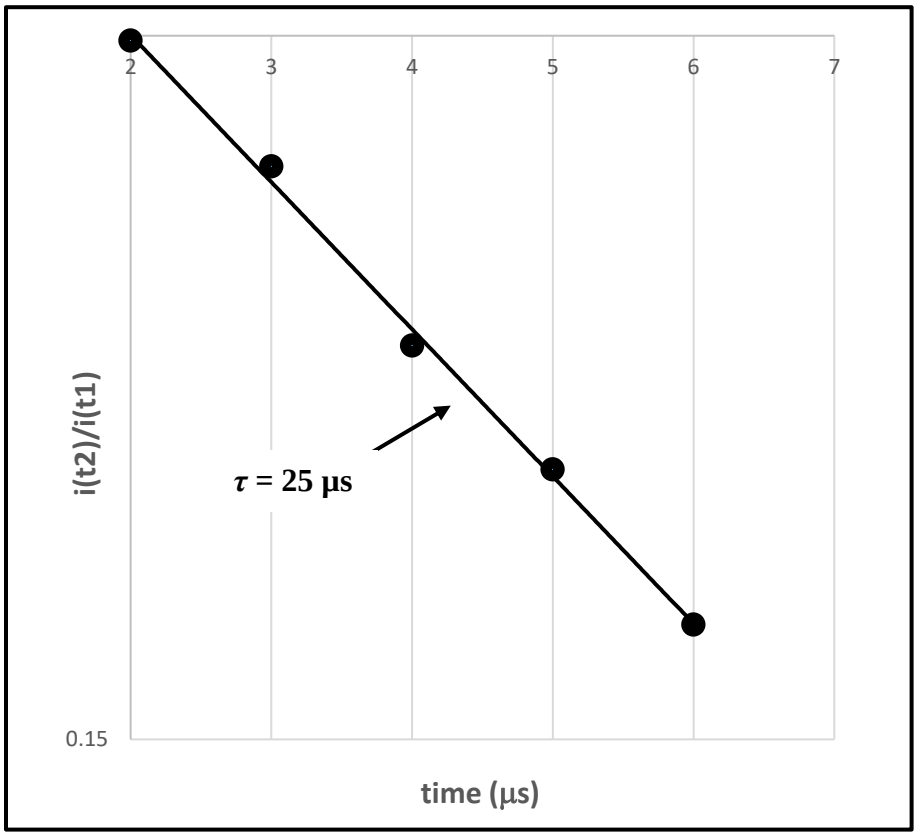

Figure 3.9 A semi-logarithm plot of the ratio of photocurrent drop and interruption time. The slope of the plot gives the carrier trapping time.

A grounded bridge network was used to eliminate the displacement current in this research work. This technique provides a grounded voltage supply to bias the sample for good radio-frequency interference (RFI) shielding and uses a variable capacitor to balance the displacement currents in the two branches of the bridge. Figure 3.10 shows the concept of the bridge circuit. A differential measurement is performed across the bridge while a differential amplifier detects the photocurrent signal because it appears in only one branch of the bridge.

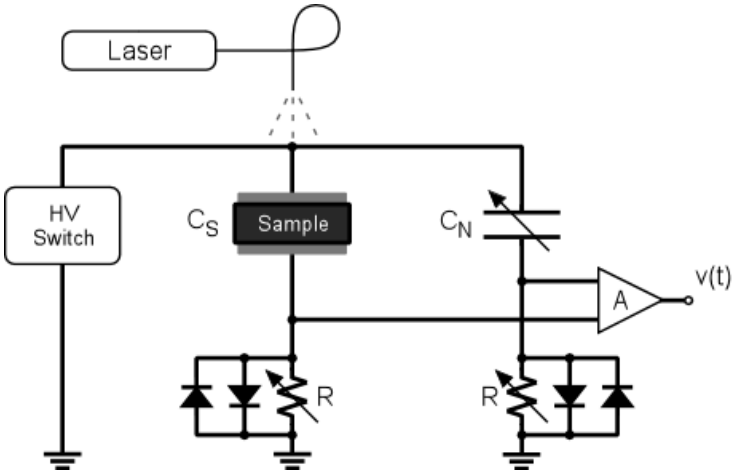

Figure 3.10 a grounded bridge network to eliminate the displacement current signal from IFTOF transient measurement

3.5 TOF/IFTOF Experimental System

3.5.1 System Overview

The TOF/IFTOF experiment setup implemented for this study includes an LN103C nitrogen-pumped dye laser, an amplifier system, a high voltage supply and switching system, a grounded bridge system and a commanding and data acquisition system. The LN103C nitrogen-pumped dye laser system is used for photoexcitation of the sample to inject charge carriers in the sample. The transient response signal of the TOF/IFTOF measurement can be very small, so the amplifier is used to boost the signal. The high voltage supply provides the voltage bias for the sample under investigation while a fast switching HV HEXFET switching system is used to turn on and off the voltage supply during the IFTOF experiments. A grounded bridge network eliminates the displacement current produced as a result of switching on and off the high voltage. A variable capacitor C_N with a large breakdown voltage was used to balance the bridge with two ultra-fast switching rectifiers across each bridge resistor to limit the large common mode switching transient. Note that in a perfectly balanced bridge, the common mode signal due to transients would be nil but the bridge can never be perfectly balanced. Further, initially right after the introduction of the sample, the bridge is unbalanced. The trigger signals for the switches,

laser and the oscilloscope were generated by a PCI- CTR05 counter board in the PCI of a personal computer.

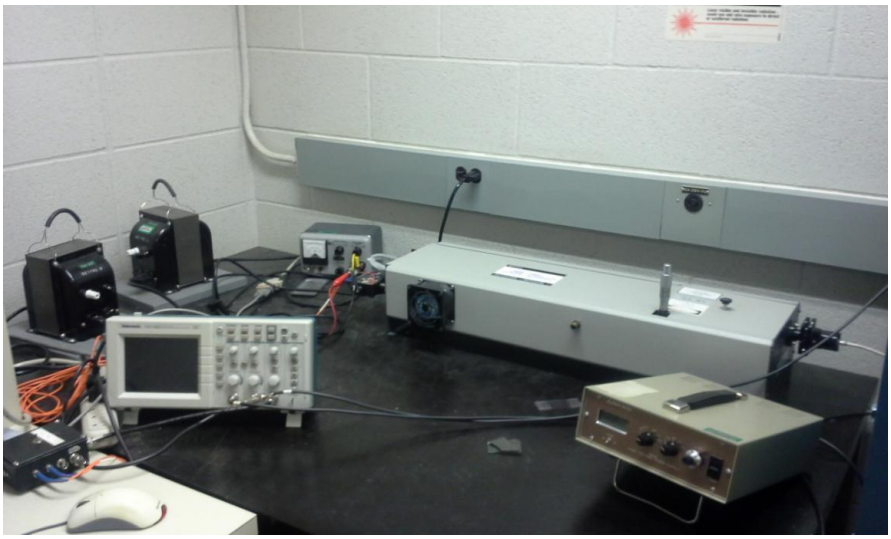

Figure 3.11 Some component of the experimental setup for the TOF/IFTOF experiment showing A LN103C nitrogen-pumped laser, a 10V supplied triggering system, an EG&G high voltage supply, a Tektronix digital oscilloscope and a GBIB

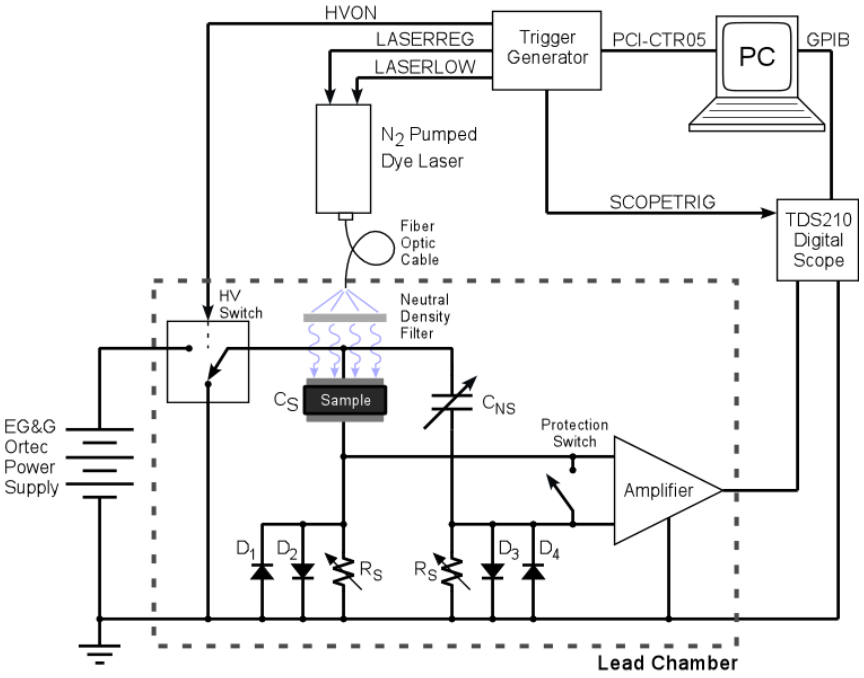

Figure 3.12 The TOF/IFTOF system schematic

3.5.2 High Voltage Switch and Supply

A large bias voltage is applied to the sample to investigate the bulk transport properties; both the charge carrier mobility and trapping lifetime. The large bias voltage is required because of the relatively large thickness of samples to represent typical x-ray photoconductor thicknesses in practical detectors. So, an EG&G Ortec 556 high voltage supply is used to apply voltage bias on the sample and a switching system is employed to turn on and off the voltage supply. The high voltage switch uses a fast switching n-channel HEXFETS in a totem pole configuration [10]. The maximum switching voltage of the HEXFET is 1 KV and when it is in conduction mode, it passes current from the high voltage input to the high voltage output as shown in figure 3.12 in the circuit design.

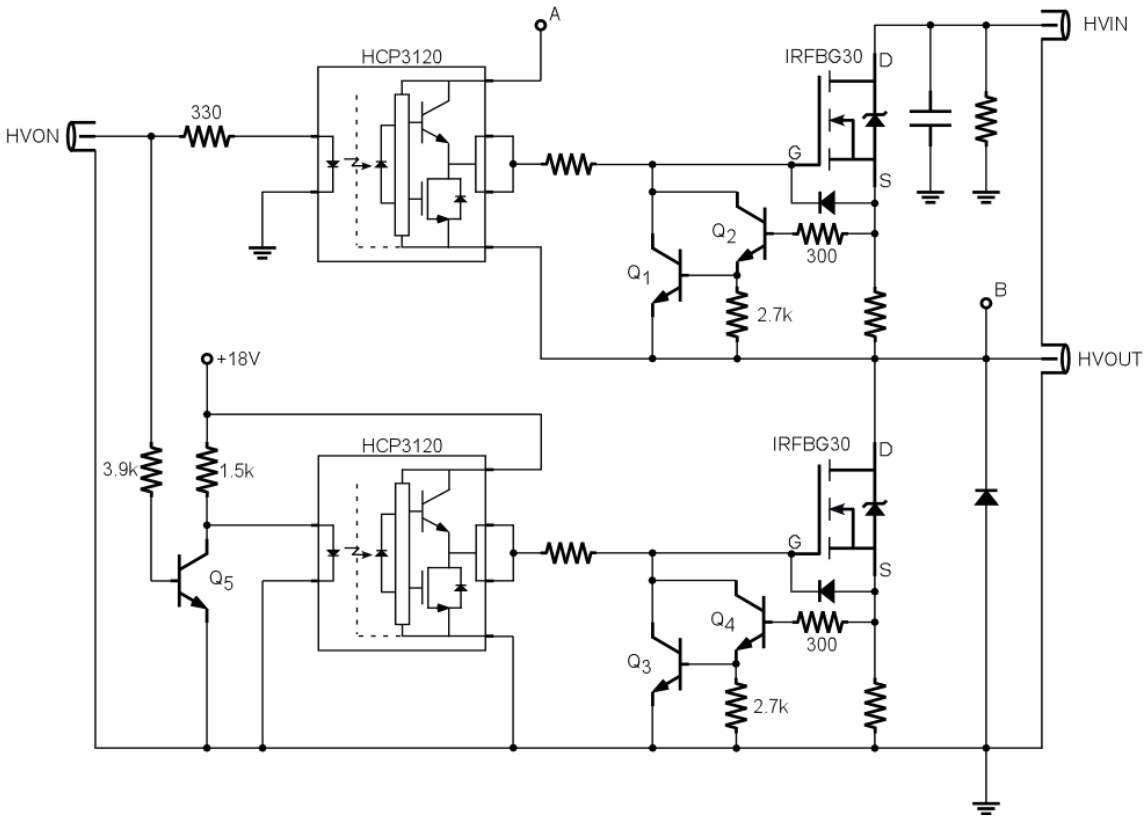

Figure 3.13 A 1 KV fast switching high voltage HEXFET switch.(After [8])

The type of HEXFET switch used was a fast switching n-channel IRFBG30 with a maximum gate-source voltage of ± 20 V. The gate voltage was supplied by two HCPL-3120

optocouplers which also isolate the control circuit from the high voltage output of the switch. The HEXFET was protected by BJT transistors Q1, Q2, Q3 and Q4 from excess current. Q1 and Q3 will switch on to provide a short circuit path between gate and source when the current exceeds maximum rating. The high voltage power supply is connected to the sample through the upper HEXFET by a +5 V pulse signal at the trigger input for the duration of the trigger pulse

3.5.3 Amplifier

The induced photocurrent signal across the sampling resistor is amplified by a two-stage wideband voltage differential amplifier. Figure 3.13 shows the amplifier design schematic diagram. The first stage of the amplifier is made up of an analog device AD830 wide bandwidth, high common mode rejection ratio CMRR video amplifier. This stage amplifies the differential photocurrent signal from the displacement current signal. The second stage uses an analog device AD827 non-inverting operational amplifier designed to have 16 dB gain above noise floor level of the oscilloscope and to drive the capacitance of the coaxial cable connecting the amplifier and the oscilloscope. A protection circuit is connected between the amplifier inputs to protect the amplifier from high voltage switching transient. The protection circuit makes use of a Maxim MAX318, a normally open CMOS analog SPST switch. A timing control circuit of an LS123 monostable multivibrator and an LS74 positive-clocked D flip-flop provides timing control for the switch. The protection circuit and the timing pulse duration is shown in figure 3.14. The amplifier is estimated to have a small signal bandwidth of 12 MHz and since the transit time of a-Se is more than 1 μs, it implies that the amplifier's performance is sufficient for the TOF/IFTOF experiment measurement for the a-Se samples.

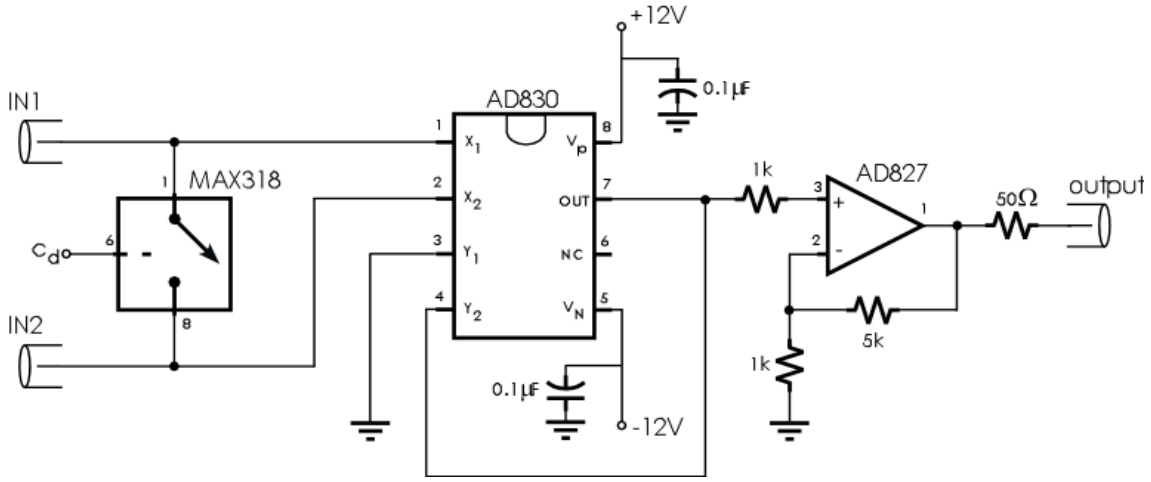

Figure 3.14 A two-stage wide bandwidth differential amplifier with 16 dB gain. Circuit designed by Dr. Robert Johanson.

3.5.4 Laser and Trigger System

A nitrogen pumped LN103C laser with pulse duration of ~300 ps, power 250 kW and spectral width of 337.1 nm (UV) with a 0.1 nm spread was used was used as the photoexcitation source for the TOF/IFTOF experiment. A Newport optical fiber adapter was used to feed in the laser pulse into the lead chamber where samples were tested. The laser is triggered by two TTL signals, REG and LOW, through BNC connections which are used fire the laser by creating a high voltage discharge across a spark gap.

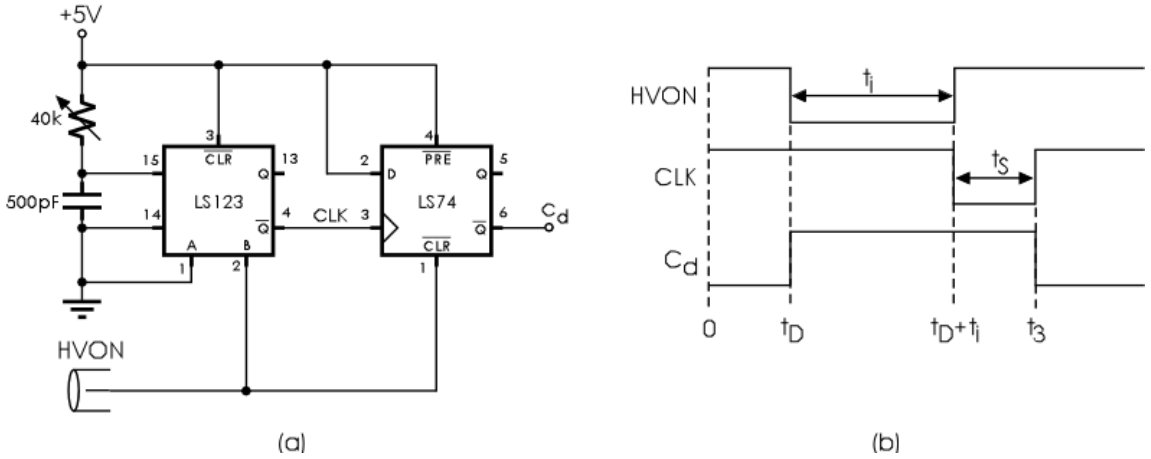

Figure 3.15 (a) The protection circuit system. (b) The timing diagram. (After [4])

The first signal, REG, which is a +5 V pulse of at least 100 ns in duration triggers the input to charge the laser and between 30 and 50 µs later, the second +5 V signal, LOW, of at least 100 ns in duration triggers the laser to fire which produces laser at the exit aperture.

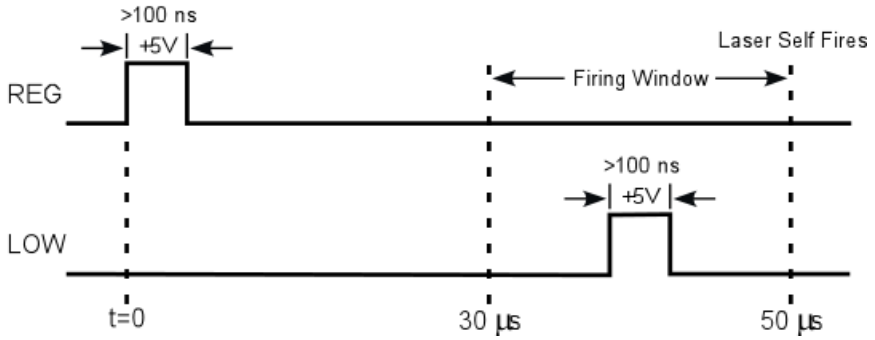

Figure 3.16 Trigger timing for the LN103C laser. (After Fogal [8])

For the laser to fire, a high voltage discharge is required through the spark gap circuit. The laser trigger signals were coupled optically to the laser control input to prevent feedback of the large switching transient from the control circuit which can interfere with the measurement.

The timing of trigger signals is provided by a PCICTR05 counter board interfaced with the PCI bus of a personal computer. The counter board uses an AMD 9513 timer/counter chip which is fully supported by the Computer Boards Universal Library of programming function providing high-level software control of the counter registers on the AMD 9513. The timing chip is made up of five 16 bit up/down counter. A LabView graphic user interface (GUI) program is written to call the C++ functions.

A trigger generator circuit as shown in Figure 3.16 interfaced the TOF/IFTOF system with the counter board. The output of the counter board is connected to the interface circuit, placed in a separate aluminum case, by a ribbon cable. A switch is used to manually control the position of the high voltage bias by selecting one of the three settings; on, pulsed and off. For the TOF/IFTOF experiment, the switch is set on a pulsed position

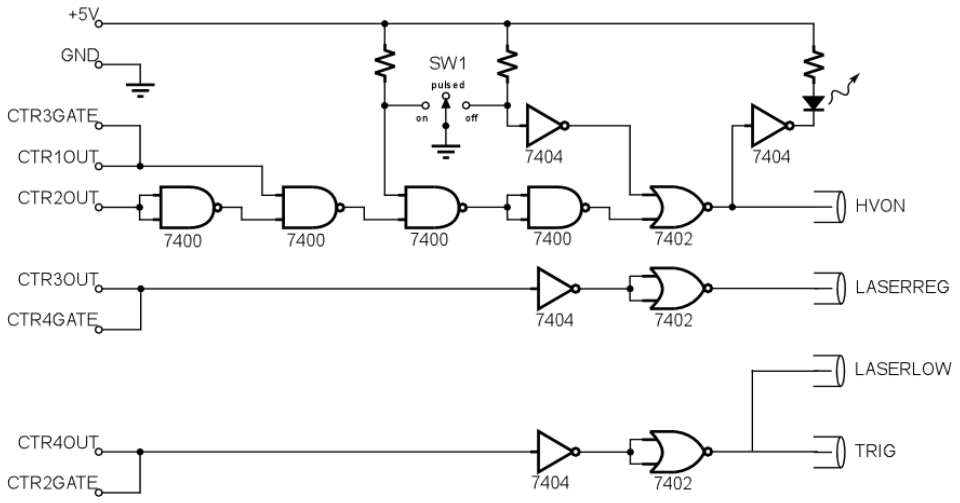

Figure 3.17 The PCI-CTR05 interface circuit for generating the trigger system for the TOF/IFTOF system. (After Fogal [8])

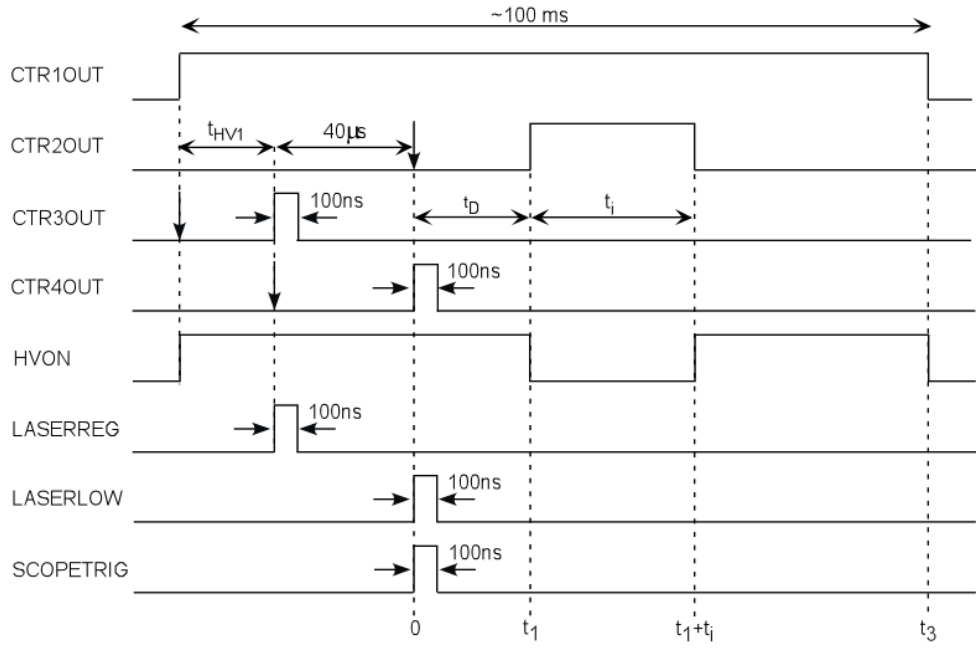

Figure 3.18 Timing signal from the PCI-CTR05 counter board and interface circuit. (After Fogal [8])

Figure 3.17 shows the timing waveform at the counter board output and the resulting signals when the switch is in pulsed position. The application of the bias on the sample is controlled

by the HVON trigger signal which triggers the high voltage switch. The displacement current caused by the application of high voltage bias is allowed to decay to a very small level by a delay of t_{HV1}. A 100 ns LASERREG pulse initiates the charging of the laser and then after a 40 μs delay, a 100 ns LASERLOW pulse fires the laser and inject charge into the sample. The oscilloscope is triggered simultaneously with the firing of the laser to capture the photocurrent signal. For TOF experiment, the HVON signal is not interrupted with the bias applied for a sufficiently long time to collect all the charge carriers in the bottom electrode. However, during the IFTOF experiment, the bias is interrupted after a specified delay time t_D by the user and after the interruption time, the bias is reapplied for a sufficient time to collect all the remaining charge carries.

3.5.5 Data Acquisition System

The TOF/IFTOF experiment signal is captured by an 8-bit Tektronix TDS210 digital oscilloscope of a sampling rate of 1 GS/s. Experimental data are collected by a personal computer through a GBIB interface connected to the oscilloscope. The output of the amplifier is connected to the channel 1 of the oscilloscope and the high voltage controlling signal from the command terminal is connected to channel 2 of the oscilloscope. A GUI interface realized through LabView software is to control and manipulate parameters of the experiment. The parameters of the experiment include changing between TOF and IFTOF modes of the experiment, the interruption time for the IFTOF experiment, delay time and laser trigger time. The GUI is also used to capture both the photocurrent signal and background signals while an accurate photocurrent signal is captured by background subtraction. The captured waveform can be stored in the text.txt format on the PC. Carrie mobility and trapping time calculation is also provided by the graphic user interface program. Figure 3.17 shows the picture of the GUI used for this study.

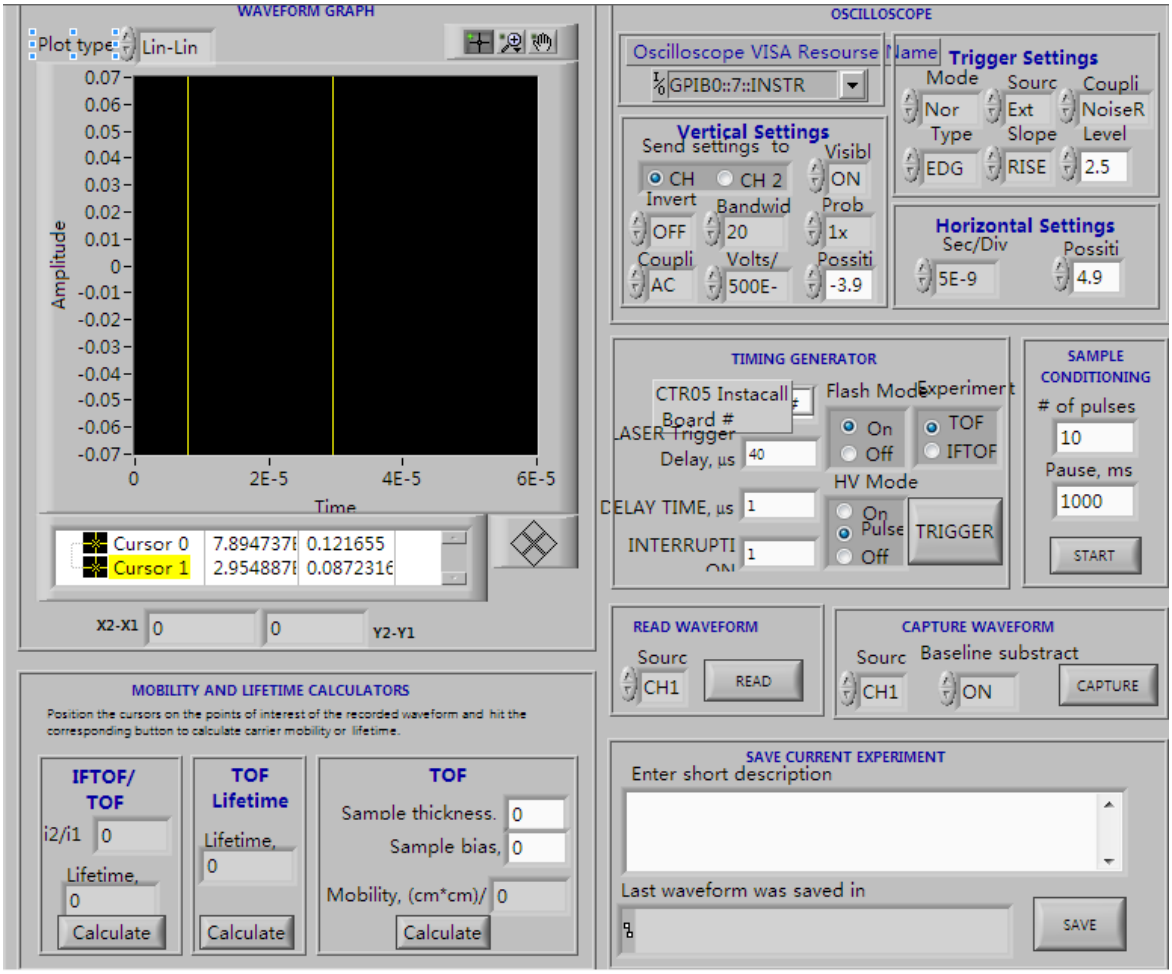

Figure 3.19 GUI interface for TOF/IFTOF in LabView.

3.6 X-ray Induced Carrier-trapping Lifetime Changes

The goals of this research work are to study the effect of accumulated X-ray dose on the carrier-trapping lifetime at room temperature and at 35.5 ºC and to study the damage recovery process at room temperature, at 35.5 ºC and under the LED light of different wavelengths and intensities. The accumulated dose measurement and the lifetime recovery measurements were developed to achieve these goals.

3.6.1 Accumulated Dose Measurement

This measurement studies the effect of accumulated dose of X-ray on the carrier-trapping lifetime. The changes in the trapping lifetime because of X-ray irradiation is observed in this measurement. The initial lifetime of the sample under investigation is measured by the conventional IFTOF method. The sample was irradiated by X-ray at 70 kVp tube voltage for time t seconds and the carrier lifetime of the sample is measured immediately after the X-ray irradiation. This process is repeated at regular time interval until the carrier-trapping lifetime drops significantly.

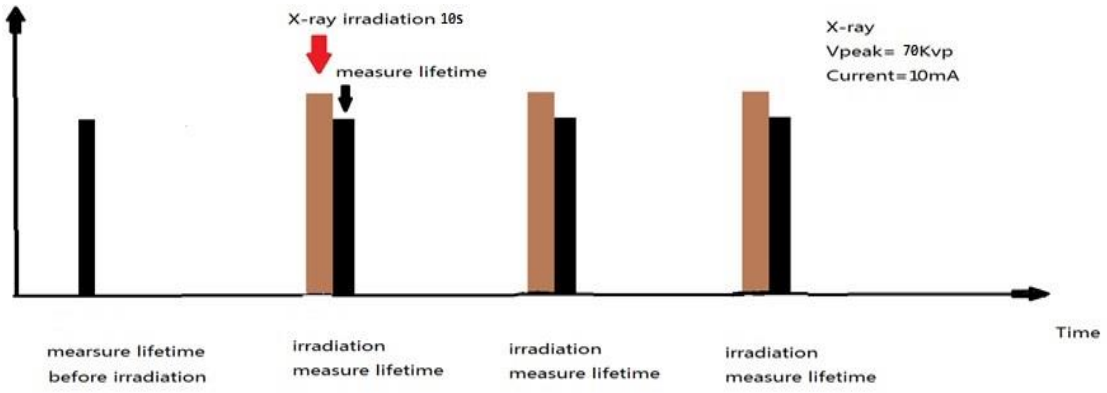

Figure 3.20 Accumulated dose measurement procedure

3.6.2 Lifetime Recovery Measurement

The carrier-trapping lifetime changes induced in the a-Se sample because of X-ray irradiation recovers gradually. The lifetime recovery measurement studies these changes back to the equilibrium point, that is, back to the original starting point. During this process, the IFTOF measurement was performed where the carrier-trapping lifetime was recorded every t(n) seconds for n time where

$$t(n) = \{t_{\mathrm{n}} \in \mathrm{T} \parallel \ t_{\mathrm{n}} < t_{\mathrm{n+1}}\}, \qquad \mathrm{T} = \{t_{1,} t_2, \dots\} \tag{3.4}$$

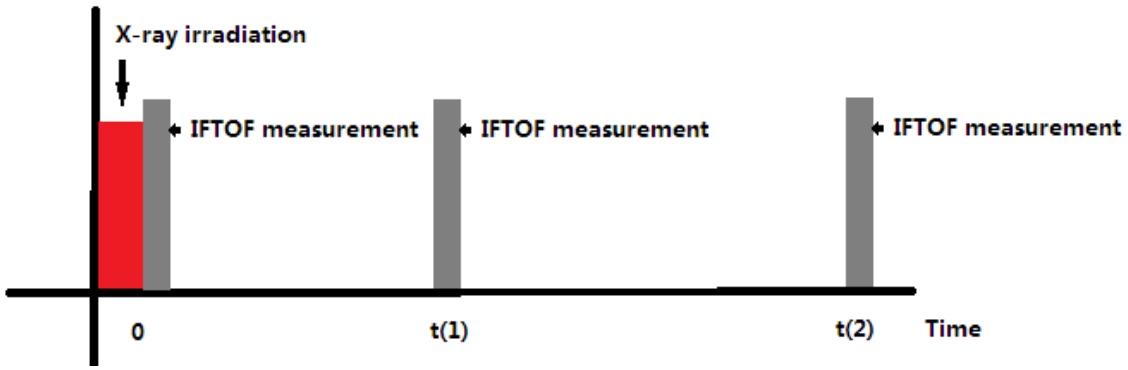

Figure 3.21 Recovery measurement procedure

The time interval between recovery measurements is not uniform because some recovery processes are more rapid than others. The experiment process is depicted in Figure 2.20. The experiment was terminated when the carrier-trapping time approximately equal to the initial carrier-trapping time before X-ray irradiation. The lifetime recovery measurements were conducted for samples at different temperature and under LED lights of different wavelengths and intensities.

3.7 Temperature Control Systems

Part of the goals of this study is to investigate the X-ray induced effect of a carrier-trapping lifetime and the recovery process at a different temperature, specifically room temperature and 35.5 ^{o}C. This is to investigate if temperature affects the rate of decrease of the carrier-trapping lifetime under X-ray Irradiation. The temperature control consists of a heater and cooler. The heater uses a 50 ohms resistor heater as its source and the cooling source makes use of a CP60440 Peltier cooler from CUI Inc. The Peltier cooler is 40×40 mm in dimension with a 6 A input current which draws heat from the sample and a continuous flowing water serves as a heat sink to dissipate heat. The system is controlled by an Omega CNI3252-C24 temperature controller through the thermal coupling. An external +20V dc source powers the temperature controller. The schematic diagram of the temperature control system is shown in Figure 3.20. The temperature controller cuts current from the heater once the set temperature is reached while the cooling system is activated simultaneously to stop

further heating. The error margin for the temperature control system is ± 0.5 ^{o}C from the set temperature.

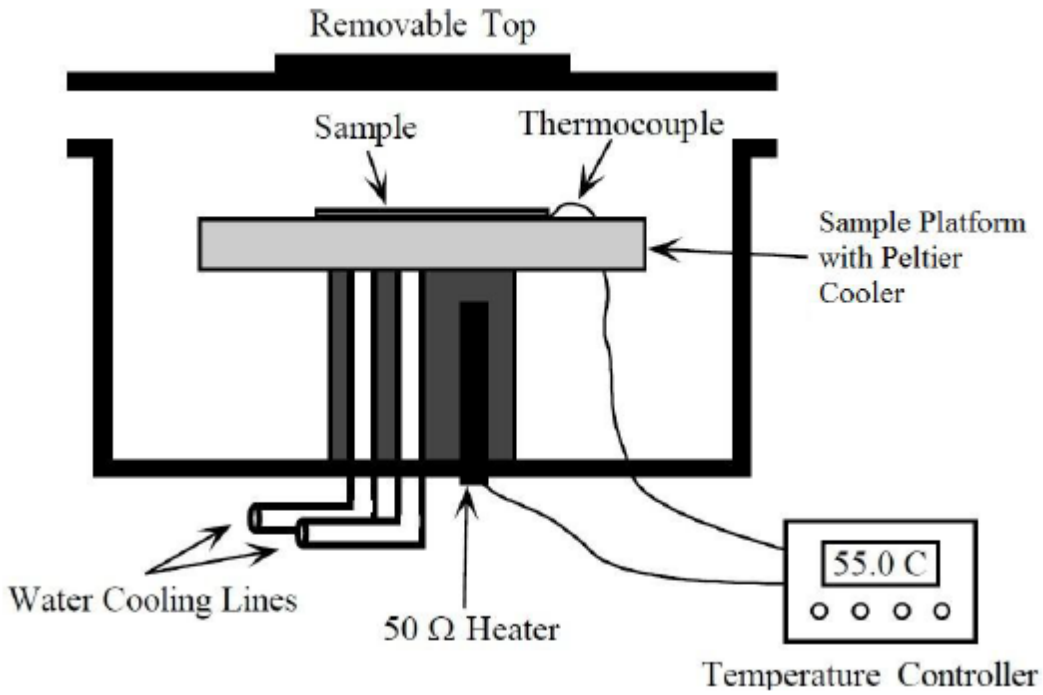

Figure 3.22 Thermal controlling system chamber. After [4])

3.8 Summary

This chapter has presented a detailed procedure for the experiments used in this research. The samples used in this study, pure a-Se films and stabilized a-Se film, were fabricated through the conventional vapor deposition method with a thickness ranging from 50 μm to 200 μm. The sputtering system was used to deposit semi-transparent gold top electrode on the samples. This chapter also presents the X-ray dose estimation method. A Gendex GX 1000 X-ray tube system is used as the X-ray source and a dosimeter together with an ion chamber is used to measure the X-ray exposure.

The TOF/IFTOF experimental technique setup for the measurement of charge carrier transport is discussed in this section. Charge carriers are photoexcited in the sample by a

nitrogen-pumped LN103C laser with pulse duration of ~ 300 ps, power 250 kW and spectrum with a peak at of 337.1 nm (UV) and a width of 0.1 nm . The charge carriers are drifted through the sample by an applied high voltage bias. The drift of charge carriers induces a photocurrent signal in the external circuit. During the IFTOF process, the voltage bias is switched off and then on after an interruption time. A grounded bridge network is used to eliminate the displacement current originating from the high voltage switching transients. The measured signal is amplified by a differential amplifier and captured by a digital oscilloscope. A GUI created from the LabView program is created on a personal computer to control the TOF/IFTOF experiment setup.

The X-ray induced lifetime changes in stabilized a-Se sample were investigated by the accumulated dose measurement and the lifetime recovery measurements during which TOF/IFTOF experiments were carried out. Repeated IFTOF measurement was taken after X-ray irradiation on the sample under study until the expected dose is deposited on the sample while the carrier-trapping lifetime recovery was studied by taking IFTOF measurements at intervals until sample fully recovers to its pre-irradiation state. The carrier-trapping lifetime recovery measurement was also observed at different temperature and under LED lights of different wavelengths and intensities. A 50 ohms resistance heater and a Peltier cooler are used to actualize the thermal coupling process with an Omega CNI3252-C24 temperature controller.

4. RESULT AND DISCUSSION

4.1 Introduction

The previous chapters have introduced the concepts of time-of-flight (TOF) and interrupted-field-time-of-flight (IFTOF) followed by the experimental procedure. Chapter 2 explains the theoretical background for describing the transport of injected carriers in amorphous semiconductors. Chapter 3 elucidates the experimental procedures from sample preparation to the measurement of X-ray induced carrier-trapping lifetime changes. This chapter presents the results of experiments conducted in this work. These results include the x-ray dose deposited in the a-Se sample, the effect of x-ray irradiation on the carrier lifetime for both holes and electrons at 23.5^{o}C and 35.5^{o}C, the normalized lifetime recovery at both 23.5^{o}C and 35.5^{o}C.

All samples used in this project are pure a-Se for hole transport measurements, a-Se: 0.3%: 2.5ppm Cl and a-Se: 0.5%: 10ppm Cl for electron transport measurements. Sample thickness ranges from 50 μm to 200 μm with a variance of $\pm$5 μm at different positions on the sample. Both the electron and hole life time change with respect to absorbed accumulated dose under x-ray irradiation. After irradiation with x-rays, the lifetime decreases and then recovers to its equilibrium point after the cessation of x-ray irradiation. The process of recovery was observed at different temperatures.

4.2 X-ray Dose Deposited in a-Se Samples

The amount of X-ray dose deposited in each sample at an X-ray tube peak voltage depends on the distance between the sample and the X-ray source and the filament current of the X-ray tube. X-ray absorbed by a-Se samples is estimated by first using Keithley 35050 Ion Chamber with the Keithley 35050 Dosimeter to measure X-ray exposure at different sample positions and X-ray filament current. A peak voltage of 70 kVp was chosen for X-ray dose measurements. The results of the X-ray dose in air, measured by the Keithley dosimeter and the ion chamber, with respect to the inverse square of the distance of the sample from the X-ray source is shown in Figure 4.1.

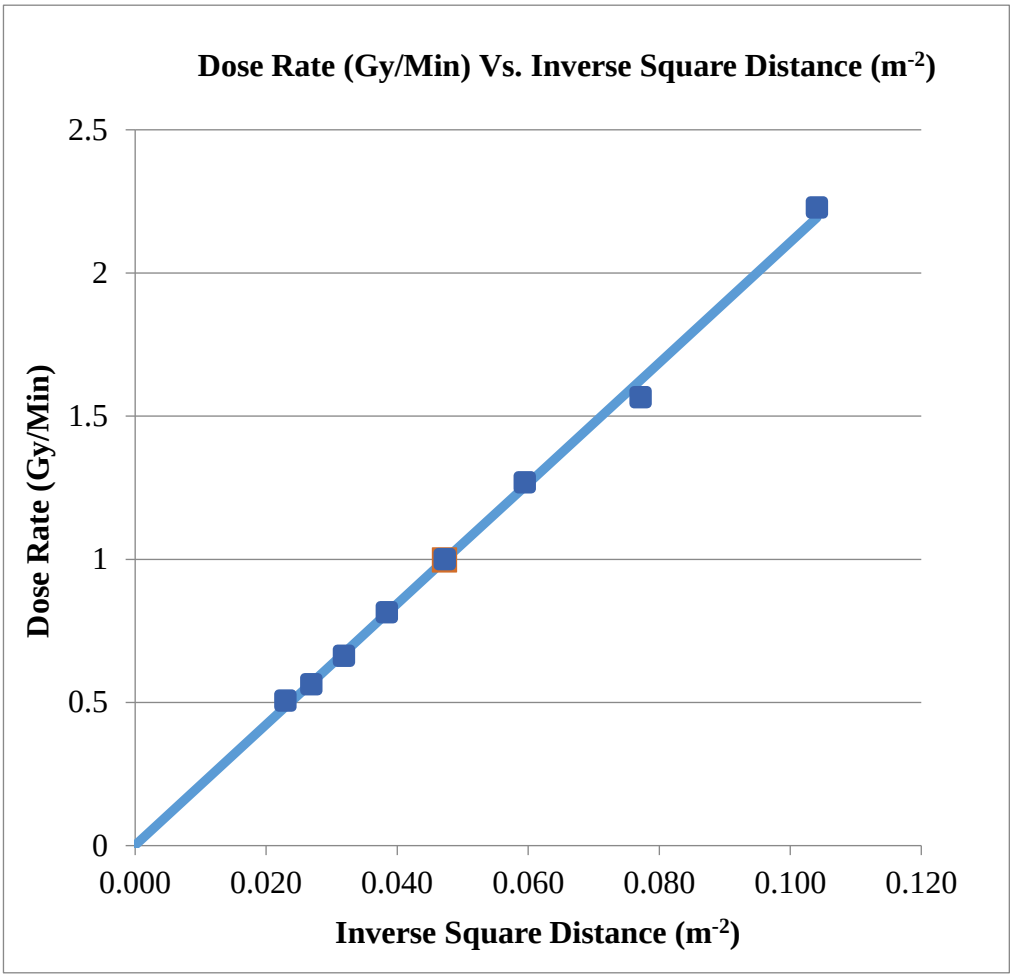

Figure 4.1 X-ray dose in air in Gy/minutes vs the inverse square distance of the sample from the X-ray source.

The dose deposited on a-Se samples is estimated by the parameters from exposure measurement and sample parameters such as sample area, thickness, density, and absorption coefficient. The mass attenuation and mass energy coefficients of selenium are interpolated from data from the NIST website. The absorbed dose is a function of X-ray photon energy per unit area per Roentgen known as the energy fluence. The distribution is simulated at a tube voltage of 70 kVp from a simulation program by Siemens as shown in Figure 2.11 in Chapter 2 [41]. The X-ray attenuation coefficients and mass-energy coefficients of Selenium and dry air interpolated from data from the NIST website are shown in Figures 4.2 and 4.3 respectively.

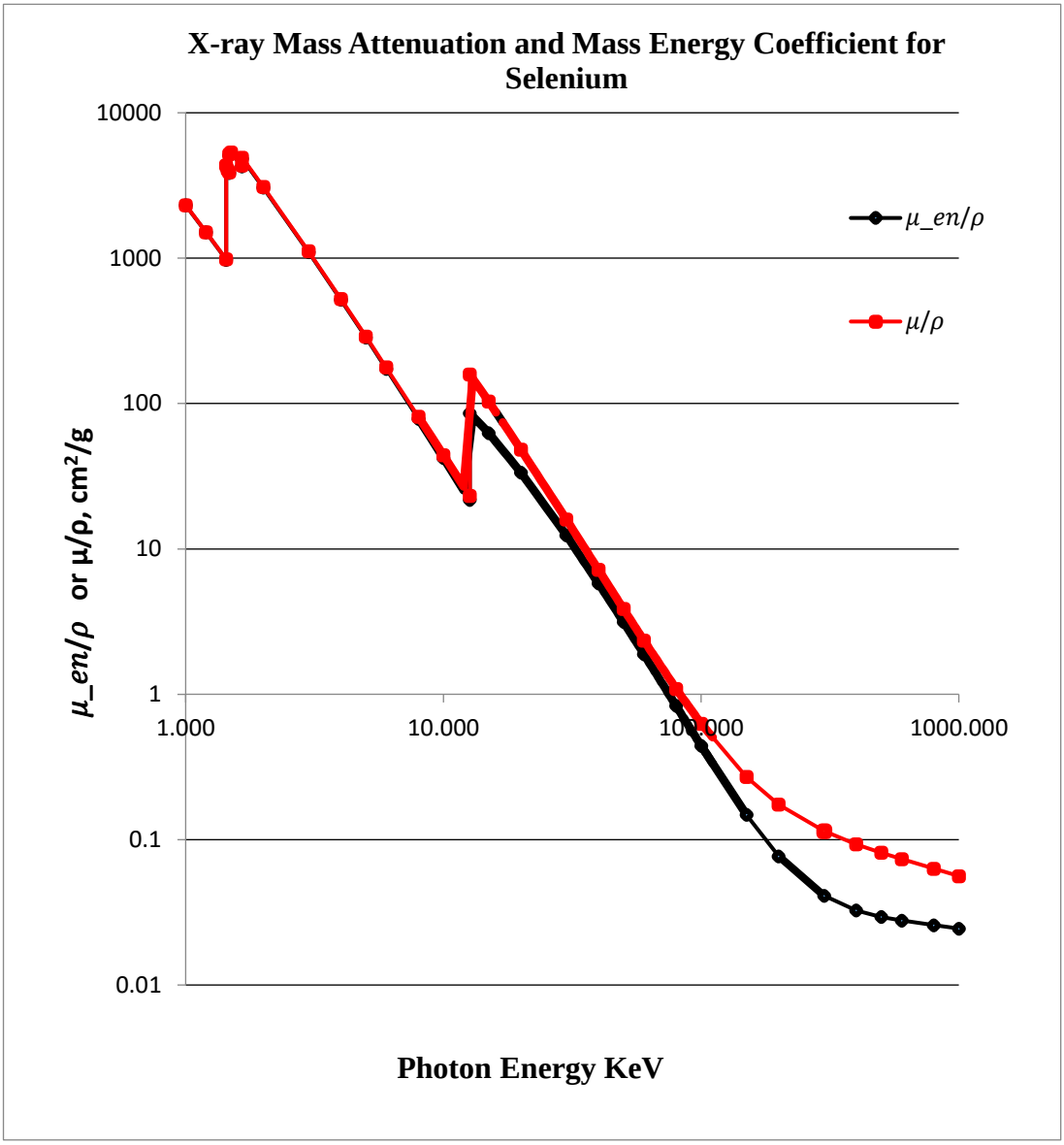

Figure 4.2 X-ray mass attenuation and the mass-energy coefficient for selenium vs photon energy. Data interpolated from data from NIST [66].

The units of the mass attenuation coefficient and energy absorption coefficient provided by the NIST website are cm^2/g and energy is expressed in keV. The value for the density of air at room temperature from the NIST data is $\rho_{\mathrm{air}} = 1.205 \times 10^{-3}\mathrm{g/cm}^3$. It is assumed that the X-ray dose is distributed uniformly over the area of the sample.

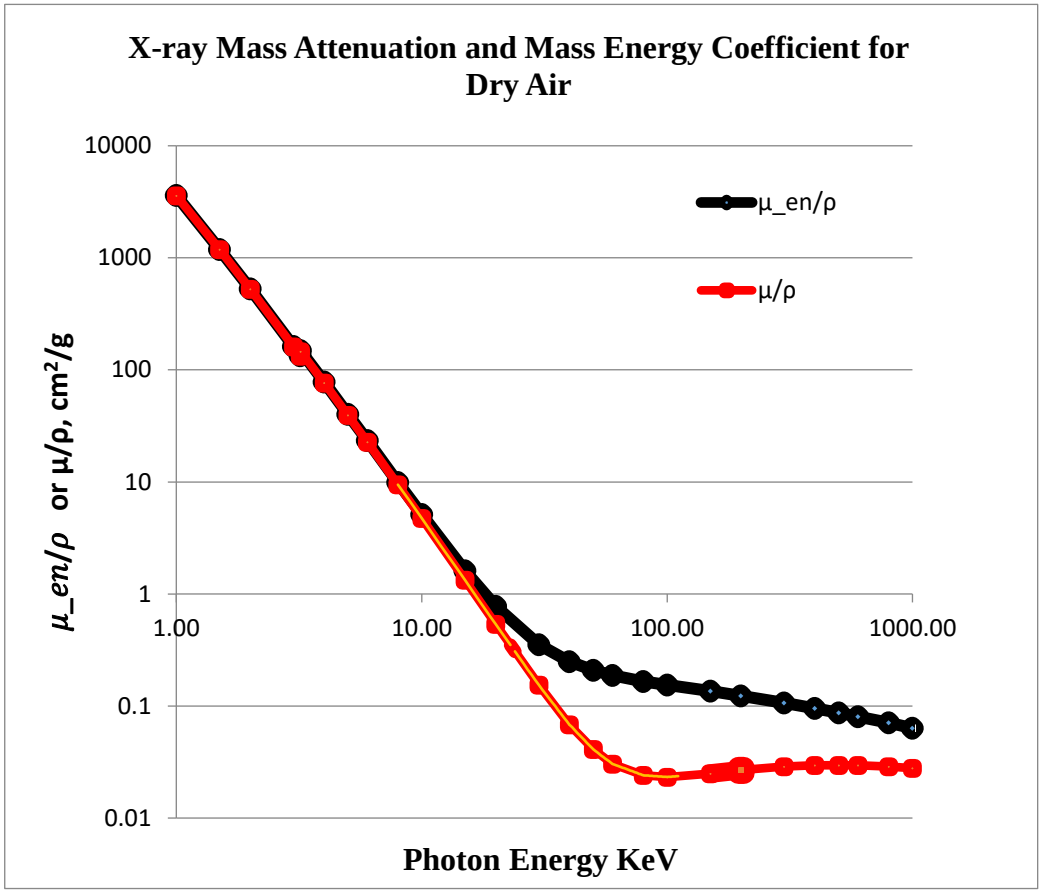

Figure 4.3 X-ray mass attenuation and the mass-energy coefficient for dry air vs photon energy. Data interpolated from data from NIST [66].

The X-ray does in air, which is the exposure in Roentgen, was measured by the Keithley dosimeter and ion chamber which has been pre-calibrated with a calibration factor on 0.7 Roentgen/volt. A digital voltmeter was connected to the dosimeter to read the output voltage which was converted to Roentgen by the calibration factor. Since 1 R is equivalent to 0.00877 Gy, this value is use to estimate the incident dose on the samples which is the dose in air ($D_{air,\ exp}$) as explained in Chapter 2. The absorbed X-ray dose rate per second results from the dosimeter for samples at X-ray tube peak voltage 70 kVp and tube current of 15 mA is shown in Table 4.1. The average energy of the incident X-ray beam is 37.61 keV

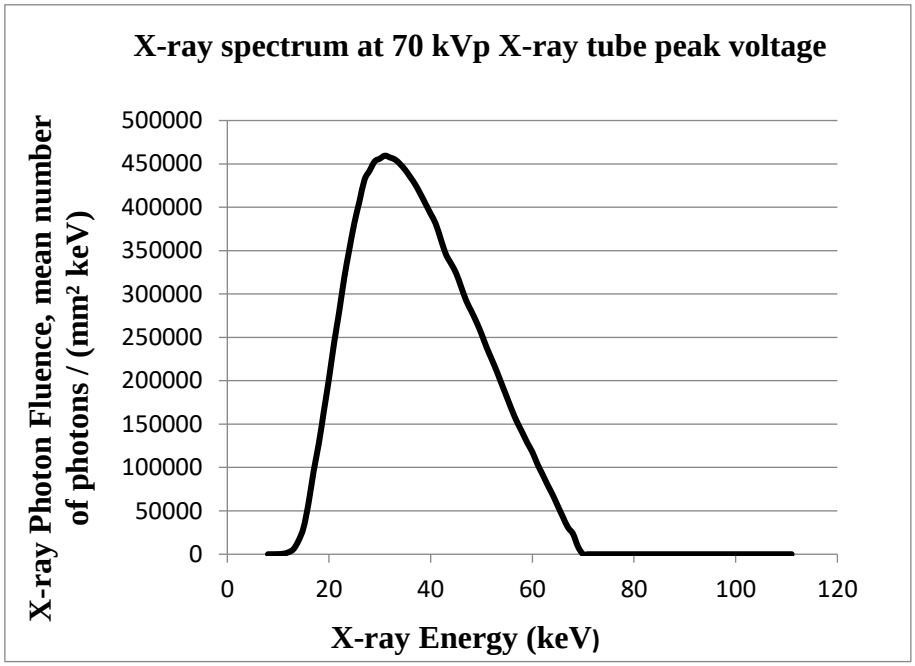

Figure 4.4 Simulated X-ray spectrum at 70 kVp X-ray tube voltage from Siemens for dose of 1 mGy [41]

Table 4.1 Deposited X-ray dose rate in Gy/s at Air Dose rates 5.11 R/s at distance 280 mm from the X-ray source. The X-ray source tube voltage is 70 kVp X-ray tube voltage and 15mA filament current with average energy of 37.37 keV

Sample	**Thickness (µm)**	**Delivered Dose Rate (Gy/s)**
R98#2 (a-Se: 0.5% As – 10ppm Cl)	83	2.35
R774#3 (a-Se: 0.5% As)	105	2.20
R821#3 (a-Se: 0.3% As: 2.5ppm Cl)	88	2.31
R822#1 (a-Se: 0.5% As)	151	1.94

4.3 Charge Carrier Mobility and Lifetime

The charge transport properties of a-Se were measured using the TOF and IFTOF measurement techniques. The TOF measures the carrier mobility while the IFTOF measures the carrier-trapping lifetime (deep trap capture time). The theory behind the experiments has been presented in previous chapters. The measurement techniques described in Chapter 3 were used to capture induced transient photocurrent signals when a very narrow charge sheet is photogenerated by a strongly absorbed short pulse of light. The sample is suitably biased, and the light intensity is kept low to ensure small signal conditions. The applied voltage is removed when drifting charge carriers reach a point in the sample for IFTOF measurements, allowing the charge carrier to interact with the localized states in the mobility gap of the sample, and then restored to drift remaining charge carries to the collecting electrode. For hole measurement, the top electrode is connected to the positive polarity of the applied voltage. This enables the generated electrons from the photogenerated EHPs to be quickly collected at the top electrode leaving only holes in the charge sheet to drift through the sample. The polarity of the applied voltage is reversed for electron transport measurements.

Dispersion of charge carriers in the charge packet during transit, which is because of multiple trapping, produces a photocurrent tail in the TOF signal. The transit time t_T of the charge carrier is the average time it takes for a charge carrier to drift from the point of generation to the point of collection at the electrode. This is measured from the TOF photocurrent signal by using the half peak magnitude method. The carrier mobility is calculated from the measured transit time from the photocurrent waveform using the relation $\mu = L^2/Vt_T$, from Equation 3.3. The carrier trapping lifetime of a-Se samples was obtained from the IFTOF experiments by using a semi-logarithmic plot of the ratio of the photocurrent after and before interruption against the interruption time. The slope of the plot gives the carrier trapping lifetime. Another way to compute the carrier trapping lifetime from the IFTOF measurement is by computing the fractional recovered photocurrent.

Figures 4.5 and 4.6 shows the photocurrent waveforms from the TOF and the IFTOF measurements.

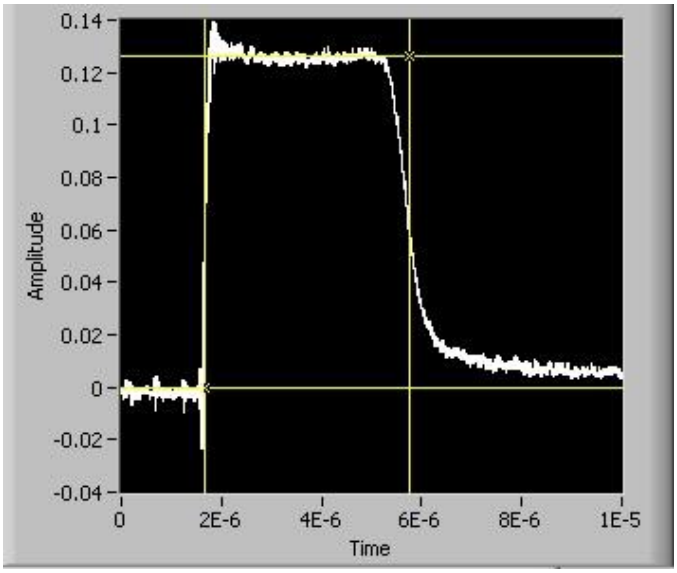

(a)

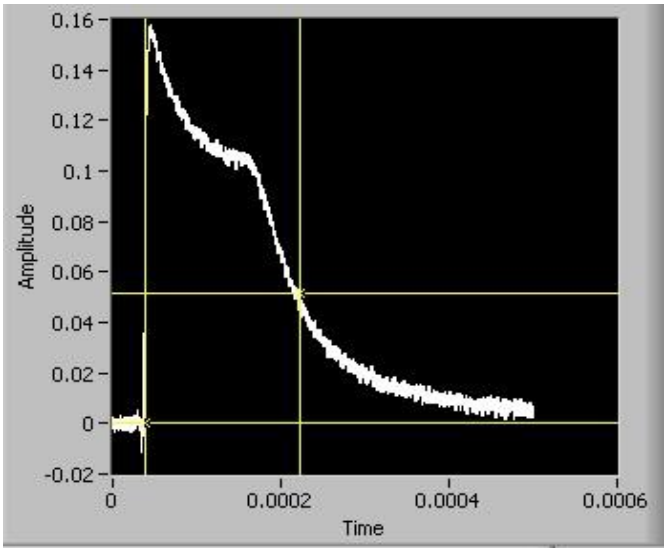

(b)

Figure 4.5 (a) Hole TOF waveform of a 151 μm thick film of a stabilized a-Se with an applied field of 1.99 V/μm gives transit time of 5.54 μs, μ_h = 0.137 cm^2/V.s . (b) Electron TOF of an 88 μm thick film, applied field is 1.14 V/μm and transit time 286.81 μs, μ_e = 0.003 cm^2/V.s

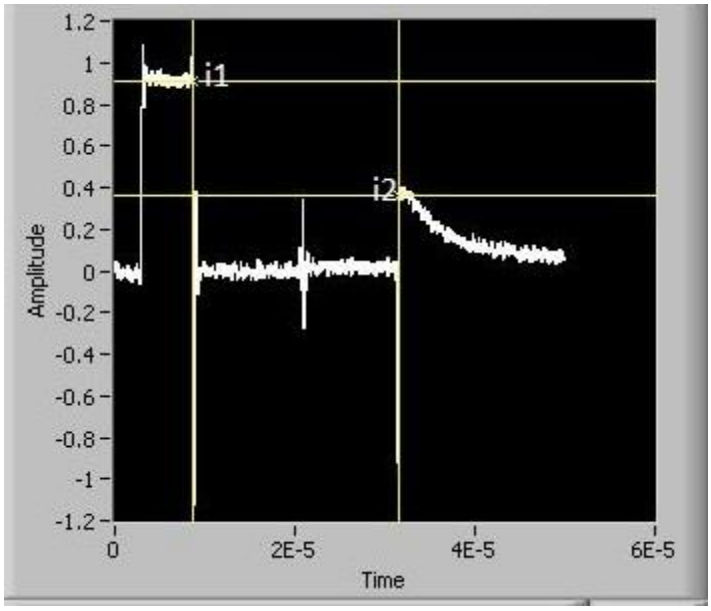

(a)

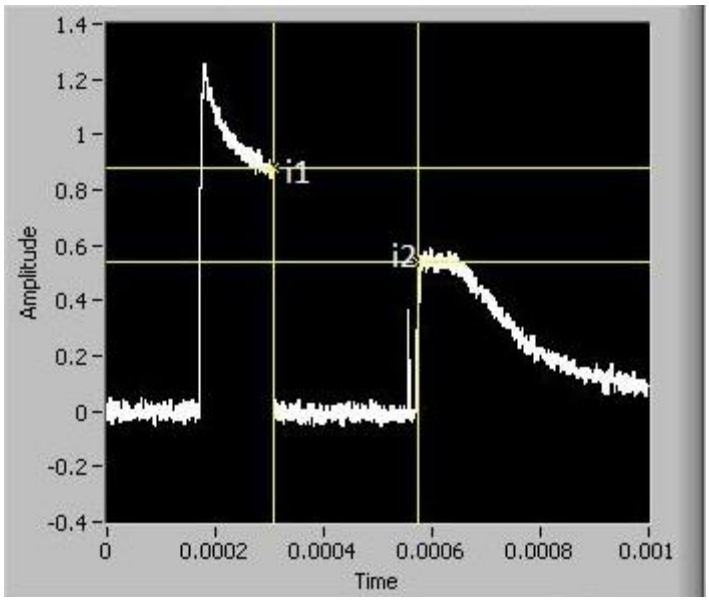

(b)

Figure 4.6 (a) Hole IFTOF waveform for a 105 μm thick film sample with interruption time of 12 μs, τ_h= 13.92 μs. (b) Electron IFTOF waveform captured for an 88 μm thick film with interruption time of 250 μs, τ_e= 574.29 μs.

The fractional recovered photocurrent computation is done by measuring the magnitudes of the photocurrent signal immediately before and after interruption t_1 and t_2 and determined by $i(t_2)/i(t_1) = \exp(-t_i/\tau)$, where $t_i = t_2 - t_1$ is the interruption time.

Table 4.2 Measured carrier mobility

Carrier	**Hole Mobility (cm^2/V.s)**
Hole	0.137 ± 0.007
Electron	0.003 ± 0.0002

Table 4.3 Measured carrier trapping lifetime before irradiation

Sample	**Hole Lifetime (μs)**
Hole	13.92 ± 0.69
Electron	574 ± 29

4.3.1 X-ray Irradiation Effect on Lifetime

The sequence for the irradiation experiment was presented in chapter 3. The carrier trapping lifetime is measured followed by X-ray irradiation under an applied electric field. X-ray dose deposited in the sample for each irradiation is a function of time of exposure. Dose deposited is the product of the dose rate and the time of exposure as shown in equation 4.1. Three different dose rates are chosen for both hole and electron measurements are listed in table 4.2.

$$\text{Dose (Gy)} = \text{Dose Rate } \left(\frac{\text{Gy}}{\text{s}}\right) \times \text{Time (s)} \qquad 4.1$$

Table 4.4 Different dose rate for electrons and holes measurement

Electron (Gy/s)	2.02	2.16	2.31
Hole (Gy/s)	1.91	2.05	2.20

After each X-ray irradiation, the carrier trapping lifetime is measured to observe the effect of the X-ray radiation on the carrier trapping time. The values of the trapping lifetime are normalized with respect to the initial trapping lifetime before X-ray irradiation.

$$\tau_{\text{normalized}} = \frac{\tau_{\text{after X-ray irradiation}}}{\tau_{\text{initial before irradiation.}}} = \frac{\tau}{\tau_0} \qquad 4.2$$

where τ_0 is the original lifetime value before any x-ray exposure and τ is the lifetime value after exposure.

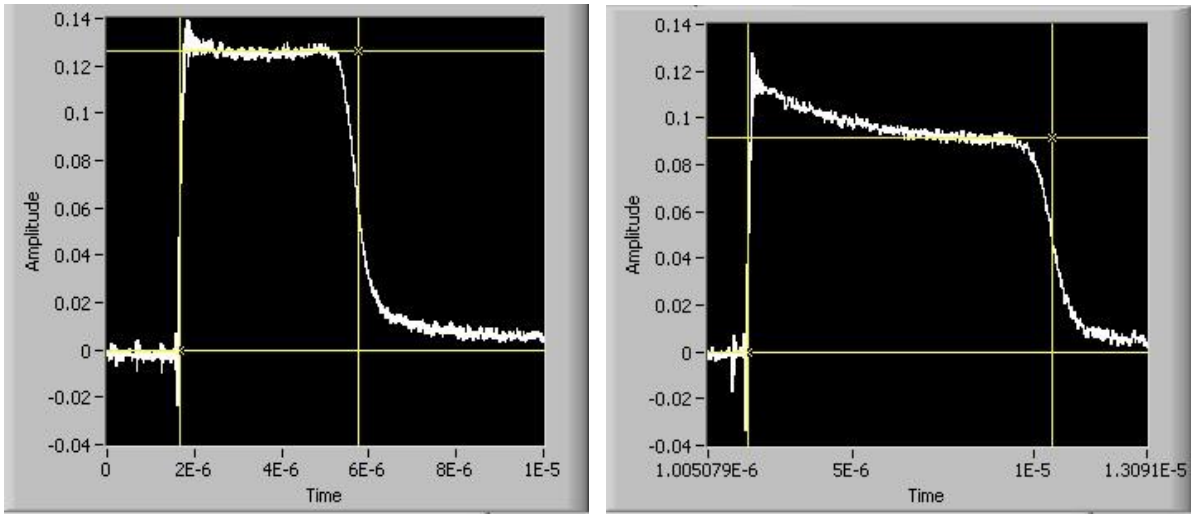

(a) (b)

Figure 4.7 (a) Hole TOF signal captured before x-ray exposure. (b) Hole TOF signal captured after x-ray exposure.

Figure 4.7 (a) shows captured hole waveform for TOF measurement before x-ray exposure and Figure 4.7 (b) shows the captured waveform after the sample has been exposed to x-ray radiation.

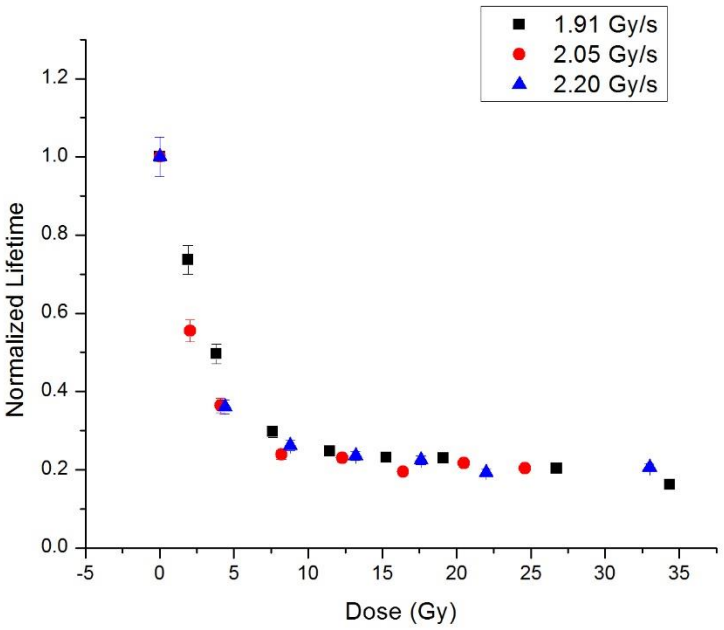

Figure 4.8 X-ray Irradiation effect on Normalized hole-trapping lifetime at different dose rates

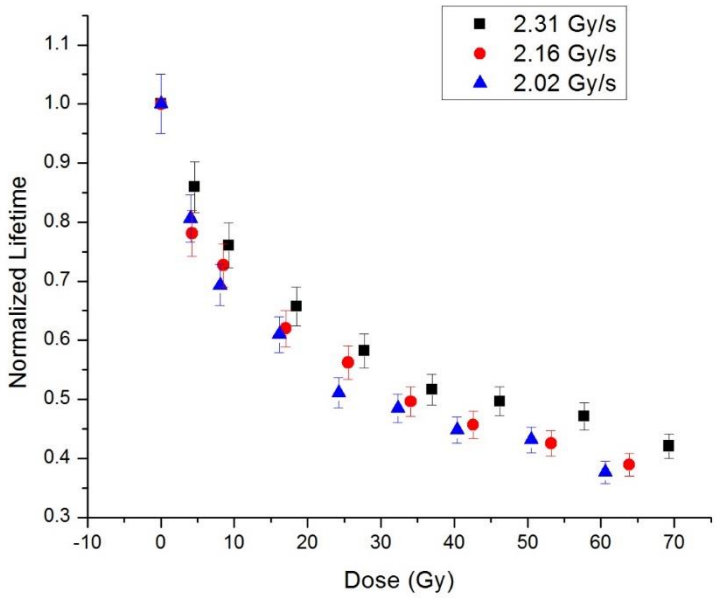

Figure 4.9 X-ray Irradiation effect on Normalized electron-trapping lifetime at different dose rates

The accumulated dose experiment was terminated when the carrier trapping lifetime is significantly reduced to approximately 40% of the initial value before irradiation. The result for the hole and electron measurements are shown in Figure 4.8 and 4.9 respectively.

At an accumulated dose of about 35 Gy, the hole-trapping lifetime is reduced to about 20% of the initial lifetime. Electron trapping lifetime is reduced up to 40% of the initial lifetime at an accumulated dose of 70 Gy at 2.31 Gy/s dose rate, and about 60 Gy at 2.02 Gy/s. The rate of reduction in the normalized trapping lifetime appears to be higher in the hole case than that for electrons.

The normalized carrier trapping time decreases with X-ray dose during the accumulated dose measurement. When X-ray energy is deposited in the a-Se sample, new defects are generated in the sample. The increase in the number of defects in the sample causes a decrease in the average carrier trapping time. For both hole and electron accumulated dose measurements, the normalized trapping lifetime decays reciprocally with respect to dose. The carrier trapping lifetime is inversely proportional to the concentration of deep traps in the sample. The carrier trapping lifetime before irradiation is closely related to the intrinsic defect concentration, so that it can, be written as [4]

$$\tau_{\mathrm{o}} = \frac{1}{CN_0} \qquad 4.3$$

where C is the capturing coefficient and N_{o} is the initial number of defect or carrier trap density. The deposited X-ray dose generates new defects with a concentration N_{x} in the band gap.

$$N_{\mathrm{x}} \propto D \qquad 4.4$$

where D is the deposited x-ray dose.

The total concentration of defects in the sample after X-ray irradiation is

$$N = N_0 + N_{\mathrm{x}} \qquad 4.5$$

However,

$$N_0 = \frac{1}{C\tau_0} \text{ and } N = \frac{1}{C\tau} \quad 4.6$$

Therefore, using equation4.3, 4.4 and 4.6 equation 4.5 transforms to

$$\frac{1}{\tau} = \frac{1}{\tau_0} + AD \quad 4.7$$

where *A* is a constant. Rearranging equation 4.7 gives

$$\frac{\tau}{\tau_0} = \frac{1}{1+AD} \quad 4.8$$

The value of *A* for each X-ray dose rate was obtained from the normalized carrier lifetime vs. accumulated dose curve by a rational curve fitting. Tables 4.5 and 4.6 show the normalized lifetime change rate at different dose rate for hole and electron respectively.

Table 4.5 Normalized lifetime change rate dependence on dose rate for hole

Dose Rate (Gy/s)	Normalized Lifetime Change Rate, *A* (Gy^{-1})
1.91	0.177 ± 0.009
2.05	0.218 ± 0.011
2.20	0.180 ± 0.009

The normalized lifetime change rate varies very slightly with the X-ray irradiation dose rate. Figure 4.9 shows the variation of the normalized lifetime change rate with the dose rate. Increase in dose rate does not have a significant effect on the normalized lifetime change rate for both electron and hole.

The accumulated dose measurement was done at 23.5 ºC and at 35.5 ºC to investigate the temperature effect on the dependence of the lifetime on accumulated dose in a-Se samples. Although the study of electron trapping lifetime change with temperature has been previously conducted by Michael Walornyj [4], part of the goal of this work is to compare the temperature effect on the trapping lifetime of holes and electrons. Normalized lifetime change rate dependence on dose rate

Table 4.6 Normalized lifetime change rate dependence on dose rate for electron

Dose Rate (Gy/s)	Normalized Lifetime Change Rate, A (Gy^{-1})
2.02	0.032 ± 0.016
2.16	0.029 ± 0.014
2.31	0.023 ± 0.011

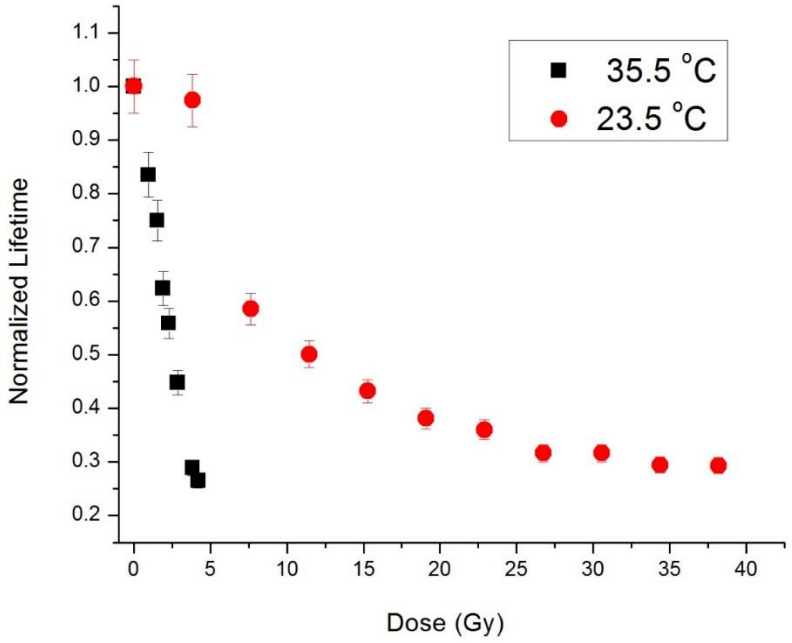

Figure 4.10 X-ray dose effect on the normalized hole trapping lifetime at 23.5 ºC and at 35.5 ºC

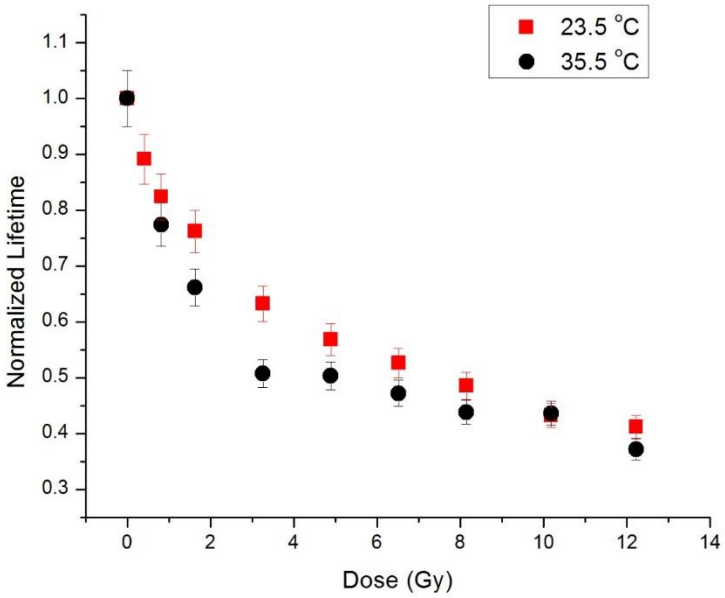

Figure 4.11 X-ray dose effect on the normalized electron trapping lifetime at 23.5 ºC and at 35.5 ºC

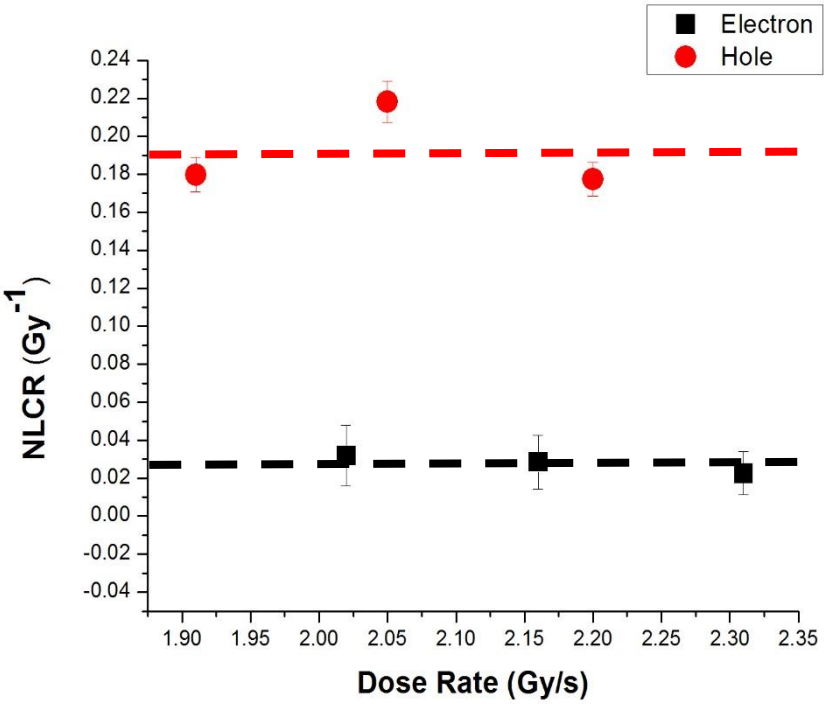

Figure 4.12 Normalized lifetime change rate (NLCR) dependence on dose rate

The results of the temperature effect on the lifetime dependence on the accumulated dose for holes and electrons are shown in Figure 4.10 and 4.11 respectively. The hole normalized lifetime change with X-ray dose was significantly affected by the change in temperature. The rate of decrease in the hole normalized lifetime is more rapid at 35.5^{o}C than at room temperature. The hole lifetime was reduced to about 20% of the initial lifetime by 5 Gy of the dose at 35.5 ^{o}C. At 23.5 ^{o}C, about 40 Gy X-ray dose reduced the hole lifetime to about 20% of the initial value. However, change in temperature does not have a significant effect on the rate of X-ray dose reduction in the electron trapping lifetime. Electron normalized lifetime was reduced to about 40% of its initial value before X-ray irradiation by up to 12 Gy accumulated X-ray dose. The normalized electron lifetime is observed to change with accumulated X-ray dose at 23.5 ^{o}C and 35.5^{o}C. The dependence of normalized lifetime change rate (NLCR) on the dose rate results is show in Figure 4.12.

The dependence of normalized lifetime (τ) and the reciprocal ($1/\tau$) on accumulated dose D for holes and electrons at 23.5 ^{o}C and 35.5 ^{o}C are shown in Figures 4.13 to 4.16. It has been established that normalized lifetime decreases with accumulated dose in Figures 4.10 and 4.11. The curves through the figures are guides to the eye.

Table 4.7 Hole and Electron normalized lifetime change rate at different temperature

Temperature ^{o}C	Normalized Lifetime Change Rate for Hole, A (Gy^{-1})	Normalized Lifetime Change Rate for Electron, A (Gy^{-1})
23.5	0.076 ± 0.014	0.132 ± 0.021
35.5	0.569 ± 0.006	0.173 ± 0.023

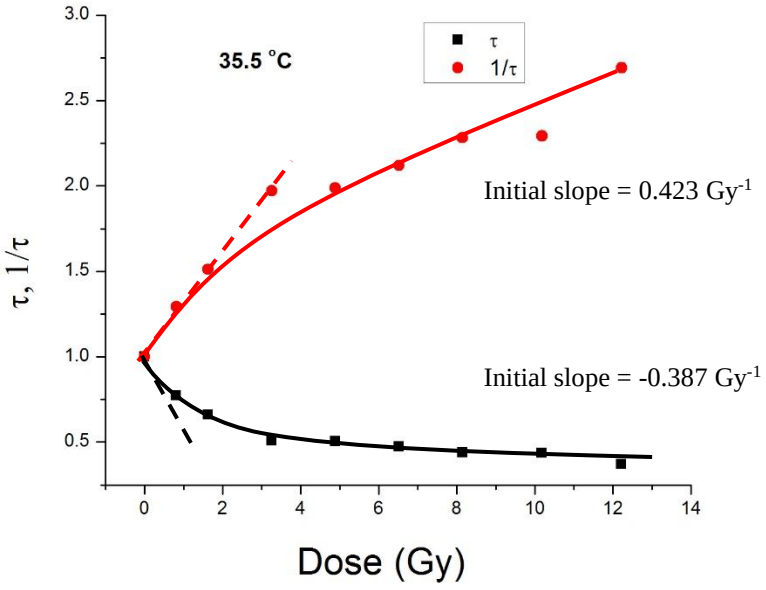

Figure 4.13 Electron Normalized lifetime (τ) and its reciprocal ($1/\tau$) dependence on dose D at 35.5 ^{o}C

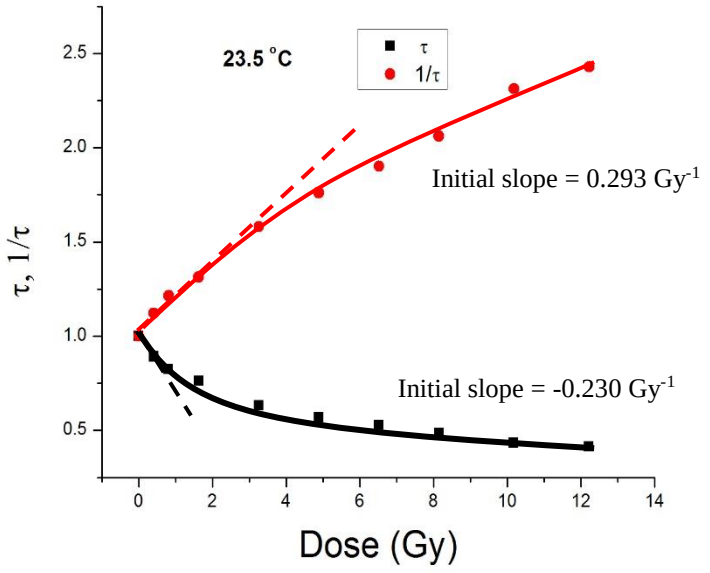

Figure 4.14 Electron Normalized lifetime (τ) and its reciprocal ($1/\tau$) dependence on dose D at 23.5 ^{o}C

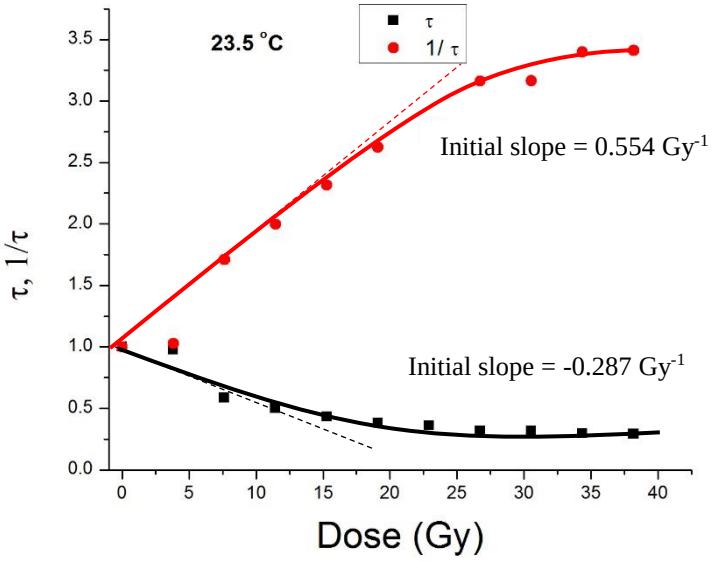

Figure 4.15 Hole Normalized lifetime (τ) and its reciprocal ($1/\tau$) dependence on dose D at 23.5 ^{o}C

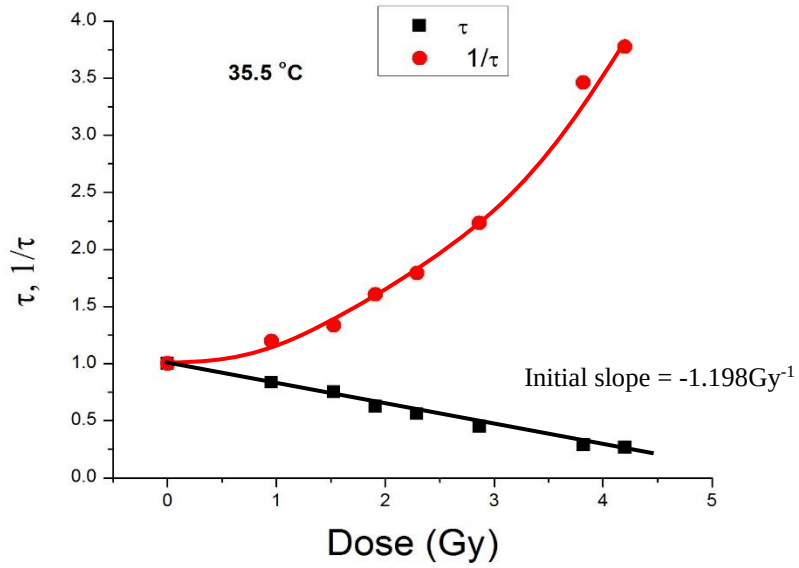

Figure 4.16 Hole Normalized lifetime (τ) and its reciprocal ($1/\tau$) dependence on dose D at 35.5 ^{o}C

A linear relationship was observed at the initial small doses and an initial slope to represent the fractional change in τ and $1/\tau$ per accumulated dose. These initial slopes show the sensitivity of charge carries lifetime to delivered dose.

4.4 Lifetime Recovery

Immediately after the accumulated dose experiments, the lifetime recovery process starts. The structural changes induced by the X-ray irradiation gradually recovers to the equilibrium through a structural relaxation process. The effect of temperature on the recovery process was examined at room temperature and 35.5 ^{o}C. The lifetime recovery experiment was also examined under LED lights of different wavelength and intensities to observe the effect of light on the recovery process.

The recovery process for both holes and electrons was observed to have a stretched exponential recovery that follows the following expression. [10]

$$\tau_{\text{irradiated}} = \tau_{\text{unirradiated}} - (\tau_{\text{unirradiated}} - \tau_{\text{initial}})\exp^{\left(-\frac{t}{\tau_{\text{sr}}}\right)^{\beta}} \qquad 4.9$$

A dataset of the carrier lifetime vs time recorded in the recovery process is well fitted by performing a non-linear least square fit. This can be simplified into

$$\tau_{\text{normalized}} = 1 - (1 - \tau_{0\text{i}})\exp^{\left(-\frac{t}{\tau_{\text{sr}}}\right)^{\beta}} \qquad 4.10$$

where τ_{0i} is the normalized initial carrier lifetime right after x-ray irradiation, τ_{sr} is the structural relaxation time and β is the stretched exponential parameter for data fitting. The structural relaxation time τ_{sr} is the average time for the irradiated sample to recover to it equilibrium state before X-ray irradiation. The reason for the use of "structural" in the name is because the recovery process involves structural changes that remove the x-ray induced defects. τ_{sr} is assumed to be X-ray dose independent but dependent on the sample composition and hence its structure; thus, this quantity would be different for each sample

At time t = 0, Equation 4.10 is reduced to

$$\tau_{\text{normalized}} = \tau_{0i} \qquad 4.11$$

Equation 4.11 gives the carrier trapping just after X-ray irradiation. When the time *t* goes to infinity, the exponential term tends to 1 while equation 4.10 is reduced to

$$\tau_{\text{normalized}} = 1 \qquad 4.12$$

Equation 4.12 presumes that, after a sufficiently long time, the carrier lifetime recovers to its initial state.

The results for the hole and electron lifetime recovery at 23.5 ^{o}C and at 35.5 ^{o}C are shown in Figure 4.17 and 4.18 respectively. The effect of temperature on the recovery process is more pronounced for holes than electrons. The hole lifetime recovers very rapidly at 35.5 ^{o}C compared to 23.5 ^{o}C as shown in Figure 4.17 and summarized in Table 4.8. At 23.5 ^{o}C, hole trapping lifetime takes more than 30 hours to recover to about 90% of its initial value while at 35.5 ^{o}C, its take less than 5 hours. Similar results were observed for electron lifetime. The recovery process took about 13 hours for electrons at room temperature while at 35.5 ^{o}C, it takes less than 2 hours to recover.

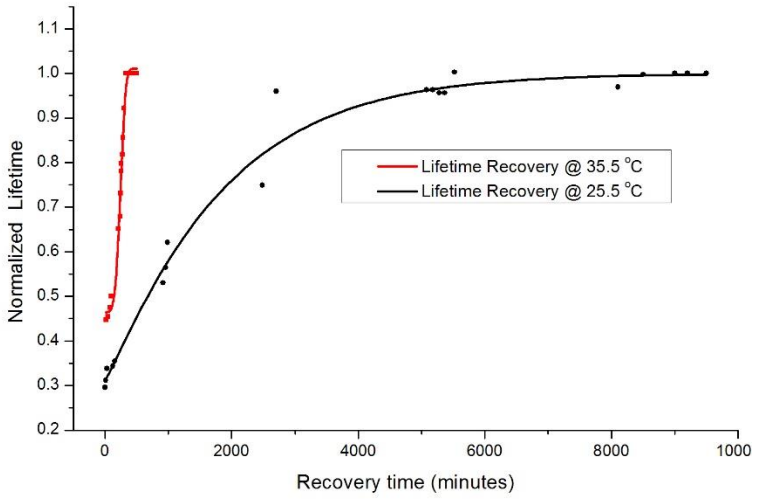

Figure 4.17 Normalized Hole lifetime recovery at different temperature

The higher temperature allows greater atomic diffusion and faster molecular configurational changes which could be as a result of an expansion in the volume. These processes aid the annealing of X-ray induced defects.

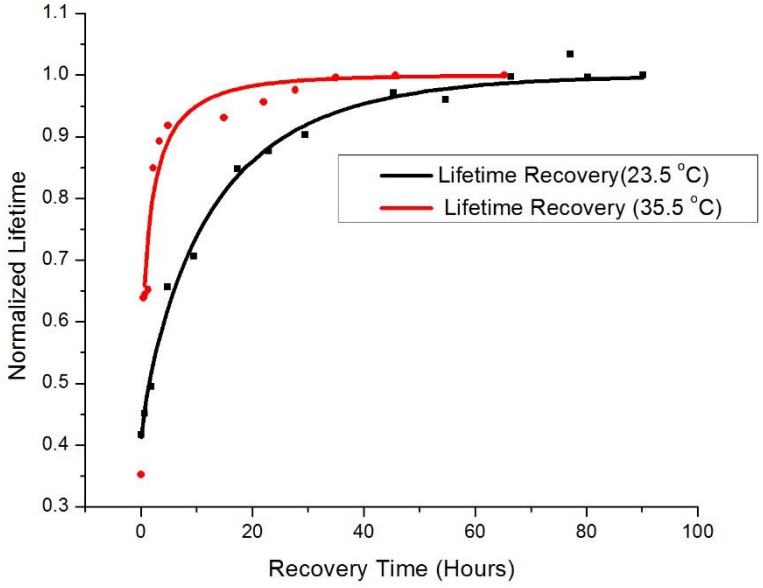

Figure 4.18 Normalized hole lifetime recovery at different temperature

Table 4.8 Structural Relaxation Time for Different Temperature

Temperature ^{o}C	Hole Relaxation Time τ_{sr} (Hours)	Electron Relaxation Time τ_{sr} (Hours)
23.5	30.5 ± 2.5	12.7 ± 2.6
35.5	4.43 ± 2.41	1.3 ± 0.8

4.5 Summary

The results of the TOF and IFTOF measurements conducted during this study, the X-ray dose deposited in the samples, the X-ray induced effects on the electronic properties of a-Se samples at room temperature and 35.5 ^{o}C, and the lifetime recovery measurements at 23.5 ^{o}C and 35.5 ^{o}C are presented in this chapter.

The X-ray dose rate used for the X-ray irradiation fall between 1.9 and 2.5 Gy/s. The maximum X-ray dose for the X-ray induces an effect on the hole is about 35 Gy which reduced the normalized hole-trapping time to about 20% of the initial lifetime before irradiation. Three different dose rates were applied to the sample and the normalized lifetime change rate has an average value 0.2 Gy^{-1} for all the different dose rate. In the case of the electron, the maximum dose is 60 Gy which induced a reduction of the trapping lifetime to about 40% of the initial value before X-ray irradiation. The normalized lifetime change rate for electron for the dose rates used has an average value of 0.028 Gy^{-1}. These results are consistent with the previous measurement by Yang [10] and Michael [4].

The effects of temperature on the X-ray induced carrier trapping lifetime changes were also studied at room temperature 23.5 ^{o}C and 35.5 ^{o}C for the accumulated dose measurements. At 35.5 ^{o}C, the hole-trapping lifetime decreases very rapidly at a normalized lifetime change rate of about 0.6 Gy^{-1}. At the lower temperature, the normalized lifetime change rate is about 0.1 Gy^{-1}. In the case of the electron, the value of the normalized lifetime change rate at 35.5^{o}C and 23.5^{o}C are very close and the electron-trapping lifetime decreases very slowly.

For the lifetime recovery measurements, the same temperatures were chosen. The hole-trapping lifetime recovers very fast with a relaxation time of 4.4 hours and the rate of recovery is slower, about 30.5 hours, at a lower temperature. The electron-trapping lifetime follows a similar pattern as the hole-trapping lifetime. The relaxation time at higher temperature is 1.3 hours and at a lower temperature in about 13 hours.

5. SUMMARY AND CONCLUSION

Stabilized amorphous selenium has been one of the most suitable photoconductive materials for use in flat panel direct conversion detectors. This is because it can be fabricated over a large area uniformly using conventional vacuum deposition method and the cost of fabrication is relatively cheap compared to other photoconductive materials. When x-ray photons are absorbed in the photoconductor, electron-hole pairs are generated. The applied field separates and drift the carriers which are collected and form the photocurrent signal. In this work, the effect of X-ray irradiation on charge transport parameters were examined. X-ray-induced effects on the carrier trapping lifetime of a-Se and the recovery process under certain conditions were examined. The recovery process was studied at different temperatures, 23.5 ^{o}C and 35.5 ^{o}C. The charge transport measurement techniques employed in this work were the time-of-flight (TOF) and Interrupted-field-time-of-flight (IFTOF) techniques to capture the transient photocurrent produced by the drift of charge carriers in a-Se samples. The time-of-flight method measures the carrier mobility and the Interrupted-field-time-of-flight measure the carrier trapping lifetime. These charge transport parameters are the key to understanding the performance of a-Se X-ray detectors

5.1 X-ray Induced Changes in the Lifetime

The effect of X-ray irradiation was observed by the accumulated dose measurement experiment. The samples were irradiated by X-rays produced by an X-ray tube system at peak voltage 70 kVp, with average X-ray energy of 37.37 keV, and was kept the same for all X-ray irradiations. The delivered dose was controlled by adjusting the filament current and the distance between the x-ray source and the sample.

The samples used in this work were pure a-Se and stabilized a-Se that is a-Se: 0.5% As doped with 10 ppm Cl and a-Se: 0.3% As doped with 2.5 ppm Cl). Sample thicknesses ranged between 50 μm to 200 μm. The accumulated dose measurements involved the X-ray irradiation of the sample and IFTOF measurements. IFTOF measurements allowed the carrier lifetimes to be monitored as a function of accumulated dose. X-ray dose deposited

in the samples were estimated by measuring the exposure by a dosimeter system. The dependence of the carrier lifetime on the accumulated dose was studied as a function of the dose rate, that is, whether the induced effects depend on the dose rate. Three different dose rates were chosen to irradiate the samples for hole and electron transport measurements. After an accumulated dose of about 35 Gy was deposited, the hole trapping lifetime was reduced to 20% of the initial value of the lifetime before the X-ray irradiation. The electron trapping lifetime was reduced to 40% of its initial value before the X-ray irradiation by an accumulated dose of 70 Gy. The rate of normalized lifetime change gives the X-ray dose effect on the carrier trapping lifetime was computed for each dose rate. The results show that the induced effect of the X-ray dose on the carrier trapping time is independent of the X-ray dose rate within experimental errors. This means that the x-ray induced effects depend on the total energy delivered and not on the rate of delivery over the dose rates examined.

The examination of the normalized rate of capture vs. the accumulated dose at room temperature follows the reported behavior in which $1/\tau = 1 + AD$, where A is a constant and D is the accumulated dose. The constant A, within experimental errors, is independent of the dose rate. This behavior was observed for both holes and electrons.

The effect of temperature on the X-ray induced carrier trapping time was also investigated in this study. The accumulated dose measurements were done at 23.5 ^{o}C and 35.5 ^{o}C. The hole trapping lifetime decrease more rapidly with X-ray dose at the higher temperature than at the lower temperature. The normalized lifetime change rate at the higher temperature is about 8 factors more than at the lower temperature for the hole lifetime. For the electron trapping lifetime, the normalized lifetime change rate at higher temperature is about a factor of 0.5 more than at lower the temperature. This could be because at higher temperature, atomic bonding is more pliable and not stable, which makes it possible for X-ray to generate localized defects in the band gap of a-Se. This reason could also be responsible for faster relaxation time at the higher temperature.

5.2 Carrier Trapping Lifetime Recovery Process

Once the X-ray irradiation stops, the lifetime starts to recover to its initial equilibrium value through a structural relaxation process. The lifetime recovery measurement tracks the progressive recovery of the X-ray induced changes in the carrier trapping lifetime. The carrier trapping lifetime was measured at a series of time intervals after the cessation of X-ray irradiation until the value of the carrier lifetime fully recovers (to within 90%) of the initial equilibrium value. The recovery process is a stretched exponential type of behavior as proposed previously. The data were fitted by a non-linear least square fit. The recovery process was observed at different temperatures, 23.5 ^{o}C and 35.5 ^{o}C. The relaxation time characterizes the relaxation process and gives the average time the carrier lifetime takes to recover to its initial value.

At higher the temperature, both hole and electron trapping lifetime recover more rapidly than at the lower temperature. The relaxation time drops from about 30.5 hours at 23.5 ^{o}C to 4.4 hours at 35.5 ^{o}C for the hole lifetime. The relaxation time for electron trapping lifetime drops from 12.7 hours at room temperature to 1.3 hours at 35.5 ^{o}C. The structure of a-Se at a higher temperature is floppier (than rigid) which makes it easier to generate defects by X-ray irradiation. The floppy structure also accounts for the faster recovery at the higher temperature. The decrease in the lifetime may also involve trapped carriers recombining with oppositely charged free carriers. At high temperatures, the release of trapped carriers would be much faster, so the recovery would also be faster.

5.3 Future Works

This study focuses on the X-ray induced effect on the carrier trapping lifetime of a-Se as a photoconductor for flat panel X-ray Image detectors and the recovery process of the carrier trapping lifetime after cessation of X-ray irradiation. However, the X-ray induced effect does not indicate if low energy X-rays or high energy X-rays will induce similar effects in a-Se. The present work used polychromatic x-ray energy source with a maximum 70 keV photon energy. This study could give a better understanding of how X-ray detector

performance could be influenced by X-rays of different energy range. In addition, the applied field on the a-Se during irradiation was fixed and the effect of changing the applied field was not examined. It would be very useful to examine whether the observed effects depend on the applied field.

The study of the recovery of X-ray irradiation damage in a-Se could be observed with a field and without a field to see whether the recovery depends on the field. If the x-ray effects include trapped carriers, at sufficiently high fields, there may be a field-enhanced carrier release of carriers, which can accelerate the recovery. Thus, the effect of the applied field in induced damage and recovery can be studied systematically.

REFERENCES

[1] A. R. Cowen, “Digital x-ray imaging,” Meas. Sci. Technol., vol. 2, pp. 691–707, 1991.

[2] N. F. Güler and E. D. Übeyli, “Theory and applications of telemedicine,” J. Med. Syst., vol. 26, no. 3, pp. 199–220, 2002.

[3] R. Tanha, “Electron And Hole Transport In Stabilized A-Se For X-Ray Imaging Chapter1,” 1997.

[4] M. Walornyj, “Electron Lifetime And Its Dependence On Temperature And Dose In A-Se Photoconductors By,” 2013.

[5] Safa Kasap, Joel B. Frey, George Belev, Olivier Tousignant, Habib Mani, Jonathan Greenspan, Luc Laperrirer, Oleksandr Bubon, Allan Reznik, Giovanni Decrescenzo, Karim S. Karim And John Rowlands. “Amorphous And Polycrystalline Photoconductors For Direct Conversion Flat Panel X-Ray Image Sensors,” Sensors, Vol. 11, No. 5, Pp. 5112–5157, 2011.

[6] S. O. Kasap, M. Zahangir Kabir, and J. A. Rowlands, “Recent advances in X-ray photoconductors for direct conversion X-ray image detectors,” Curr. Appl. Phys., vol. 6, no. 3, pp. 288–292, 2006.

[7] C. S. Allen, “Relaxation in the Electrical Properties of Amorphous Selenium Based Photoconductors,” March, 2009.

[8] B. J. Fogal, “Electronic Transport Properties of Stabilized Amorphous Selenium X-ray Photoconductors,” March, 2005.

[9] J. M. Boone, “Chapter 1 X-Ray Production , Interaction , And Detection In Diagnostic Imaging,” Vol. 1, No. I, 2000.

[10] J. Yang, “X-ray Induced Changes in Electronic Properties of Stabilized Amorphous

Selenium Based Photoconductors," April, 2016.

[11] D. Mortensen, "Thickness dependence of electron transport in amorphous selenium for use in direct conversion flat panel X- ray detectors," July, 2012.

[12] P. Kasap, S.O., Capper, "Photoconductors for X-ray Image Detectors," Springer Handb. Electron. Photonic Mater., vol. 2, 2006.

[13] S. O. Kasap, Optoelectronics and Photonics, Principle and practice, Second Edition 2012.

[14] W. Que and J. A. Rowlands, "X-ray photogeneration in amorphous selenium: Geminate versus columnar recombination," Phys. Rev. B, vol. 51, no. 16, pp. 10500–10507, 1995.

[15] S. O. Kasap and G. Belev, "Progress in the science and technology of direct conversion X-ray image detectors: The development of a double layer a-Se based detector," J. Optoelectron. Adv. Mater., vol. 9, no. 1, pp. 1–10, 2007.

[16] S. O. Kasap and J. A. Rowlands, "X-ray photoconductors and stabilized a-Se for direct conversion digital flat-panel X-ray image-detectors," J. Mater. Sci. Mater. Electron., vol. 11, no. 3, pp. 179–198, 2000.

[17] M. Z. Kabir, S. O. Kasap, and J. A. Rowlands, "Direct conversion X-ray sensors: sensitivity, DQE and MTF," IEE Proc. - Circuits Devices Syst. ·, vol. 150, no. 3, pp. 258–266, 2003.

[18] G. Belev and S. O. Kasap, "Amorphous selenium as an X-ray photoconductor," J. Non. Cryst. Solids, vol. 345–346, pp. 484–488, 2004.

[19] E. Ientilucci, "Fundamentals of Xerography," Page. 1–9, 1994.

[20] A. M. Melvin P.Shaw, The Physics and Application of Amorphous Semiconductors. San Diego: Academic Press Inc, 1988.

[21] N.F. Mott, “Electrons in Disordered Structures,” Adv. Phys., vol. 16, pp. 49–57, 1967.

[22] P.W. Anderson, “Absence of Diffusion in Certain Random Lattices.” Page. 1492–1505, 1957.

[23] Brodsky M. H., “Amorphous semiconductors,” Springer-Verlag, 1979.

[24] M. H. Cohen, H. Fritzsche, and S. R. Ovshinsky, “Simple band model for amorphous semiconducting alloys,” Phys. Rev. Lett., vol. 22, no. 20, Page. 1065–1068, 1969.

[25] Kasap S.O., "Handbook of Imaging Materials", 2nd Edition, edited by A. Diamoond and D. Weiss, Maecel Dekker, New York, Chapter 9, 2002.

[26] F. L. G. Gerald Lucovsky, “Intermediate Range Order in Amorphous Solid,” vol. 36, Page. 1209–1214, 1980.

[27] M. Abkowitz, “On the Question of Rlevance,” J. Chem. Phys., vol. 46, pp. 4537–4538, 1967.

[28] S. C. Agarwal, “Nature of localized states,” Phys. Rev. B, vol. 7, no. 2, 1973.

[29] M. Abkowitz, “Density of states in a-Se from combined analysis of xerographic potential and transient transport data,” Philosophical Magazine Letter, 58, pp. 53–77, 1988.

[30] W. E. Spear, “Transit Time Measurements of Charge Carriers in Amorphous Selenium Films,” Proc. Phys. Soc. B, vol. 70, pp. 669–675, 1957.

[31] Kasap S., Koughia C., Berashevich J., Johanson R., Reznik A., "Charge transport in pure ans stabilized amorphous selenium: re-examination of the density of statedistribution in the mobility gap and the role of defects', J Mater Electron (2015) 26: Page 4644 - 4658

[32] M. Abkowitz, “Relaxation induced changes in electrical behavior of glassy chalcogenides semiconductors,” Polym. Eng. Sci., vol. 24, pp. 1149–1154, 1984.

[33] J. M. Marshall and A. E. Owen, “The hole drift mobility of vitreous selenium,” Phys. Status Solidi, vol. 12, no. 1, pp. 181–191, 1972.

[34] M. Kastner, D. Adler and H. Fritzsche, " Valence-Alternation Model for Localized Gap States in Lone-pair Semiconductors," Physical Review Letters, Vol. 37, Number 22, Page 1504 - 1507, Nov., 1976.

[35] M. Abkowitz, “Evidence for the defect origin of states which control photoelectronic behavior of amorphous chalcogenides,” J. Non. Cryst. Solids, vol. 66, no. 1–2, pp. 315–320, 1984.

[36] G. S. Belev, B. Fogal, K. V. Koughia, R. E. Johanson, and S. O. Kasap, “Dependence of charge-carrier ranges in stabilized a-Se on preparation conditions and alloying,” J. Mater. Sci. Mater. Electron., vol. 14, no. 10–12, pp. 841–842, 2003.

[37] W. C. Tan, G. Belev, K. Koughia, R. Johanson, S. K. O’Leary, and S. Kasap, “Optical properties vacuum deposited and chlorine doped a-Se thin films: Aging effects,” J. Mater. Sci. Mater. Electron., vol. 18, no. SUPPL. 1, pp. 429–433, 2007.

[38] H. Adachi and K. C. Kao, “Dispersive optical constants of amorphous Se1−xTex films,” J. Appl. Phys., vol. 51, no. 12, p. 6326, 1980.

[39] D. M. Pai and R. C. Enck, “Onsager mechanism of photogeneration in amorphous selenium,” Phys. Rev. B, vol. 11, no. 12, pp. 5163–5174, 1975.

[40] P. M. J. White S.C., “Oral Radiology: Principles and Interpretation,” Elseiver - Heal. Sci. Devision, pp. 20–22, 1999.

[41] Siemens, “X-ray Spectrum.” [Online]. Available: https://www.oem-xray-components.siemens.com/x-ray-spectra-simulation.

[42] S.O.Kasap, “Definitions in Radiation Physics.” 2003.

[43] W. E. Spear, “Drift mobility techniques for the study of electrical transport properties in insulating solids,” J. Non. Cryst. Solids, vol. 1, no. 3, pp. 197–214, 1969.

[44] S.O.Kasap, Optoelectronics and Photonics: Principles and Practices, Second. Pearson Education, Inc., 2013.

[45] K. R. Zanio, W. M. Akutagawa, and R. Kikuchi, “Transient currents in semi-insulating CdTe characteristic of deep traps,” J. Appl. Phys., vol. 39, no. 6, pp. 2818–2828, 1968.

[46] W. A. K. Zanio, “The Possibilities Of Using CdTe As A Gamma Spectrometer,” Ieee Trans. Nucl. Sci. 15, Pp. 266–274, 1968.

[47] Martini M., Mayer J.W., and Zanio K.R., “Drift velocity and trapping in semiconductors transient charge technique,” Appl. State Sci. Adv. Mater. Device Res., 1972.

[48] R. M. Blakney and H. P. Grunwald, “Small-signal current transients in insulators with traps,” Phys. Rev., vol. 159, no. 3, pp. 658–664, 1967.

[49] C. Allen, G. Belev, R. Johanson, and S. Kasap, “Relaxation of the electrical properties of vacuum-deposited a-Se1−xAsx photoconductive films: Charge-carrier lifetimes and drift mobilities,” J. Vac. Sci. Technol. A Vacuum, Surfaces, Film., vol. 28, no. 5, pp. 1145–1156, 2010.

[50] G. Corp, “Gendex Corp, GX-1000 intra oral x-ray system installatio/maintenance manual,” Millwaukee, WI USA.

[51] R. G. Kepler, “Charge carrier production and mobility in anthracene crystals,” Phys. Rev., vol. 119, no. 4, pp. 1226–1229, 1960.

[52] O. H. LeBlanc, “Hole and Electron Drift Mobilities in Anthracene,” J. Chem. Phys.,

vol. 33, no. 2, pp. 626–626, 1960.

[53] F. C. Brown, “Temperature dependence of elctron mobility in AgCl,” Phys. Rev., vol. 97, no. 2, pp. 355–363, 1955.

[54] S. O. Kasap and C. Juhasz, “Transient photoconductivity probing of negative bulk space charge evolution in halogenated amorphous selenium films,” Solid State Commun., vol. 63, no. 6, pp. 553–556, 1987.

[55] H. P. B. R. . Grunwald, “Trapping Processes in Amorphous Selenium*,” Phys. Rev., vol. 159, Numbe, no. 2, 1967.

[56] T. M. Hiroyoshi Naito, Masafumi Nakaishi, Hiroshi Nakayama, Masahiro Okuda, Tanehiro Nakau, Akio Suzuki, “Isothermal Photocurrent Transient Spectroscopy of Gap States in Amorphous Chalcogenide Semiconductors,” Jpn. J. Appl. Phys., vol. 22, no. 12, pp. 1818–1821, 1983.

[57] M. D. Tabak and P. J. Warter, “Field-controlled photogeneration and free-carrier transport in amorphous selenium films,” Phys. Rev., vol. 173, no. 3, pp. 899–907, 1968.

[58] T. I. Oda O., Onozuka A., “Effect Of Oxygen On Electrophotographic Properties Of Selenium,” J. Non. Cryst. Solids, Vol. 83, Pp. 49–62, 1986.

[59] R. M. J. Abkowitz, M. A., “Electronic transport in Silicon backbone polymers,” Philosophical Magazine Letter B, 61, pp. 25–27, 1990.

[60] S. O. Kasap, R. P. S. Thakur, and D. Dodds, “Method and apparatus for interrupted transit time transient photoconductivity measurements,” J. Phys. E., vol. 21, no. 12, pp. 1195–1202, 1988.

[61] B. Polischuk and S. O. Kasap, “A high-voltage interrupted-field time-of-flight transient photoconductivity apparatus,” Meas. Sci. Technol., vol. 2, no. 1, pp. 75–80,

1991.

[62] H. K. Kim, I. A. Cunningham, Z. Yin, and G. Cho, “On the Development of Digital Radiography Detectors : A Review,” Precis. Eng., vol. 9, no. 4, pp. 86–100, 2008.

[63] S. O. Kasap, John Rowland, B. Fogal, M Zahangir Kabir, G Belev, N Sidhu, Brad Polischuk, Robert E Johanson. “Progress In The Science And Technology Of Direct Conversion a-Se X-Ray Sensors,” J. Non. Cryst. Solids, Vol. 299–302, No. Part 2, Pp. 988–992, 2002.

[64] J. Berashevich, A. Mishchenko, and A. Reznik, "Two-Step Photoexcitation mechanism in Amorphous Se", Physical Review Applied 1.034008.

[65] W. C. Tan, “Optical Properties of Amorphous Selenium Films,” no. July, 2006.

[66] J. H. H. S. M. Seltzer, “Tables of X-ray Mass Attenuation Coefficients and Mass Energy-Absorption Coefficient from 1 keV to 20 MeV for Elements Z = 1 to 92 and 48 Additional Substances of Dosimetric interest,” NIST StandardReference Database 126, 1996. [Online]. Available: https://www.nist.gov/pml/x-ray-mass-attenuation-coefficients.